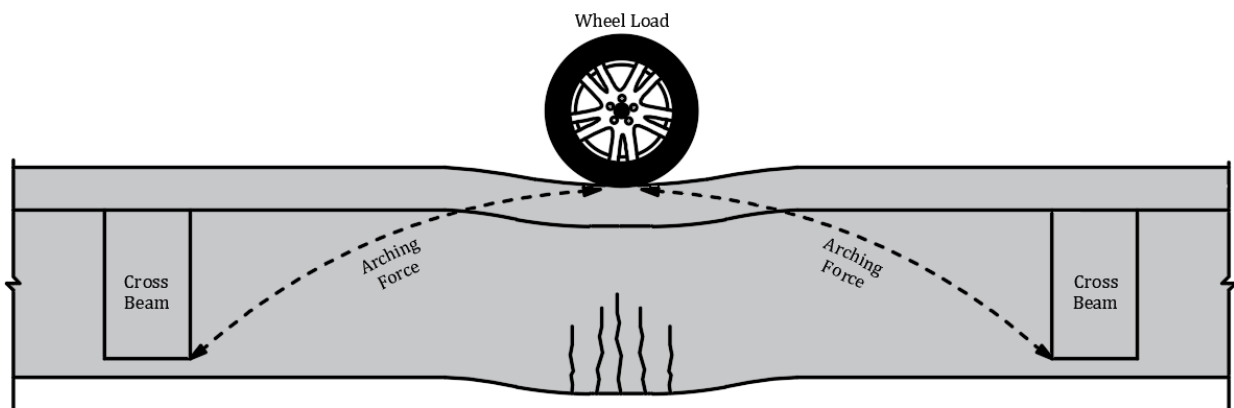
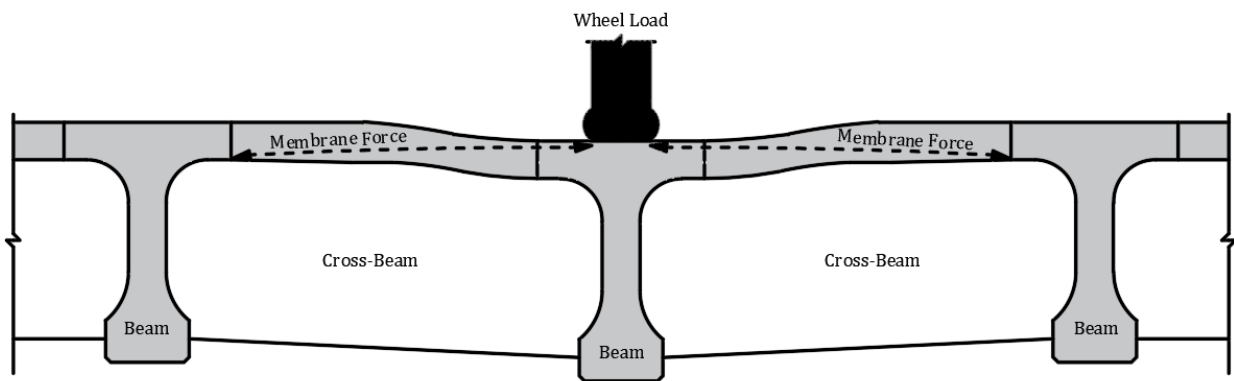


Analytical and Numerical Study of Arch Action in T-beam Bridges

Shozab Mustafa



Analytical and Numerical Study of Arch Action in T-beam Bridges

by

Shozab Mustafa

to obtain the degree of Master of Science
at the Delft University of Technology,
to be defended publicly on Thursday August 15, 2019 at 11:00 AM

Student number: 4708334
Project duration: December 1, 2018 - August 15, 2019
Thesis committee: Dr. ir. Max A.N. Hendriks, Chair of the Committee
ir. Sebastiaan Ensink, Daily Supervisor
Dr. ir. Cor van der Veen, Supervisor
ir. Lambert J.M. Houben, Supervisor

An electronic version of this thesis is available at <http://repository.tudelft.nl/>.

Preface

This research study is the culmination of my Master's degree experience at Delft University of Technology which has been an unforgettable journey. To say that this experience has been academically rewarding would be half the statement - from helping me learn to cope with self-doubt and feelings of over-whelm to triumphing the challenges and pushing my potential - it has also had a profound effect on my personality.

I would like to express my immense gratitude towards the chair of my thesis committee, Max Hendriks, for introducing me to the application of non-linear finite elements analysis and inspiring my interest in the field. I have learned a lot from his critical remarks and invaluable feedback during our discussion meetings for my graduation project and internship experience.

I would like extend my gratitude to Cor van der Veen for providing me with the opportunity to work on such an interesting and innovative project. His intellectual inputs and appreciative comments have inspired me to push my limits during the course of the research. I would also like to thank my daily supervisor, Sebastiaan Ensink, for always being available for consultation and providing constructive feedback every step of the way. It has been an enriching learning experience to work with both of them.

My sincere gratitude to TU Delft for deeming me worthy of Justus & Louise van Effen Excellence Scholarship. This honor has helped me sail through my masters without any financial concerns and has continuously been a source of motivation to work harder towards my goals.

I would also like to thank my family for their unconditional love and support throughout this period. Last, but not the least, I would like to thank my friends, peers and all the connections I made during this period that have made this experience worth the while!

Shozab Mustafa
Delft, August 2019

Abstract

The main objective of this research is to understand the development of arch action in a single T-beam acting as part of the bridge system, ignoring the distribution of the load in transverse direction. As the beam is loaded, several mechanisms work simultaneously in the bridge system, resulting in enhanced ultimate load bearing capacity of the bridges, like compressive membrane action (CMA) in deck slabs and arch action in concrete beams.

In the first phase of the project, an approximate analytical model for quantification of arch action in underwater concrete slabs loaded with uniformly distributed loads (suggested in CUR-077) is verified using non-linear finite element analysis for varying span-to-depth ratios, stiffness of lateral restraint and initial prestressing in the system. The adopted analytical model seems to be able to conservatively predict the arching capacity (within 12%), horizontal stretch (within 10%) and membrane forces (within 10%) in concrete members when compared to the numerical models, provided that the slenderness is less than 15 and the stiffness of end-restraint is at least equal to the stiffness of restrained member. However, the vertical deformations are underestimated by almost 50% for all the models because the adopted analytical model only takes into account the rigid body rotation, ignoring the effect of bending deformations and shortening of the beam under membrane force. Prestressing seems to have a slightly positive effect on arching behavior and the analytical model is unable to capture this effect. The verified analytical model is then extended to beams loaded with concentrated loads and within the central half of the span, the adapted model is able to conservatively predict the arching capacity with an accuracy of at least 15%. The analytical model is then further extended to beams with T-shaped cross-sections for uniform and concentrated loads. These models are able to predict the arching capacity in T-beams with an accuracy of 7.5% when the numerical failure is due to crushing of concrete. In T-beams with thin webs, the strut failure is observed and the adapted models are not able to predict the arching capacities.

In the second phase, the beam from the Vechtbrug is modeled using 2D, 2.5D and 3D approaches in DIANA and the models are validated using the experimental work done by Ensink as part of his PhD studies. All the models show comparable load-deformation behavior and peak loads (within 7%) but only the 3D model is able to simulate the crack pattern observed during experiments. The validated numerical model of the Vechtbrug beam is then adapted as though it is connected to the bridge through cross-beams by applying full restraint at the edge faces of the cross-beams in longitudinal direction. Using the adapted beam model, it is found that modeling only the loaded sub-span as non-linear causes only 7% loss in accuracy and takes 67% less computational time when compared to the full non-linear adapted beam model. The results of the adapted Vechtbrug beam model are also compared with a disjointed bridge model developed by Ensink in which the distribution of the load is prevented in transverse direction by disconnecting the slab of the loaded sub-span with neighboring beams. Applying full restraints at the edge faces of cross-beams is found to overestimate the influence of arch action in the loaded sub-span when compared to the disjointed bridge model. The adapted analytical model (from the

first phase of the project) for T-beams with point loads is applied on the loaded sub-span but is found to be unable to conservatively predict the arching capacity owing to the thin web causing strut failure.

This report, therefore, also consist of two parts. The first part discusses the results of sensitivity analysis and extension of the analytical model (chapter 2, chapter 3 and chapter 4) and the second part discusses the modeling of the Vechtbrug beam and the methods used to model the behavior of a beam as though it is connected to the bridge through cross-beams (chapter 5, chapter 6 and chapter 7).

Contents

List of Figures	xi
List of Tables	xv
1 Introduction	1
1.1 Background and Motivation	2
1.2 Scope and Objectives of Research	6
1.3 Research Hypothesis	7
1.3.1 Research Questions and Methodology	7
Part-I Sensitivity Analysis and Modification of CUR Method	8
2 Analytical Model	11
2.1 Background and Description of the Analytical Model	12
2.2 Simplified Analytical Model - UDL	14
2.3 Modified Analytical Model - Point Load	16
2.4 Modified Analytical Model - T-Beam with UDL	17
2.5 Modified Analytical Model - T-Beam with Point Load.	19
3 Numerical Model	21
3.1 Description of the Numerical Model.	22
3.2 Geometry of the Model.	22
3.2.1 PCC Models	22
3.2.2 Compression Model	23
3.2.3 Prestressed Model.	23
3.2.4 Point Load Model	24
3.2.5 T-Beam Model (UDL).	24
3.2.6 T-Beam Model (Point Load)	24
3.3 Material Properties	25
3.3.1 Concrete	25
3.3.2 Prestressing Steel	27
3.3.3 Boundary Interface at Edges	27
3.3.4 Plates and Plate Interface	28
3.4 Composed Lines.	29
3.5 Loads	29
3.6 Supports and End Restraint	29
3.7 Mesh.	29
3.8 Analysis Procedure	30
4 Sensitivity Analysis (CUR and Modified CUR)	31
4.1 Sensitivity Analysis - General	32
4.1.1 PCC Ideal Model.	32
4.1.2 PCC Parabolic Model.	34

4.1.3	Compression Model	35
4.1.4	Prestressed Model.	36
4.1.5	Comparison of the Numerical Models	38
4.2	Slenderness Sensitivity Analysis	39
4.3	End Stiffness Sensitivity Analysis	42
4.4	Beam Width Sensitivity Analysis	44
4.5	Prestressing Sensitivity Analysis	46
4.6	Load Location Sensitivity Analysis	48
4.7	Web-width Sensitivity Analysis (T-beams with UDL)	53
4.8	Web-width Sensitivity Analysis (T-beams with Point Load)	56
Conclusions (Part-I)		61
Part-II Assessment of Vechtbrug Beam		64
5	Vechtbrug - Layout and Details	67
5.1	Location and Layout of Vechtbrug	68
5.2	Description of Vechtbrug Beam.	69
5.3	Results of Material Testing.	71
5.4	Results of Individual Beam Tests	72
6	Vechtbrug - Numerical Model	75
6.1	Description of Vechtbrug Beam.	76
6.2	Geometry of the Beam	76
6.2.1	2D Model	76
6.2.2	3D Model	77
6.2.3	2D Shell Model	78
6.3	Material Properties	79
6.3.1	Concrete	79
6.3.2	Reinforcing and Prestressing Steel	80
6.3.3	Load and Support Plate Interface	81
6.4	Loads	81
6.4.1	Prestressing Loads	81
6.4.2	Applied Load.	82
6.5	Behavior of the End-Beam.	82
6.6	Support Conditions	85
6.7	Mesh.	85
6.7.1	2D Model	86
6.7.2	3D Model	86
6.7.3	2D Shell Model	88
6.8	Analysis Set-up.	88
6.9	Results.	89
6.9.1	Load at 2250mm	89
6.9.2	Load at 4000mm	94
6.10	Refinement using Post-tension Load	99
7	Comparison of Disjointed Bridge and Equivalent Beam Model	101
7.1	Equivalent Beam Model	102
7.2	Disjointed Bridge Model	106

Conclusions (Part-II)	111
Recommendations	113
Appendices	117
A Appendix A	117
B Appendix B	121
C Appendix C	125
Bibliography	135

List of Figures

1.1	Number of bridges constructed in NL over time [6]	2
1.2	Arch action in concrete members	3
1.3	Influence of arch action on the load deflection response of concrete members [17]	3
1.4	Compressive membrane action in bridge deck slabs	4
1.5	Arch action in T-beams	4
1.6	Trial beam models	5
1.7	Comparison of fully restrained and simply supported trial beam	5
1.8	Cross-section of Vechtbrug beam	6
2.1	CUR method - undeformed state	12
2.2	CUR method - deformed state	13
2.3	CUR formulation (spring and load capacity) [2]	13
2.4	Typical results of CUR method	15
2.5	Modified CUR method - point load	16
2.6	T-beam cross-section	17
2.7	Modified CUR method - T-beams with UDL	18
2.8	Compressive zone height for T-beams loaded with UDL	19
2.9	Modified CUR method - T-beams with point load	19
2.10	Compressive zone height for T-beam loaded with point load	20
3.1	PCC model for numerical analysis	23
3.2	Compression model for numerical analysis	23
3.3	Prestressed model for numerical analysis	23
3.4	Point load model for numerical analysis	24
3.5	T-beam model with UDL	24
3.6	T-beam model with point load	25
3.7	Tensile behavior of concrete	26
3.8	Compressive behavior of concrete	26
3.9	Prestressing steel material model	27
3.10	Typical mesh of the models	30
3.11	Typical convergence behavior of the models	30
4.1	Location of vertical and horizontal deformation measurement	32
4.2	General behavior of PCC ideal model	33
4.3	General behavior of PCC parabolic model	35
4.4	General behavior of compression model	36
4.5	General behavior of prestressed model	37
4.6	Load deformation comparison of the variants	38
4.7	Comparison of analytical and numerical load-deformation behavior	39

4.8	Slenderness sensitivity analysis	40
4.9	Peak load against horizontal deformation for ideal PCC model (Slenderness Sensitivity)	41
4.10	End stiffness sensitivity analysis	42
4.11	Peak load against horizontal deformation for ideal PCC model (Stiffness Sensitivity)	44
4.12	Beam width sensitivity analysis	45
4.13	Peak load against horizontal deformation for ideal PCC model (Beam width sensitivity)	46
4.14	Prestressing sensitivity analysis	47
4.15	Effect of prestressing on CUR formulation	48
4.16	Peak load against horizontal deformation for ideal PCC model (Prestressing Sensitivity)	48
4.17	S2 and compressive zone height comparison for varying load location	49
4.18	S2 comparison for varying load location	50
4.19	E_{cw1} comparison for varying load location	51
4.20	Load location sensitivity analysis	52
4.21	Peak load against horizontal deformation for ideal PCC model (Load Location Sensitivity)	52
4.22	T-beam cross-section for sensitivity analysis	53
4.23	Web width sensitivity analysis for T-beam with UDL	54
4.24	S2 comparison for varying web width	55
4.25	E_{cw1} comparison for varying web width	55
4.26	Peak load against horizontal deformation for parabolic PCC model (Web width sensitivity)	56
4.27	Web width sensitivity analysis for T-beam with point load at 4000mm	57
4.28	S2 comparison for varying web width with load at 4000mm	58
4.29	E_{cw1} comparison for varying web width with load at 4000mm	58
4.30	Web width sensitivity analysis for T-beam with point load at 2250mm	59
4.31	S2 comparison for varying web width with load at 2250mm	60
4.32	E_{cw1} comparison for varying web width with load at 2250mm	60
5.1	Location of the Vechtbrug [13]	68
5.2	Layout of the Vechtbrug with marked test locations [7]	69
5.3	Cross-section and tendon anchorage	70
5.4	Beam geometry and tendon anchorage	70
5.5	Cross beam detail	71
5.6	Saw-cuts used for individual beam tests	71
5.7	Experimental set-up and location of LVDTs	72
5.8	Results of individual beam tests	73
5.9	Overview of the test set-up used at site	74
6.1	Longitudinal view of the beam	76
6.2	Cross-sectional function definition in 2D	77
6.3	Longitudinal view of 2D model	77
6.4	Isometric view of the 3D model	78
6.5	Isometric view of the reinforcement in 3D model	78

6.6	Isometric view of the 2D shell model	79
6.7	Tying used in shell model	79
6.8	Behavior of concrete for Vechtbrug beam model	80
6.9	Behavior of reinforcing and prestressing steel	81
6.10	Application of load in DIANA	82
6.11	Tying and supports for end-beam model	83
6.12	Tying and supports for end-beam	83
6.13	Torsional cracks in the end-beam	84
6.14	Force-deformation behavior of end-beam	85
6.15	Supports of beam in 2D	85
6.16	Elements used in 2D model	86
6.17	3D cross-sectional mesh	86
6.18	3D isometric mesh	87
6.19	Elements used in 3D model	87
6.20	Elements used in 2D shell model	88
6.21	Load-deformation comparison of numerical models and experiments for load at 2250mm	89
6.22	Behavior of the 2D model with load at 2250mm	91
6.23	Behavior of the 3D model with load at 2250mm	92
6.24	Behavior of the 2D shell model with load at 2250mm	93
6.25	Cracking behavior of tested beams with load at 2250mm [13]	94
6.26	Load-deformation comparison of 3D model and experiments for load at 4000mm	95
6.27	Behavior of the 2D model with load at 4000mm	96
6.28	Behavior of the 3D model with load at 4000mm	97
6.29	Behavior of the 2D shell model with load at 4000mm	98
6.30	Cracks after test 7 [13]	99
6.31	Comparison for stress distribution in a tendon	100
6.32	Comparison for axial prestressing force in the system	100
7.1	Geometry of the equivalent beam model	102
7.2	Reinforcement of the equivalent beam model	103
7.3	Intermediate cross-beam boundary conditions	103
7.4	Shear force and moment distribution in linear elastic bridge system [7]	104
7.5	Description of EQ-NL and EQ-CB model	104
7.6	Comparison of EQ-NL and EQ-CB model	105
7.7	Comparison of crack pattern for EQ-NL and EQ-CB model	106
7.8	Disjointed bridge model with disconnected slab (Light gray part is non-linear)	107
7.9	Disjointed bridge model mesh (Light gray part is non-linear)	108
7.10	Comparison of disjointed bridge model and equivalent beam model	108
7.11	Comparison of shear force distribution in equivalent beam and disjointed bridge model	109
7.12	Cracks in the loaded sub-span of disjointed bridge model	110
7.13	Vechtbrug beam and transformed T-section for CUR method application	110
R.1	Effect of arching on shear capacity of prestressed concrete beams	115
A.1	Convergence behavior of 2D model with load at 2250mm from the support	118
A.2	Convergence behavior of 3D model with load at 2250mm from the support	118

A.3	Convergence behavior of 2D shell model with load at 2250mm from the support	118
A.4	Convergence behavior of 2D model with load at 4000mm from the support	119
A.5	Convergence behavior of 3D model with load at 4000mm from the support	119
A.6	Convergence behavior of 2D shell model with load at 4000mm from the support	119
B.1	Convergence behavior of EQ-CB Model	122
B.2	Convergence behavior of EQ-NL Model	122
B.3	Convergence behavior of EQ-CB model used for comparison with disjointed bridge model	122
B.4	Convergence behavior of the disjointed bridge model	123

List of Tables

3.1	Properties of concrete in DIANA	27
3.2	Properties of interface between beam and plates	29
4.1	PCC ideal model	32
4.2	PCC parabolic model	34
4.3	Compression model	35
4.4	Prestressed model	37
4.5	Summary - Slenderness sensitivity analysis	39
4.6	Summary - End stiffness sensitivity analysis	42
4.7	Summary - Beam width sensitivity analysis	45
4.8	Summary - Prestressing sensitivity analysis	46
4.9	Summary - Load location sensitivity analysis	49
4.10	Summary - Web width sensitivity analysis	53
4.11	Summary - Web width effect in numerical models	54
4.12	Summary - Web width and load location sensitivity analysis	57
5.1	Test description - summary	69
5.2	Material investigation results	72
6.1	Properties of concrete in DIANA for Vechtbrug models	80
6.2	Properties used for post-tensioning load	82
6.3	Peak load and computation time comparison for load at 2250mm	90
6.4	Peak load comparison for load at 4000mm	95
7.1	Computation time of EQ-NL and EQ-CB model	106
7.2	Parameters used to calculate analytical arching capacity of the loaded sub-span 110	

1

Introduction

This chapter outlines the main objectives of the research and explains the step by step procedure adapted to try and answer the set out research questions.

1.1. Background and Motivation

In recent years, the assessment of existing structures has become one of the major concerns of the engineers all around the world, especially in Europe, as most of the structures constructed after the second world war approach the end of their service life. This has lead engineers to use advanced methods like non-linear finite element analysis (NLFEA) to assess the current condition and estimate the remaining life time of these structures.

Most of the bridges in Netherlands were also constructed during 60s and 70s as can be seen in figure 1.1 and approximately 150 [7] such prestressed T-beam bridges with cast-in-between decks are still in service. As these bridges were constructed using the older Dutch code N 1009: 1950 [14] which had a less conservative shear capacity approach compared to the current Eurocode (EN 1992-1-1:2005) [1], most of the prestressed beams do not fulfill the safety requirements upon assessment and hence the safety of such bridges is questioned. This effect is even worsened by the increased traffic loads on bridges which they were not designed for. However, upon inspection there seems to be no sign of distress, begging the question about the source of this additional capacity in concrete bridges.

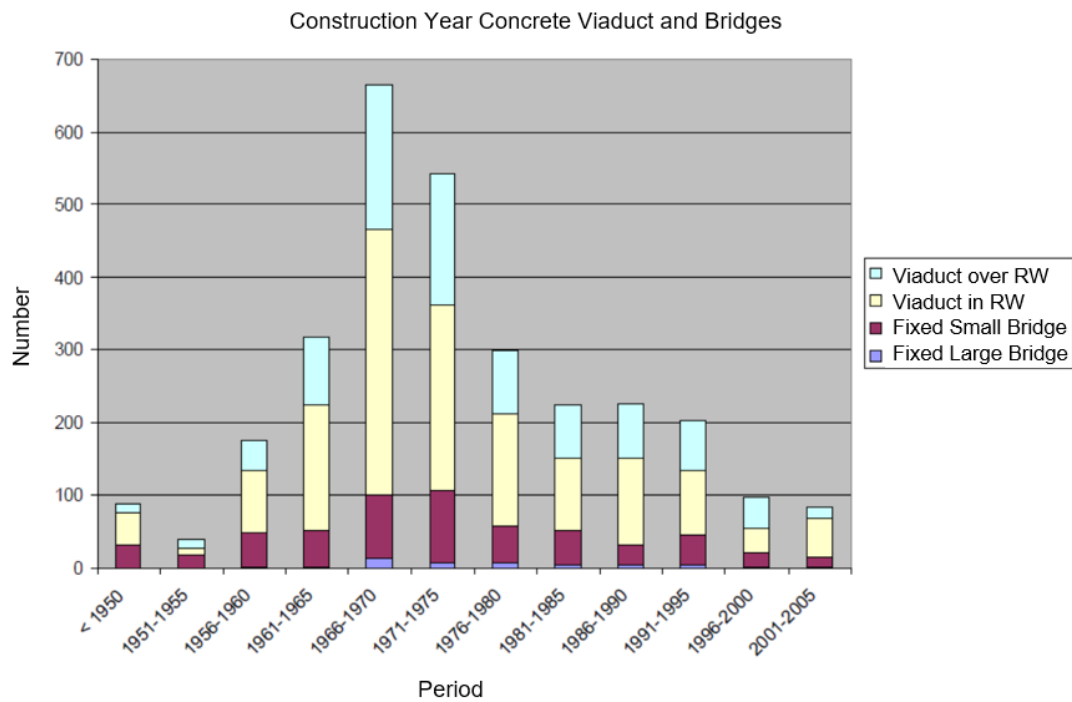


Figure 1.1: Number of bridges constructed in NL over time [6]

Possible explanation to this increased capacity can be either the increased concrete strength over time due to continuous hydration process or certain mechanisms working (simultaneously) in the bridge system resulting in increased resistance. Many researchers have tried to explain this discrepancy through the arch action in laterally restrained concrete slabs, more commonly referred to as compressive membrane action (CMA) but this mechanism alone does not explain the differences in experimental and analytical results. Therefore, this project studies the possibility for the development of arch action in the longitudinal direction i.e. in the prestressed T-beams.

The arch action is significant in concrete members because of the large difference in the tensile and compressive strength of concrete [17]. The lower tensile strength causes

the cracking at lower load levels resulting in the shift of the neutral axis towards the compression zones. If the stretching (outward movement) of the member is restrained by stiff boundaries, an internal arch action is generated in concrete members (figure 1.2) resulting in additional capacity.

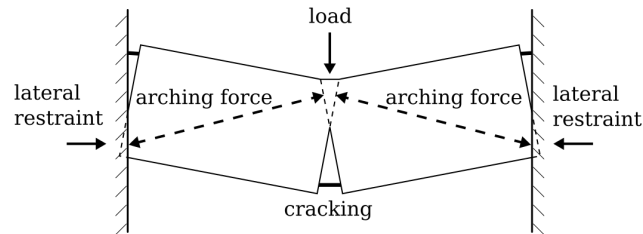


Figure 1.2: Arch action in concrete members

The arch action significantly increases the capacity of laterally restrained members in the ultimate limit state, especially in members with lower span-to-depth ratio and higher degree of lateral restraint [17]. Initially the slab behaves linear elastically before cracking (A to B), as the load is increased an elastic-plastic phase is reached (B to C) after which the capacity reduces as shown in figure 1.3.

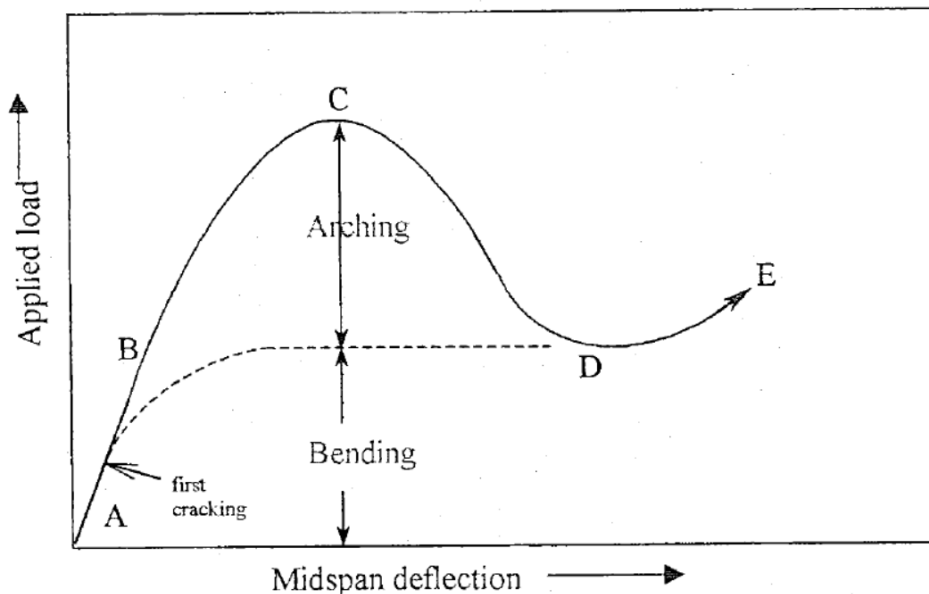


Figure 1.3: Influence of arch action on the load deflection response of concrete members [17]

The arching phenomenon has been recognized by engineers since 1909 and the development of the knowledge in this domain is comprehensively summarized in Guide to Compressive Membrane Action [17], but all of the research is mainly focused on the mechanism working transversely in the bridge deck slabs i.e. to study the phenomenon as shown in figure 1.4. It has been documented that the lateral restraint of deck slabs has beneficial effect on the flexural and punching shear capacities and this restraint is inherent to the design owing to presence of supporting beams, cross-beams and surrounding area of the

deck slab [17]. Therefore, some design standards have also incorporated this effect in the design philosophies.

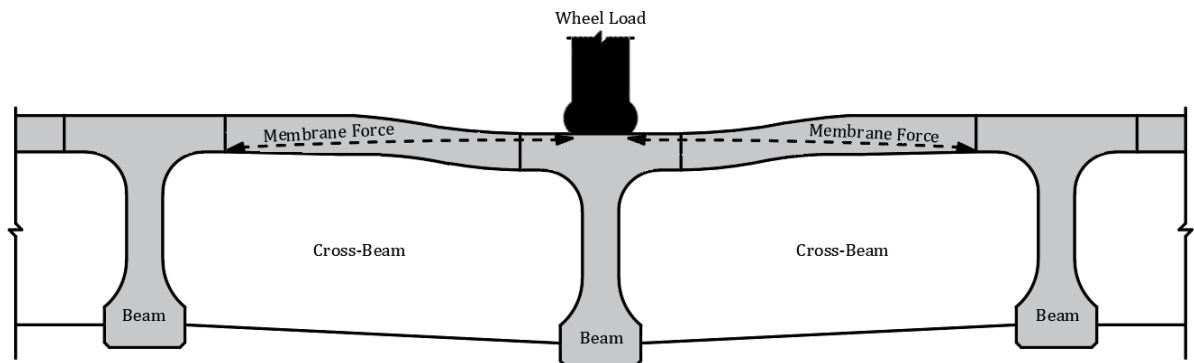


Figure 1.4: Compressive membrane action in bridge deck slabs

Although a lot of research has been conducted to understand the development of membrane action in bridge deck slabs in transverse direction, much work has not been done to investigate the similar mechanisms working longitudinally in the loaded beam as shown in figure 1.5. As the membrane action alone is not able to fully explain the enhanced capacities of T-beam bridges, it is expected that the contribution of the arch action in the loaded beam might also be a significant contributor in the bridges with intermediate cross-beams. The presence of cross-beams is vital for the development of this action as these provide the necessary external restraint.

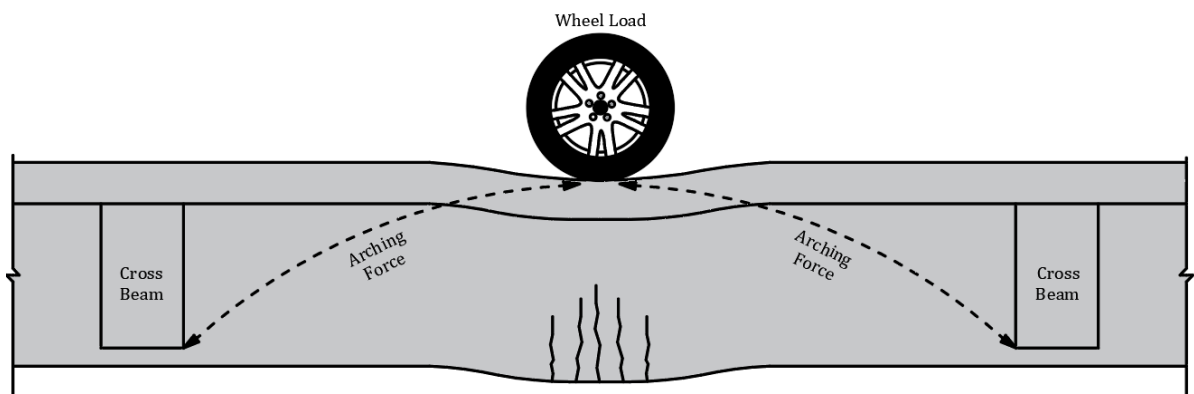
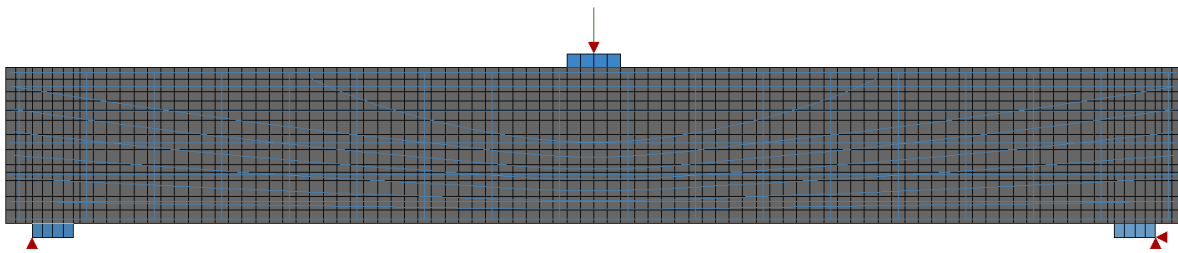


Figure 1.5: Arch action in T-beams

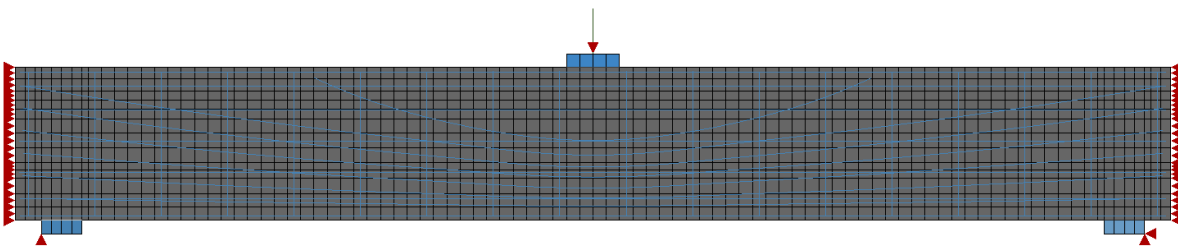
A number of publications can also be found investigating the same phenomenon in efforts to explain the progressive collapse of concrete frame structures [8, 19]. However the aim of the research at hand is to study the development of arch action in a single beam as part of a concrete bridge system (without considering the distribution of the load in transverse direction).

Owing to the lack of literature available for arching action in less slender concrete members, a trial beam model is developed to exhibit the effects of arching on the ultimate capacity of prestressed concrete beams. The trial beam is made by modeling the first and last 4m of the 24m long Vechtbrug beam (used as a case study in this project) and joining them

together, this gives a symmetric tendon profile and a beam span of 8m, which is also the distance between the cross-beams in Vechtbrug - this gives an idea of arch development in T-beams. The cross-section and reinforcement layout of the trial beam is shown in figure 1.8. The area of reinforcing bars is unaltered but the prestressing tendon area is reduced by one-third to allow for the yielding of the tendons. The material properties and the analysis set-up for the trial analysis is the same as described in chapter 6 of the report. A simply supported and a fully restrained model is developed to visualize the effect of arching on the ultimate capacity of the beam as shown in figure 1.6.



(a) Simply supported trial beam model



(b) Fully restrained trial beam model

Figure 1.6: Trial beam models

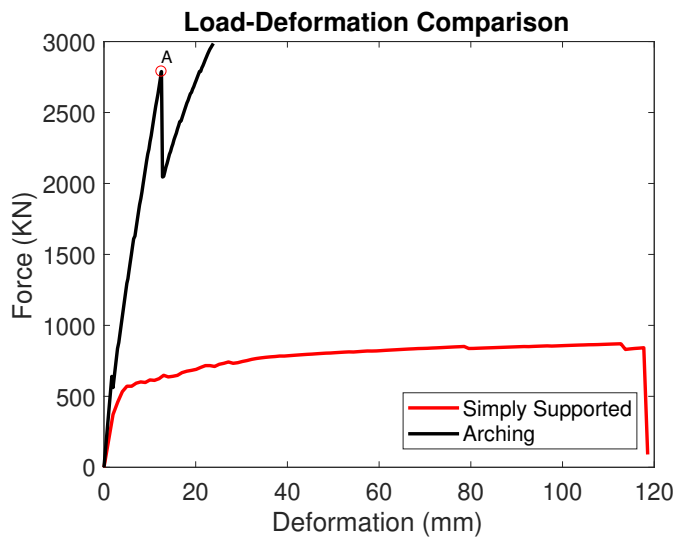


Figure 1.7: Comparison of fully restrained and simply supported trial beam

The load-deformation response of the simply supported and fully laterally restrained trial beam can be seen in figure 1.7, which shows that the lateral restraint almost increases

the capacity of the beam by a factor of 3, when estimated using the point marked A, proving that significant arch action can be expected in the Vechtbrug beam. However, the ductility of the beam is significantly reduced.

1.2. Scope and Objectives of Research

This MSc. project is part of a larger PhD project which is aimed at explaining the differences in experimental and analytical estimation of prestressed T-beam bridge capacity, treating the bridge as a structural system whereas the scope of this MSc. project is limited to the structural response of a single beam i.e. the distribution of the load in transverse direction is completely neglected.

As the project is aimed to also analytically quantify the arch action in T-beams loaded with point loads, the scope of the project covers the validation of the approximate analytical model to quantify arch action in underwater concrete slabs suggested in CUR-Recommendation 077 [2] and its extension to beams with T-shaped cross-sections. The effect on arching capacity of varying the load location along the length of the beam is also studied.

As a case study, Ensink performed experiments on Vechtbrug [13] near the Eastern border of the Netherlands. These experiments include the tests on individual beams of Vechtbrug and tests on beams as part of the bridge system. For this project, the scope is limited to the development and validation of 2D, 2.5D and 3D numerical models for an individual beam of Vechtbrug. The cross-section of the Vechtbrug beam is shown in figure 1.8.

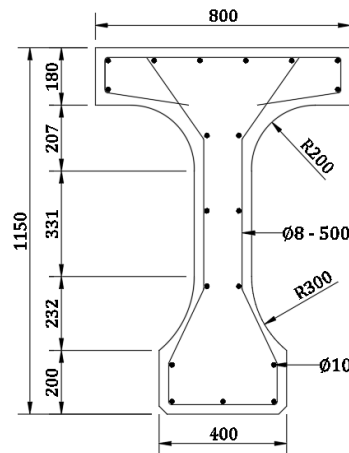


Figure 1.8: Cross-section of Vechtbrug beam

The comparison is also to be made with the behavior of beam as part of bridge system but the distribution of the load in transverse direction is not taken into account as the scope is limited to the development of arch action in the longitudinal direction of the beam only.

The objective of this research is to understand if the arch action also develops in concrete beams as part of the bridge system due to lateral restraint offered by the cross-beams (ignoring the distribution of load in transverse direction) and if the arching capacity can be estimated using the adapted analytical approach. It is believed that the arch action working longitudinally will also help in explaining the higher capacity of such bridges in addition to CMA working in the transverse direction but this is beyond the scope of this MSc. project.

1.3. Research Hypothesis

As the scope of this project is only a single beam acting as part of the bridge system, the hypothesis can be summarized as:

"The development of arch action in prestressed concrete beams as part of the bridge system can also be modeled using a single beam and appropriate boundary conditions"

1.3.1. Research Questions and Methodology

1- How sensitive is the numerical arching capacity of (prestressed) concrete beams to the slenderness ratio, stiffness of end restraint and amount of prestressing for beams loaded with uniformly distributed load (UDL) and how sensitive is the numerical arching capacity of beams to the point of application of load for beams loaded with concentrated loads?

- A finite element model with rectangular cross-section loaded with UDL is used to study the effect of slenderness ratio, stiffness of lateral restraint and amount of prestressing on the numerical arching capacity of concrete beams.
- A similar finite element model is developed with point load to study the effect of varying load location on the arching capacity.
- As the main aim is to understand arch action in T-beams, a finite element model of T-beams is developed with both, UDL and point load.

2- Is the approximate analytical model, suggested in CUR-077, able to predict the arching behavior in good accordance with the results of non-linear finite element analysis for rectangular beams loaded with uniform loads? Can this model be extended to beams with point loads and beams with T-shaped cross-sections?

- CUR-Recommendation 077 [2] provides a method for the estimation of the membrane action developed in thick underwater concrete slabs loaded with uniformly distributed loads (UDL). This model is adopted as it is most comparable with the situation at hand i.e. beam with long span and significant height as most of the known analytical methods for arching capacity are for slender short span slabs.
- The approximate analytical model is validated using the results of non-linear finite element analysis for varying parameters.
- The ideology of the adopted analytical model is extended to the beams loaded with point loads and beams with T-shaped cross-sections and the results are compared with the results of finite element analyses.

3- Is it possible to model the arching behavior of a single beam as part of bridge system using an individual beam model and the loaded sub-span only, given that the transverse distribution of load is not taken into account?

- 2D, 2.5D and 3D numerical models of the Vechtbrug beam are developed and verified by comparing the load-deformation response with the results of experiments conducted by Ensink. The 3D model is developed as it allows a more realistic modeling of end restraints for torsional behavior of end cross-beams. Efforts are also made to develop a relatively cheap numerical model using a combination of shell and brick elements.
- The verified model is then used to determine the numerical arching capacity of the central sub-span of the beam. The results of this analysis are compared with

the beam as part of the bridge system (ignoring the distribution of the load in transverse direction) and the adapted analytical model developed for T-beams with point loads.

As all the methods discussed in guide to compressive membrane action [17] focus on the mechanism working transversely in the bridge deck slabs and have certain conditions which need to be satisfied for their application, most of them cannot directly be used for beams which are much deeper and have longer spans. Therefore, an approximate analytical method is used in this research as suggested in CUR Recommendation 077 (Calculation rules for un-reinforced underwater concrete floors [2]) for determination of the arching capacity of underwater concrete floors. This is an approximate and easy to apply approach to analytically estimate the effect of arch action in concrete members with significant heights. A detailed account explaining the approximate analytical model can be found in chapter 2 and this approach is referred to as the CUR method throughout the report. In the first phase, the estimated results of arching capacity using CUR method are compared with the numerical capacities obtained using non-linear finite element analysis (NLFEA) and sensitivity analyses are performed varying slenderness of the beam, stiffness of end restraint and initial prestressing in the system. These sensitivity analyses help to verify the adopted analytical model and also to understand the development of arch action in concrete beams. The verified analytical model is then extended to beams loaded with point loads and beams with T-shaped cross-sections.

In the second phase, the finite element model of Vechtbrug beam is validated using the experimental results and efforts are made to apply similar theories and modeling techniques to model arch action. The results of a single beam model are then compared with the full bridge model with disconnected slab to avoid the influence of membrane action.

Part-I Sensitivity Analysis and Extension of CUR Method

This part of the report discusses the approximate analytical (chapter 2) and the numerical (chapter 3) approach to study the sensitivity of span-to-depth ratio, stiffness of horizontal restraint and initial prestressing on the development of arch action in a concrete beam model loaded with uniformly distributed load. The analytical model is then extended to beams loaded with point load and for beams with T-shaped cross-section. In chapter 4, the results of the sensitivity analysis are discussed and the boundary conditions for the applicability of the modified CUR method are outlined.

2

Analytical Model

This chapter describes, in detail, the approximate analytical method used for the sensitivity analysis with the necessary assumptions to make a reasonable comparison with the numerical models. The numerically verified model is then extended to beams loaded with concentrated loads and beams with T-shaped cross-sections.

2.1. Background and Description of the Analytical Model

CUR Recommendation 077 (Calculation rules for unreinforced underwater concrete floors [2]) recommends an approximate analytical model to estimate the arching capacity of unreinforced underwater concrete floors in relation to the horizontal restraint available at the edges of the slab due to surrounding retaining walls and soil pressure. This analytical approach has been referred to as "CUR method" throughout the report. As this formulation is derived for the underwater concrete floors, the loading assumed is an upward uniformly distributed load (UDL) due to water pressure on the slab and for the development of arch action the concrete has to crack at the center and at the supports. First the method has been described as mentioned in the CUR recommendations and then the assumptions made for comparison with numerical model are outlined.

The starting point for the method is the force distribution in the beam in an un-deformed state as shown in figure 2.1. The force F_0 is the initial horizontal force present in the system due to the soil pressure around the retaining wall. After cracking compressive zones are assumed to develop at supports and at mid-span. These compressive zones are assumed to be plastic hinges connected by infinitely rigid rods i.e. the shortening of the strut due to membrane force is ignored. To be conservative a triangular stress distribution is assumed at the locations of the plastic hinges as shown in figure 2.1 - sufficient rotation capacity of the system is assumed. As shown in figure 2.1, the line of action of force runs through the centroid of triangular stress blocks. The laying of underwater concrete is rather difficult so, the calculations are based on the average height of the concrete slab, taking into account the tolerances at the bottom and top of the slab labeled tol_1 and tol_2 in figure 2.1 respectively. The maximum stress at the supports is also modified using a factor $\beta = 0.60$ because at the supports the complete width of the slab is not activated. Note that for underwater concrete the supports are the anchors/piles spaced in the short direction of the slab. The slab is in equilibrium as the upward pressure force is resisted by the membrane force and the internal lever arm.

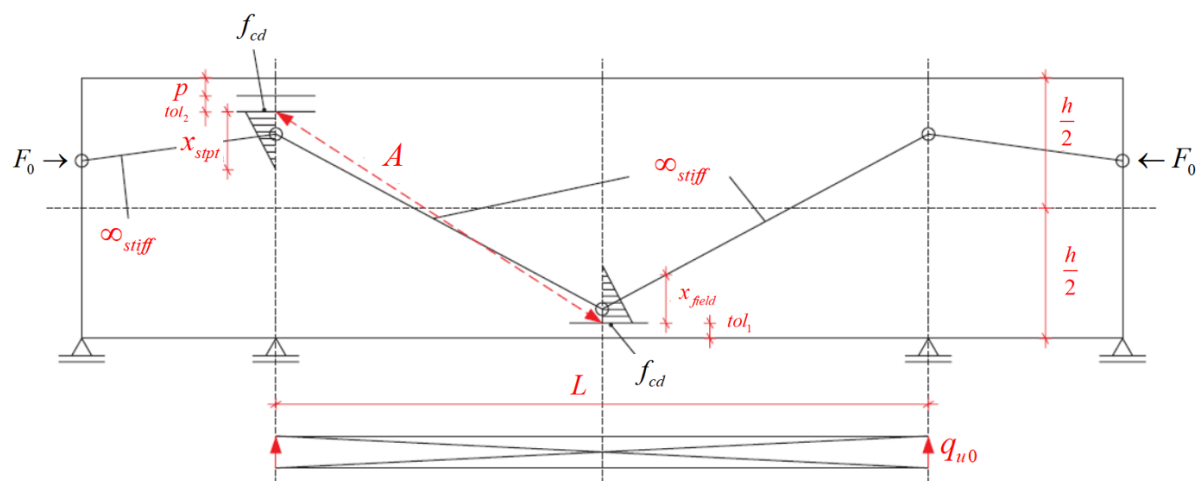


Figure 2.1: CUR method - undeformed state

Once the load starts to increase, the mechanism wants to stretch as shown in figure 2.2. This causes an increase in the membrane force due to lateral restraint, a decrease in the internal lever arm due to vertical deformation and the increase in height of compressive

zones. The reduction in the internal lever arm due to vertical deformation is included in the analytical model to take into account the effects of geometrical non-linearity. However, only the rigid body rotation of the slab is accounted for and the vertical deformation due to bending and shortening of the strut is ignored. The stretching of the floor also causes an increase in the span of the loaded slab and this has also been taken into account while calculating the arching capacity.

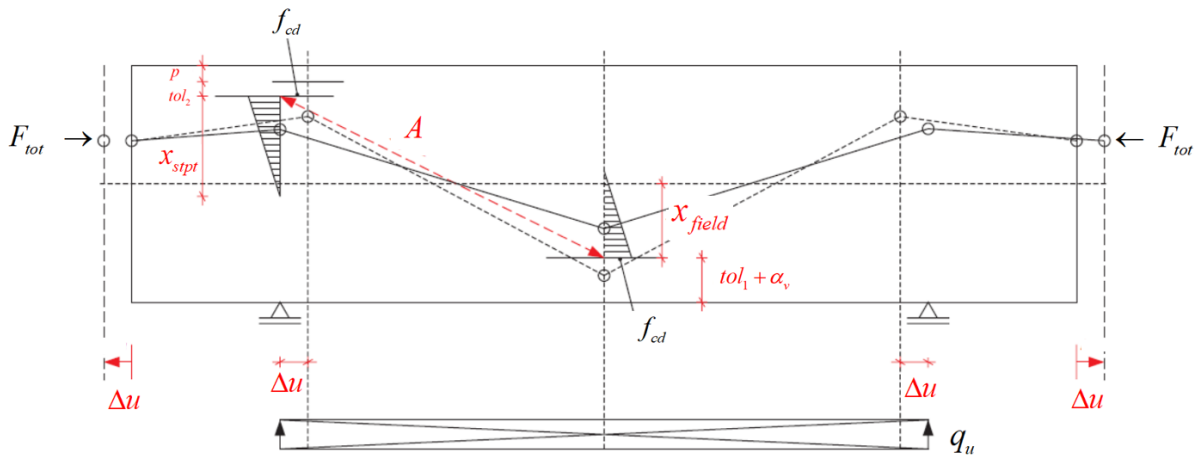


Figure 2.2: CUR method - deformed state

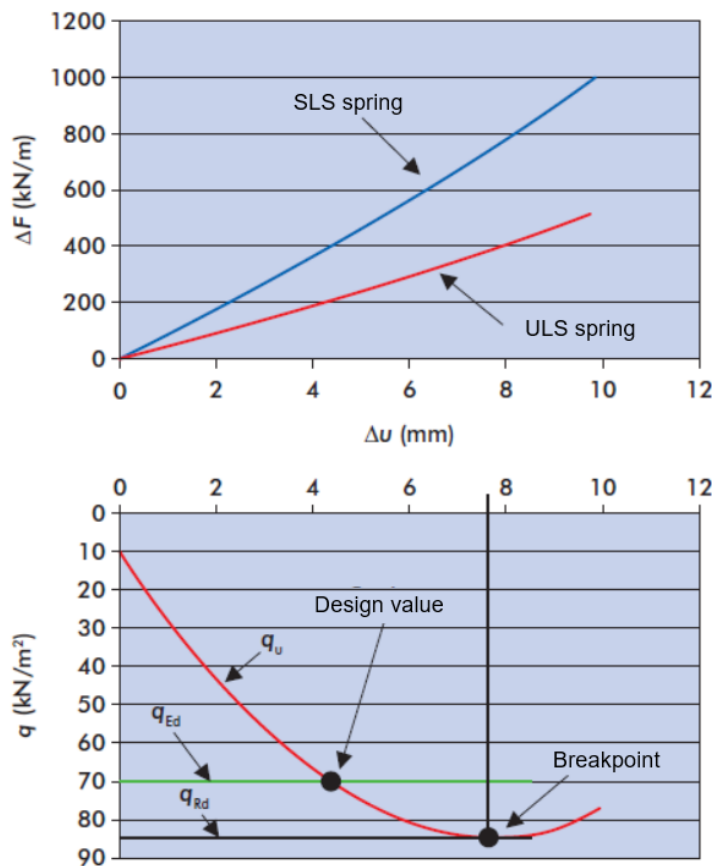


Figure 2.3: CUR formulation (spring and load capacity) [2]

It is assumed that the relationship between the development of the membrane force and outward stretch of the slab is linear elastic and can be related through a spring constant (k) as shown in figure 2.3. A typical capacity vs horizontal deformation graph is also shown.

The CUR method is derived for underwater concrete floor systems so it assumes a unit width (1m) of the floor slab in all the calculations. The CUR recommendation also provides a step by step procedure to determine the arching capacity of un-reinforced underwater concrete floor, as described in the following set of equations.

$$\begin{aligned}
 (a) \Delta F &= k(\Delta u) \\
 (b) F_{tot} &= F_0 + \alpha_{rN} \cdot \Delta F \\
 (c) x_{field} &= \frac{2 \cdot F_{tot}}{b \cdot f_{cd,pl}} \\
 (d) x_{stpt} &= \frac{2 \cdot F_{tot}}{0.6 f_{cd,pl} \cdot b} = \frac{x_{field}}{0.6} \\
 (e) A^2 &= (h - tol_1 - tol_2 - p)^2 + \left(\frac{L_x}{2}\right)^2 \rightarrow A \\
 (f) A^2 &= (h - tol_1 - tol_2 - p - \alpha_v)^2 + \left(\frac{L_x}{2} + \Delta u\right)^2 \rightarrow \alpha_v \\
 (g) z &= h - tol_1 - tol_2 - p - \frac{x_{field}}{3} - \frac{x_{stpt}}{3} - \alpha_v \\
 (h) q_u &= \frac{8 F_{tot} z}{(L_x + 2 \Delta u)^2}
 \end{aligned}$$

Where,

F_0	is the initial horizontal force due to soil pressure on the system
ΔF	is the increase in the membrane force due to stretching of the system
F_{tot}	is the total horizontal (membrane) force in the system
α_{rN}	is a reduction factor depending on the pressure head
x_{field}	is the height of compressive zone at the location of maximum bending moment
x_{stpt}	is the height of compressive zone at the supports
A	is the length of the active compressive strut
b	is the width of the concrete member (assumed 1 m)
tol_1	is the tolerances at the bottom of the concrete floor
tol_2	is the tolerances at the top of the concrete floor
p	is the distance from top of the floor to the support/dish
L_x	is the span between the compressive zones at the sides
α_v	is the vertical deformation as a result of stretching of the system
Δu	is the horizontal deformation as a result of stretching of the system
z	is the internal lever arm of the system
q_u	is the ultimate load that can be resisted by the system in KN/m/m

2.2. Simplified Analytical Model - UDL

The method is now to be adapted for the concrete beams, hence a few simplifications are made in the model to make the comparison with the numerical model. The list of simpli-

fied equations with the explanation are also listed.

Modifications:

1. F_0 is assumed to be zero as there is no soil pressure or external load on the beam. In case of application of prestressing load, the prestressing force is taken as F_0 in the analytical model.
2. α_{rN} , the reduction factor, is ignored as there is no pressure head in case of the beam.
3. x_{field} is assumed equal to x_{stpt} for the horizontal equilibrium of the system. Furthermore, the numerical model is restrained throughout the height on the edges so the complete width is activated at support level unlike in the case of underwater concrete floor.
4. All the tolerances are ignored as the geometry of a beam is well-defined when compared to underwater concrete slabs.

$$\begin{aligned}
 (a) \Delta F &= k(\Delta u) \\
 (b) F_{tot} &= F_0 + \Delta F \\
 (c) x_{field} &= \frac{2 \cdot F_{tot}}{b \cdot f_{cd,pl}} \\
 (d) x_{stpt} &= \frac{2 \cdot F_{tot}}{b \cdot f_{cd,pl}} = x_{field} \\
 (e) A^2 &= (h)^2 + \left(\frac{L_x}{2}\right)^2 \rightarrow A \\
 (f) A^2 &= (h - \alpha_v)^2 + \left(\frac{L_x}{2} + \Delta u\right)^2 \rightarrow \alpha_v \\
 (g) z &= h - \frac{x_{field}}{3} - \frac{x_{stpt}}{3} - \alpha_v \\
 (h) q_u &= \frac{8F_{tot}z}{(L_x + 2\Delta u)^2}
 \end{aligned}$$

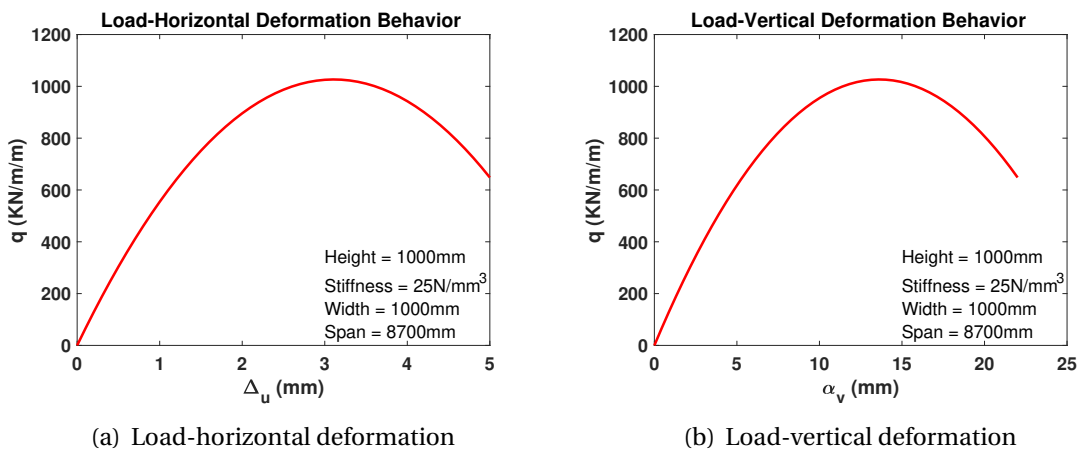


Figure 2.4: Typical results of CUR method

This simplified set of equations is used for analytically calculating the arching capacity of the beams for comparison with the numerical model. To calculate the analytical capacity

of all the variants, an excel worksheet is produced with interlinked formulae so a parametric study can be performed. Typical load-deformation graphs obtained using CUR method are shown in figure 2.4.

2.3. Modified Analytical Model - Point Load

The CUR method is derived for uniformly loaded slabs, as that is the loading scenario for underwater concrete floors but it is of interest to check the applicability of method for beams loaded with point loads. The effect of varying the location of point load with respect to the support is also to be studied.

Following the results of the numerical analysis, it is observed that due to application of the point load, there is a localization of stresses at the point of application of load. This causes the concrete to reach its compressive strength (plasticity) earlier at the point of application of load than at the supports - this can be seen in figure 4.18. A pictorial representation of stresses in beam loaded with a point load is shown in figure 2.5. This must be noted that the length of the active strut also needs to be adapted depending on the location of the load. Although CUR assumes that plasticity would occur at both the edges but due to eccentric loading this is not the case and all the calculations are based on the distance between the load and the nearest support (part a), assuming that the horizontal equilibrium will ensure similar behavior in terms of membrane force for the other side (part b).

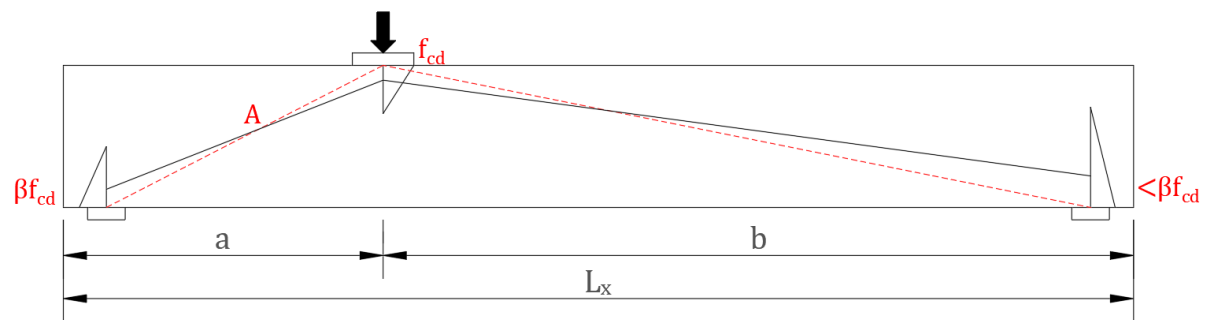


Figure 2.5: Modified CUR method - point load

The results of the numerical analysis show that when the point load is at the mid-span, the ratio of compressive stress at the supports and at center is around 50-60% - to be conservative this is assumed to be 50% for the analytical model. This stress ratio is taken into account by the factor β in figure 2.5. As the load moves closer to the support the stresses at the support increase (figure 4.17) but the contribution of these stresses in the membrane force i.e. the area under the plot in figure 4.17 remains the same. Therefore the factor β is assumed to have a constant value of 0.50 for all the load locations.

$$\beta = 0.50 \quad (2.1)$$

Furthermore, due to eccentric loading the horizontal stretch of the model is not symmetric on both sides. To take this into account the relative stretch of the part b is calculated assuming infinitely rigid struts as assumed in the original model. In the equations, the stretch of part a and part b is referred to as Δu_1 and Δu_2 respectively. The relation between Δu_1 and Δu_2 is shown in equation (2.2).

$$\Delta u_2 = -b + \sqrt{2a\Delta u_1 + b^2 + \Delta u_1^2} \quad (2.2)$$

In light of the discussion above, the following set of equations is derived for the prediction of the analytical capacity of restrained beams loaded with point load.

$$\begin{aligned} (a) \Delta F &= k(\Delta u_1) \\ (b) F_{tot} &= F_0 + \Delta F \\ (c) x_{field} &= \frac{2 \cdot F_{tot}}{b \cdot f_{cd,pl}} \\ (d) x_{stpt} &= \frac{2 \cdot F_{tot}}{b \cdot \beta f_{cd,pl}} = \frac{x_{field}}{\beta} \\ (e) A^2 &= (h)^2 + (a)^2 \rightarrow A \\ (f) A^2 &= (h - \alpha_v)^2 + (a + \Delta u_1)^2 \rightarrow \alpha_v \\ (g) z &= h - \frac{x_{field}}{3} - \frac{x_{stpt}}{3} - \alpha_v \\ (h) F_u &= \frac{F_{tot} z (L_x + \Delta u_1 + \Delta u_2)}{ba} \end{aligned}$$

2.4. Modified Analytical Model - T-Beam with UDL

The CUR method is derived for slabs so it assumes a unit width for all the calculations but as the Vechtbrug beam has a T-shaped cross-section, the applicability of CUR method for such beams is also of interest. A simple T-shaped cross-section is assumed for this purpose as shown in figure 2.6 and the working mechanism is illustrated in figure 2.7.

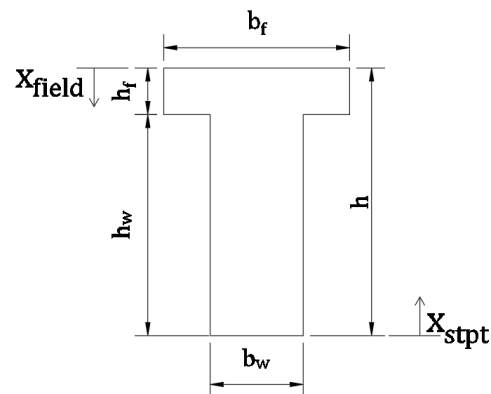


Figure 2.6: T-beam cross-section

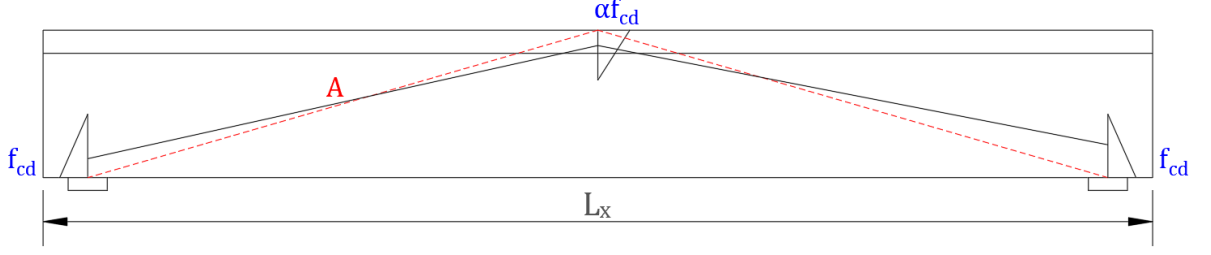


Figure 2.7: Modified CUR method - T-beams with UDL

In the previous approaches for uniformly loaded beams, it has been assumed that the height of the compressive zone at mid-span and at support level is equal, given the rectangular shape of the cross-section. In case of T-beam however, this assumption is not valid. This has been taken into account by using a piecewise function for the calculation of the height of compressive zones. It can be assumed that the compressive stress in web would always reach compressive strength of concrete, owing to its lower width compared to the flange, hence the height of compressive zone at the support level can be calculated using equation (2.3).

$$x_{stpt} = \begin{cases} \frac{2 \cdot F_{tot}}{f_{cd,pl} b_w} & x_{stpt} < h_w \\ \frac{b_f h_w f_{cd,pl} + b_w f_{cd,pl} h_w + F_{tot} + \sqrt{-b_f b_w f_{cd,pl}^2 h_w^2 + b_w^2 f_{cd,pl}^2 h_w^2 + 2 F_{tot} b_f f_{cd,pl} h_w - 2 F_{tot} b_w f_{cd,pl} h_w + F_{tot}^2}}{f_{cd,pl} b_f} & h_w < x_{stpt} < h \end{cases} \quad (2.3)$$

On the other hand, the stress in concrete at mid-span might be lower due to the wider flange. To account for this, the factor α is introduced. The height of compressive zone at the center can then be calculated following equation (2.4).

$$x_{field} = \begin{cases} \frac{2 \cdot F_{tot}}{(\alpha f_{cd,pl}) b_w} & x_{field} < h_f \\ \frac{-b_f h_f (\alpha f_{cd,pl}) + b_w h_f (\alpha f_{cd,pl}) + F_{tot} + \sqrt{-b_f^2 h_f^2 (\alpha f_{cd,pl})^2 - b_f b_w h_f^2 (\alpha f_{cd,pl})^2 - 2 F_{tot} b_f h_f (\alpha f_{cd,pl}) + 2 F_{tot} b_w h_f (\alpha f_{cd,pl}) + F_{tot}^2}}{(\alpha f_{cd,pl}) b_w} & h_f < x_{field} < h \end{cases} \quad (2.4)$$

The factor α has been derived based on the results of numerical analysis and the ratio of web to flange width. The expression of α is expressed in equation (2.5).

$$\alpha = \frac{0.8 b_w}{b_f} + 0.4 < 1.0 \quad (2.5)$$

The maximum value of α is limited to 1.0 as for any given combination of web and flange width, concrete cannot go beyond its compressive strength. The equations for the compressive zone height have been derived based on the maximum force that can be resisted by flange or web of the cross-section assuming that the extreme fiber reaches a certain stress level and a triangular stress distribution. A typical plot for estimation of compressive zones is also shown in figure 2.8, where it can be seen that because of wider flange the compressive zone at mid-span initially grows less steeply and then rapidly as the zone enters the thinner web of the cross-section and vice versa for the compressive zone at the supports.

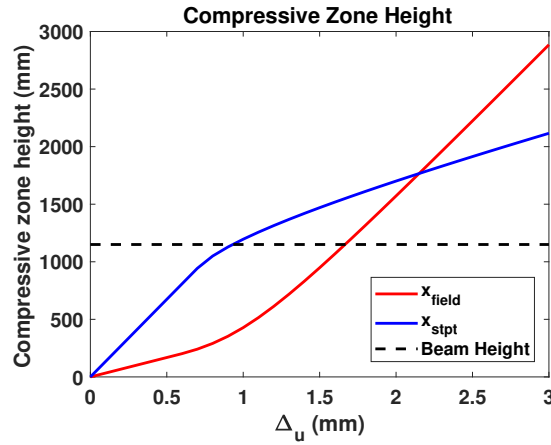


Figure 2.8: Compressive zone height for T-beams loaded with UDL

The rest of the CUR formulation remains unchanged as described in section 2.2 because a uniformly distributed load is applied. The point of application of the membrane force at mid-span and at supports has been calculated following the triangular stress distribution and the beam geometry.

2.5. Modified Analytical Model - T-Beam with Point Load

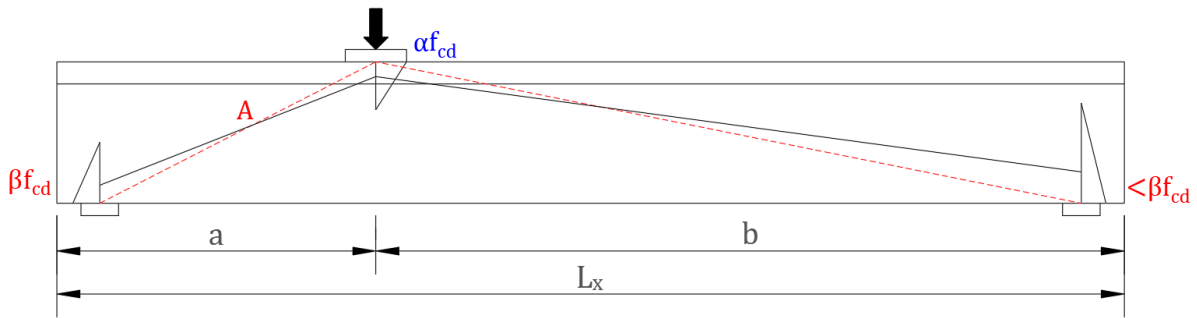


Figure 2.9: Modified CUR method - T-beams with point load

As the main goal of the project is to try and apply the approximated analytical method to estimate the arching capacity of the Vechtbrug beam loaded with a point load, the two previously discussed models (Point Load (section 2.3) and T-Beam with UDL (section 2.4)) are combined together. It must be noted that with the application of point load the concentration of stresses meant that the factor α can be assumed as 1.0 but the factor β needs to be adjusted based on the ratio of web and flange width. The factor β is also modified based on the results of the numerical analysis and is expressed in equation (2.6). The height of compressive zones can then be calculated as described in equation (2.7) and equation (2.8).

$$\beta = 1.25 - 0.8 \frac{b_w}{b_f} < 1.0 \tag{2.6}$$

$$x_{field} = \begin{cases} \frac{2F_{tot}}{(\alpha f_{cd,pl})b_f} & x_{field} < h_f \\ \frac{-b_f h_f (\alpha f_{cd,pl}) + b_w h_f (\alpha f_{cd,pl}) + F_{tot} + \sqrt{-b_f^2 h_f^2 (\alpha f_{cd,pl})^2 - b_f b_w h_f^2 (\alpha f_{cd,pl})^2 - 2F_{tot} b_f h_f (\alpha f_{cd,pl}) + 2F_{tot} b_w h_f (\alpha f_{cd,pl}) + F_{tot}^2}}{(\alpha f_{cd,pl})b_w} & h_f < x_{field} < h \end{cases} \tag{2.7}$$

$$x_{stpt} = \begin{cases} \frac{2F_{tot}}{(\beta f_{cd,pl})b_w} & x_{stpt} < h_w \\ \frac{b_f h_w (\beta f_{cd,pl}) - b_w h_w (\beta f_{cd,pl}) + F_{tot} + \sqrt{-b_f b_w h_w^2 (\beta f_{cd,pl})^2 + b_w^2 h_w^2 (\beta f_{cd,pl})^2 + 2F_{tot} b_f h_w (\beta f_{cd,pl}) - 2F_{tot} b_w h_w (\beta f_{cd,pl}) + F_{tot}^2}}{(\beta f_{cd,pl})b_f} & h_w < x_{stpt} < h \end{cases} \quad (2.8)$$

The combined equations also show a smooth and expected growth of the concrete compressive zones as shown in figure 2.10. The rest of the steps followed for the analysis are the same as described in section 2.3. It must be noted that the length of compressive strut (A in figure 2.9) is also varied for different load locations and the point of action of membrane force is determined using a triangular stress distribution and beam geometry.

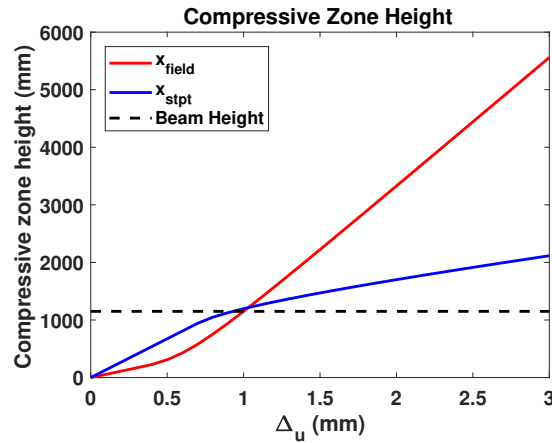


Figure 2.10: Compressive zone height for T-beam loaded with point load

3

Numerical Model

This chapter describes, in detail, the numerical model used for the sensitivity analysis to make comparison with the results obtained using the CUR and modified CUR approaches as described in the previous chapter. For all the models DIANA 10.2 has been used.

3.1. Description of the Numerical Model

In recent years, the use of non-linear finite element analysis (NLFEA) has become more common in engineering practices because of the improved speed of calculation and better understanding of structural behavior. One of the main applications of the non-linear finite element analysis is analysis of existing structures which is one of the main aims of the project. For all the non-linear analysis in this report, DIANA 10.2 (release date: 2018-11-13) is used.

As the numerical capacity of the beams is to be compared with the results of the analytical model, a finite element model is produced with similar assumptions. To also study the effect of initial prestress and presence of prestressing tendons, four variations of the model are produced in total.

1. Plane Cement and Concrete model with ideal (elastic-plastic) behaviour in compression (referred to as PCC ideal model) - this is an un-reinforced concrete model as assumed in CUR formulation with very similar compressive behavior.
2. Plane Cement and Concrete model with parabolic behaviour in compression (referred to as PCC parabolic model) - this is an un-reinforced concrete model as assumed in CUR formulation with a more realistic compressive behavior.
3. Un-reinforced concrete model but with central initial prestressing applied as external load (referred to as the compression model) - this model helps in understanding the effect of initial compression on the concrete without the presence of tendons.
4. Prestressed model with central prestressing applied using equally spaced tendons throughout the height of the structure (referred to as the prestressed model) - this model includes the effect of presence of prestressing tendons in the system.

All the models except the PCC ideal model have parabolic compressive behavior as suggested in RTD 1016-1:2017 [10].

3.2. Geometry of the Model

All the models are produced in 2D environment using regular plane stress elements and have a total length of 8700mm from edge to edge with 400mm support plates at 350mm from each edge giving a span of 8000mm, equivalent to the span of interest in the Vechtbrug beam. A typical model is shown in figure 3.1.

All the models have unit width (1000mm) as it is one of the assumptions of the CUR method. The support plate width is also equal to the width of the beam in all the models. For the generation of arch action, the horizontal restraint is one of the most important factors. Hence, to study the phenomenon both the extreme edges of the beam are restrained in the horizontal direction using linear elastic boundary interface. This interface allows the cracking of the beam at the top and the plasticity at bottom, which is the basic principle for the generation of arch action and one of the assumptions of the CUR method [2].

3.2.1. PCC Models

The PCC ideal model is produced as close as possible to the assumptions of the analytical model so a fair comparison can be drawn. To study the effect of a more realistic modelling of compression behavior the PCC parabolic model is also produced. A typical example of a

PCC model is shown in figure 3.1. There is no external load on the system at the beginning of the analysis.

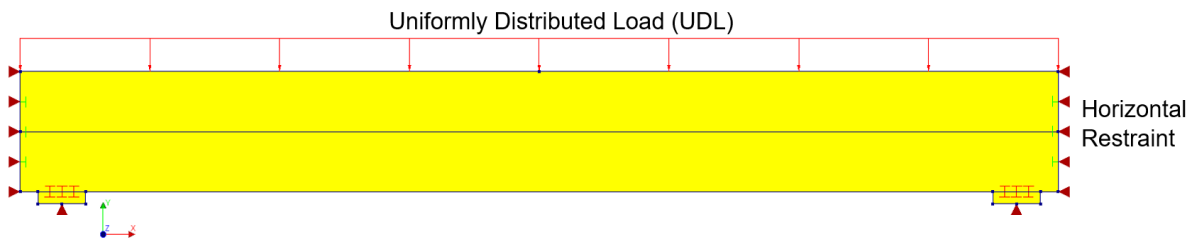


Figure 3.1: PCC model for numerical analysis

3.2.2. Compression Model

The compression model is produced to help understand the effect of initial prestressing on the system without the presence of the tendons. A phased analysis is used for this model. The initial prestressing is applied as an external load on the extreme edges of the model to give a uniform compression throughout the length of the beam in the first phase. During the application of prestressing the top fiber of the beam at mid-span is restrained in horizontal direction for stability of the system. A typical example of the compression model is shown in figure 3.2.

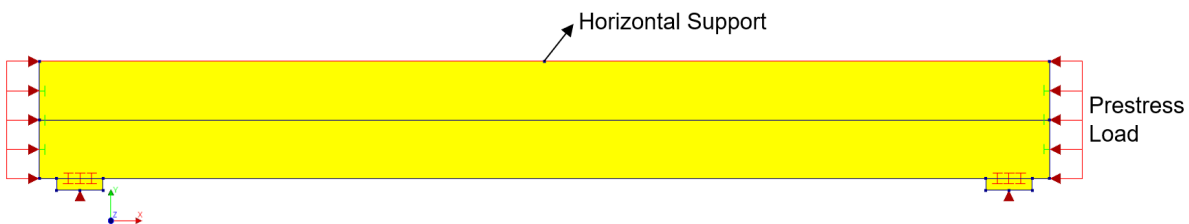


Figure 3.2: Compression model for numerical analysis

3.2.3. Prestressed Model

The prestressed model is a more realistic model compared to PCC and compression models because it has prestressing cables as embedded reinforcement for the application of initial prestress. To apply central prestressing, 5 tendons are equally spaced throughout the height of the beam and the prestressing load is applied using reinforcement bar prestress option in DIANA. All the tendons have the same cross-sectional area equal to 924 mm^2 . Similar to the compression model, a phased analysis is performed with an additional horizontal support in the first phase for stability of the system. A typical example of the prestressed model is shown in figure 3.3.

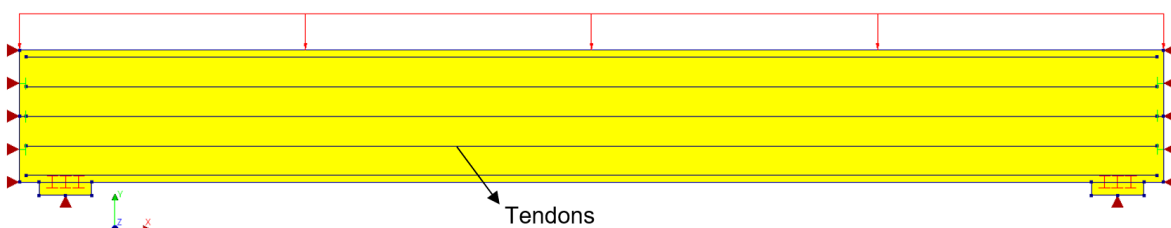


Figure 3.3: Prestressed model for numerical analysis

3.2.4. Point Load Model

This is an additional model produced to study the applicability of the modified CUR formulation on the beams loaded with a concentrated load instead of a uniformly distributed load. Several modifications were required to the method suggested by CUR to compare the results of the numerical and analytical approaches. The modifications and the list of equations used can be found in section 2.3 of the report. For the application of the point load a 500mm long steel plate is added at the top of the beam as shown in figure 3.4.

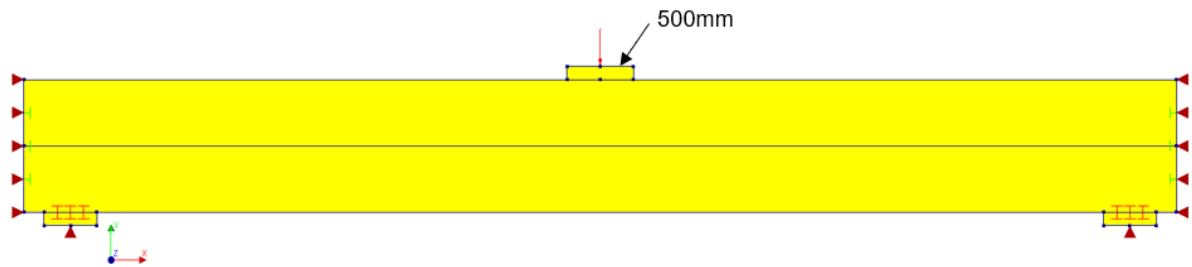


Figure 3.4: Point load model for numerical analysis

3.2.5. T-Beam Model (UDL)

All the models discussed previously are with rectangular cross-section but it is also essential to study the applicability of the modified CUR formulation on beams with T-shaped cross-section like the Vechtbrug beam. The CUR method does not specify any method for T-beams therefore some assumptions and modifications were made in the analytical model as mentioned in section 2.4 of the report. A typical T-beam model is shown in figure 3.5 and the cross-sectional details are discussed later in the report with results of the sensitivity analysis (section 4.7).

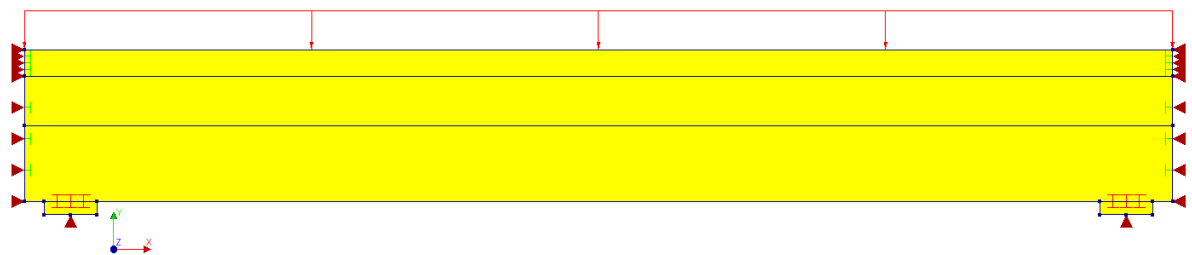


Figure 3.5: T-beam model with UDL

3.2.6. T-Beam Model (Point Load)

This model is a T-beam model loaded with point load which is the case for the Vechtbrug beam. Hence this model is closest to the loading scenario that is being studied. The necessary modifications required in the CUR model to be comparable to this case are discussed in section 2.5 of the report. A typical numerical model is also shown in figure 3.6.

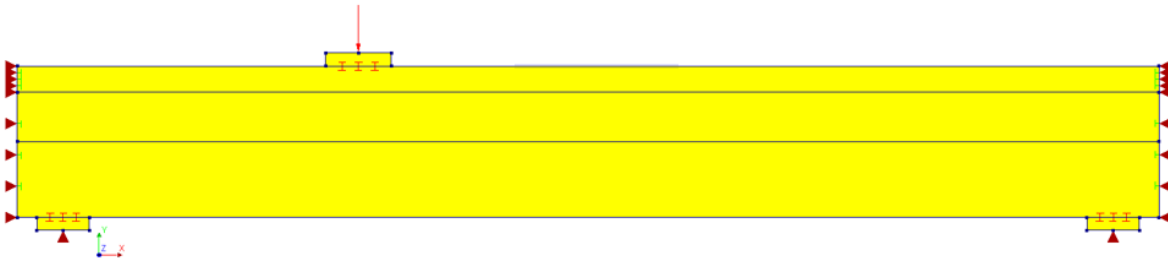


Figure 3.6: T-beam model with point load

3.3. Material Properties

The most important material models in these analyses are the compression and tensile behavior of concrete as all the relevant failures are either cracking of concrete in tension or crushing of concrete in compression. The behavior of concrete is quite complex given its heterogeneous nature, hence selection of an appropriate constitutive model is essential in performing the finite element calculations. For the prestressed model, the non-linear behavior of the prestressing cable is also important to model the plasticity, if any, in the tendons.

3.3.1. Concrete

DIANA 10.2 offers a number of options for modeling of concrete behavior in tension. Smeared cracking approach is used in all the models i.e. the crack opening is smeared over the element following a relation between concrete stress and crack opening which is a function of tensile fracture energy and crack band-width.

For these analyses Hordijk tension softening curve is used as suggested in the Guidelines for non-linear finite element analysis of concrete structures [10] and proposed by Hordijk, Cornelissen and Reinhardt [4, 11]. The material properties used in all the analysis are the design values for the concrete used in the Vechtbrug, the mean material properties of which are taken from the test results as mentioned in the material investigation report of the Vechtbrug [5]. The stress-strain relationship of concrete under tensile loading is as shown in figure 3.7.

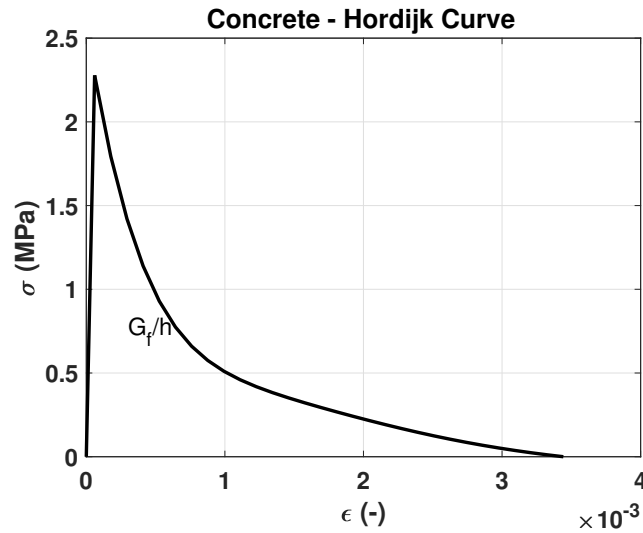


Figure 3.7: Tensile behavior of concrete

Similarly, in compression a number of constitutive relations are available in DIANA for concrete. As compression failure is the most important when studying the arch action, 2 compression curves are used (I) Ideal plastic (or elastic-plastic) behavior so a reasonable comparison can be drawn with the results of the analytical method and (II) Parabolic behavior so a more realistic compression failure can be modeled as suggested in RTD 1016-1:2017 [10]. Both the stress-strain relationships of concrete under compression are shown in figure 3.8. The inputs for the concrete behavior in DIANA are listed in table 3.1. Note that the material behavior plots have been created assuming a crack band-width of 100, which is equal to the prescribed element size.

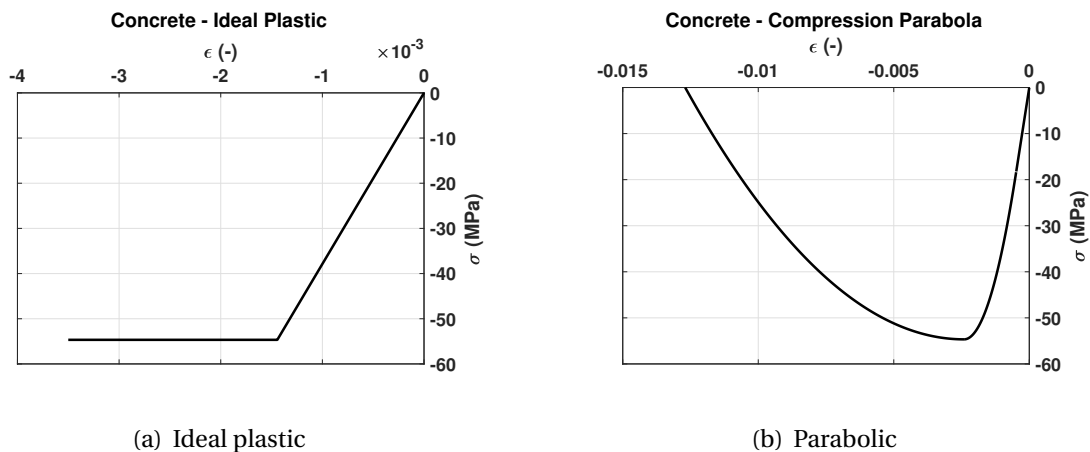


Figure 3.8: Compressive behavior of concrete

The Poisson ratio of concrete is assumed to be zero and the positive effects of confinement are ignored as these are also not taken into account by the analytical model. For the ideal plastic model the ultimate strain of concrete is assumed to be equal to 3.5 permille as shown in sub-figure (a) of figure 3.8.

Table 3.1: Properties of concrete in DIANA

Property	Value
Material class	Concrete and masonry
Material model	Total strain-based crack model
Young's modulus, E	37564 MPa
Poisson ratio, ν	0.00
Mass density	2400 kg/m^3
Crack orientation	Rotating
Tensile curve	Hordijk
Tensile strength, f_{ct}	2.26 MPa
Mode-I tensile fracture energy, G_f	0.149 N/mm
Crack band-width	Rots
Compressive curve	Parabolic/Ideal Plastic
Compressive strength, f_c	53.33 MPa
Compressive fracture energy	37 N/mm
Reduction model	Vecchio and Collins 1993
Lower bound reduction curve	0.40
Confinement model	No increase

3.3.2. Prestressing Steel

For the prestressed models where the tendons are also included for the application of prestressing loads, a tendon of type QP170 (used in Vechtbrug) is used as mentioned in the measurement report of Vechtbrug [13]. The stress strain relationship of the prestressing steel is shown in figure 3.9 with yielding strength of 1505MPa and fracture strength of 1770MPa.

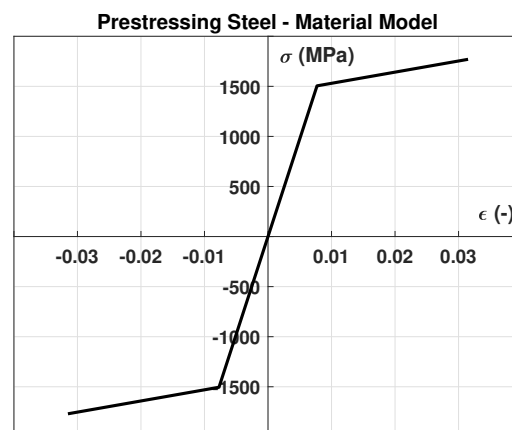


Figure 3.9: Prestressing steel material model

3.3.3. Boundary Interface at Edges

In CUR formulation [2] a discrete spring is assumed at the height of $h/4$ in the slab system (figure 2.2) while in DIANA a linear elastic boundary interface is used to model the end restraint to allow similar cracking and plasticity. As the application of the end restraint is

different in numerical and analytical model it has been assumed that half the height of concrete is always in compression - similar assumptions have also been made and verified by other researchers [18]. This allows the transformation of the linear spring interface into a point spring for comparison. The transformation function for the stiffness is expressed in equation (3.1).

$$k_{analytical} = k_{DIANA} * b * \frac{h}{2} \quad (3.1)$$

Where,

$k_{analytical}$ is the stiffness of discrete spring in analytical formulation [N/mm]

k_{DIANA} is the stiffness of linear spring in the numerical model [N/mm^3]

b is the width of the beam [mm]

h is the height of the beam [mm]

The stiffness of end restraint is related to the axial stiffness of the restrained member for the development of arch action. As a starting point it has been assumed that the end restraint stiffness should at least be equal to the stiffness of restrained member, hence the value chosen for end restraint is a bit higher than the axial stiffness of the slab following equations (3.2) and (3.3). In all the models this value is equal to $25 N/mm^3$ unless specified otherwise.

$$k_{axial} = \frac{E_c \cdot A_c}{0.5L_x} = \frac{37564 * 1000000}{4350} = 8.63 * 10^6 N/mm \quad (3.2)$$

$$k_{DIANA} = \frac{2 \cdot k_{axial}}{b \cdot h} = \frac{2 * 8.63 * 10^6}{1000000} = 17.27 N/mm^3 \quad (3.3)$$

Furthermore, in the analytical formulation, the system is stretching and Δu is defined as the outward stretching of the system while in the numerical model the horizontal deformation is an effect of both outward stretch of the system and rotation due to bending moment. Following the results, it is noticed that the axial stretch of the system is quite negligible compared to the rotation due to bending. Therefore, an average value of stretch has been taken following the same assumption that half the height is in compression as shown in equation (3.4).

$$\Delta u_{analytical} = \frac{\Delta u_{DIANA} + 0}{2} = \frac{\Delta u_{DIANA}}{2} \quad (3.4)$$

3.3.4. Plates and Plate Interface

In all the models, the support plates are modeled using linear elastic steel with Young's Modulus equal to 200GPa. To avoid the localization of stresses a linear elastic interface has been provided between the support plates and the beam. The properties of this interface have been derived based on the properties of concrete i.e the normal stiffness is equal to the Young's Modulus of concrete and the shear stiffness is equal to the Young's Modulus of concrete divided by 1000 as shown in table 3.2.

Table 3.2: Properties of interface between beam and plates

Property	Value
Normal stiffness	37564 N/mm^3
Shear stiffness	37.564 N/mm^3

For the point load model, a similar plate is also provided at the top with same material properties of steel and interface.

3.4. Composed Lines

Composed lines do not have any mechanical properties like mass or stiffness of their own and hence they do not influence the results of finite element model but they can be used as a post-processing tool.

To get the axial forces and bending moments in the system as an output, the composed line option has been used in DIANA. The composed lines integrate the stress outputs over the cross-section plane normal to the element itself to display the resulting forces and bending moments. By default, the stresses in the embedded reinforcement are also taken into account while integrating and this has not been changed.

In all the models a composed line element has been included at half the height of the beam with a radius of 2000mm i.e. it integrates all the stresses in this radius to give the required output.

3.5. Loads

As the analytical model is defined for the underwater concrete slabs which are loaded by a uniformly distributed upward load of water pressure, all the models are also loaded by a uniformly distributed load at the top fiber of the beam as shown in figure 3.1 except for the point load models. For the application of point load an additional steel plate is provided at the top of the beam and the load is applied as a vertex load at the center of the plate as shown in figure 3.4. The effects of self-weight of the beam are ignored in all the models.

3.6. Supports and End Restraint

The linear elastic steel plates are supported at mid-span of the bottom edge of the plate as shown in figure 3.1. This allows the rotation of the support plate under load without causing tensile stresses at the interface.

The edges of the beam are also restrained in horizontal direction using a boundary interface, necessary for the generation of arch action as shown in figure 3.1.

3.7. Mesh

Edge meshing with an element size of 100mm is specified in all the models and most of the elements are quadrilateral as shown in figure 3.10. Quadratic plane stress elements are used with compatible interface elements at the support plates and the edges. The elements used in the models are CQ16M, CT12M, CL12I and CL3CM as per the DIANA user manual [9].

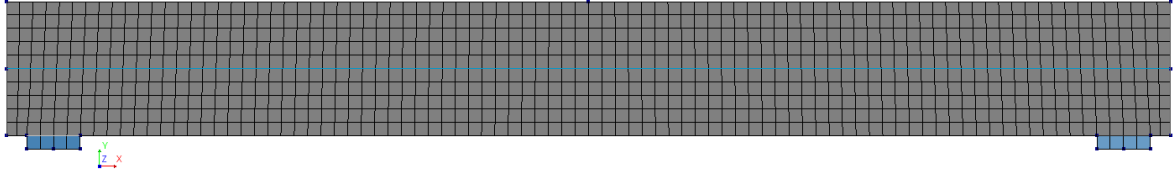


Figure 3.10: Typical mesh of the models

3.8. Analysis Procedure

All the analysis reported in this section are load-controlled analysis considering both physical and geometrical non-linearities as the analytical model also takes into account the geometrical non-linear effects. Full Newton Raphson method is used for all the analysis with a step size equal to 1.25 % of the capacity determined by the analytical model so all the analysis have more or less same number of load steps before failure. If the prestressing is to be applied, it has been done using a single load step in all the models.

For all the analysis a maximum of 100 iterations are used with the energy norm of tolerance equal to 0.001 as suggested by RTD 1016-1:2017 [10]. All the peak loads reported in the sensitivity analysis are the load values of the last load step before numerical failure which corresponds to the energy norm exceeding 1 %. A typical convergence behavior of the models discussed for the sensitivity analysis is shown in figure 3.11.

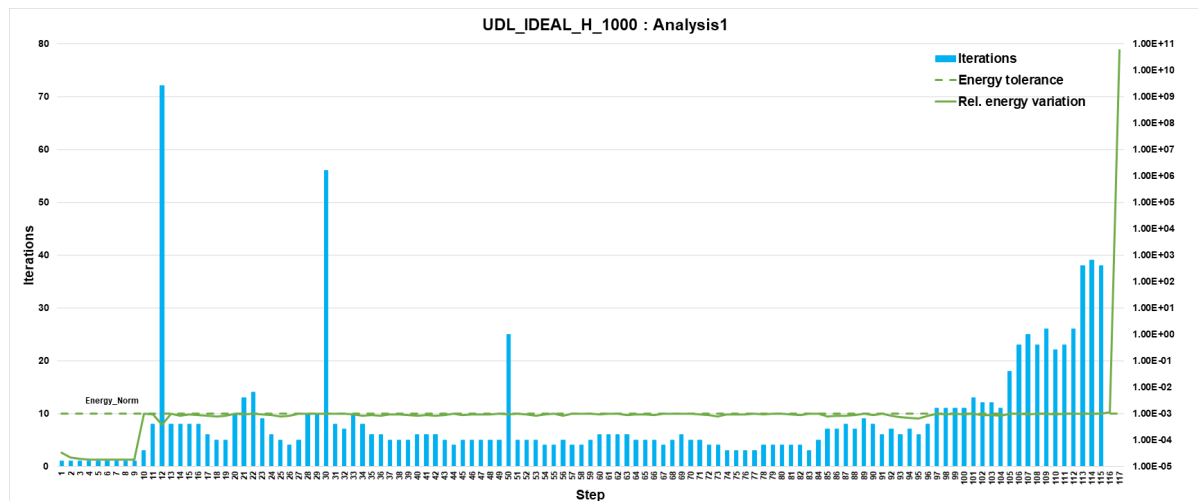


Figure 3.11: Typical convergence behavior of the models

4

Sensitivity Analysis (CUR and Modified CUR)

This chapter presents the results of the sensitivity analysis and compares the results of analytical and numerical calculations. Some conclusions are also drawn in light of the obtained results.

4.1. Sensitivity Analysis - General

As mentioned in the previous chapters, the sensitivity analysis is performed on all the variants i.e. the PCC model, the compression model and the prestressed model. The PCC model further has 2 variations, one using ideal plastic compressive behavior and the other with parabolic compressive curve as shown in figure 3.8.

The analysis are allowed to run until numerical failure (energy norm exceeding 1%) and the reported value of peak load corresponds to the last converged load step. The reported vertical deformation is at the mid-span of the top fiber of the beam and the horizontal deformation is measured at the bottom fiber of the beam at the position of the vertical support as shown in figure 4.1. Both the deformations correspond to the assumption of CUR formulation as can be seen in figure 2.2. A comparison is also made between the membrane force estimated by the analytical and numerical method using the composed line option in DIANA. The total membrane force is calculated by summing up the axial force output of composed line and the additional horizontal force due to maximum moment in the beam. To convert the bending moment to axial force an internal lever arm of 75% of height of concrete member is assumed following the outputs of non-linear analyses.

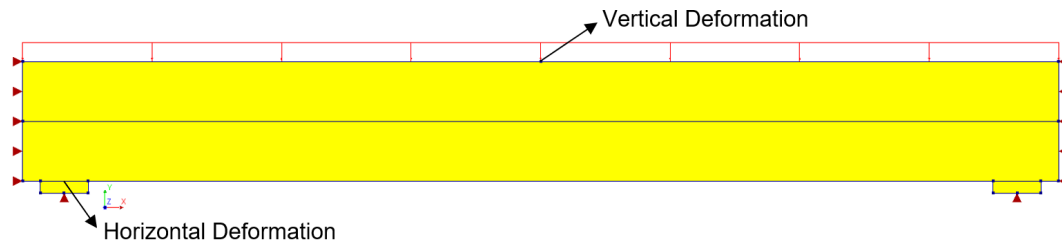


Figure 4.1: Location of vertical and horizontal deformation measurement

The general failure mode and P-Delta behavior of all the 4 variants is first discussed before looking into the results of the sensitivity analysis. All the models discussed here are with the uniformly distributed loads and the structural behavior of the beams with point loads is discussed separately in relevant sections. All the results shown are with absolute deformation and a scale of 5 in DIANA result view settings.

4.1.1. PCC Ideal Model

This model is the closest to the assumptions of the analytical model, hence very similar failure mode and cracking behavior is expected. The results discussed in this section corresponds to the model as described in table 4.1.

Table 4.1: PCC ideal model

Property	Value
Width of the beam	1000mm
Stiffness of end restraint (k_{DIANA})	$25 N/mm^3$
$k_{analytical}$	$12.5 \times 10^6 N/mm$
Total length	8700mm
Height of the beam	1000mm
Compressive model	Ideal Plastic

It can be seen from figure 4.2 that concrete has reached its compressive strength at the edges and as well as at the center of the beam and the height of compressive zone is also rather comparable. This verifies the horizontal equilibrium of the structure, however, as can be seen from sub-figure (a) figure 4.2, the height of compressive zone at the mid-span is a bit smaller compared to height of the compressive zone at the supports possibly due to higher plasticity. This is further reinforced by the principal strain plot (sub-figure (b) of figure 4.2) where it can be seen that the mid-span has higher plasticity than the supports. The arch can also be clearly visualized from the principal stress plot. It is also assumed that half the height of the beam at the edges would be in compression for conversion of linear spring to a discrete spring value, as mentioned before. This assumption also seems logical following the stress plot.

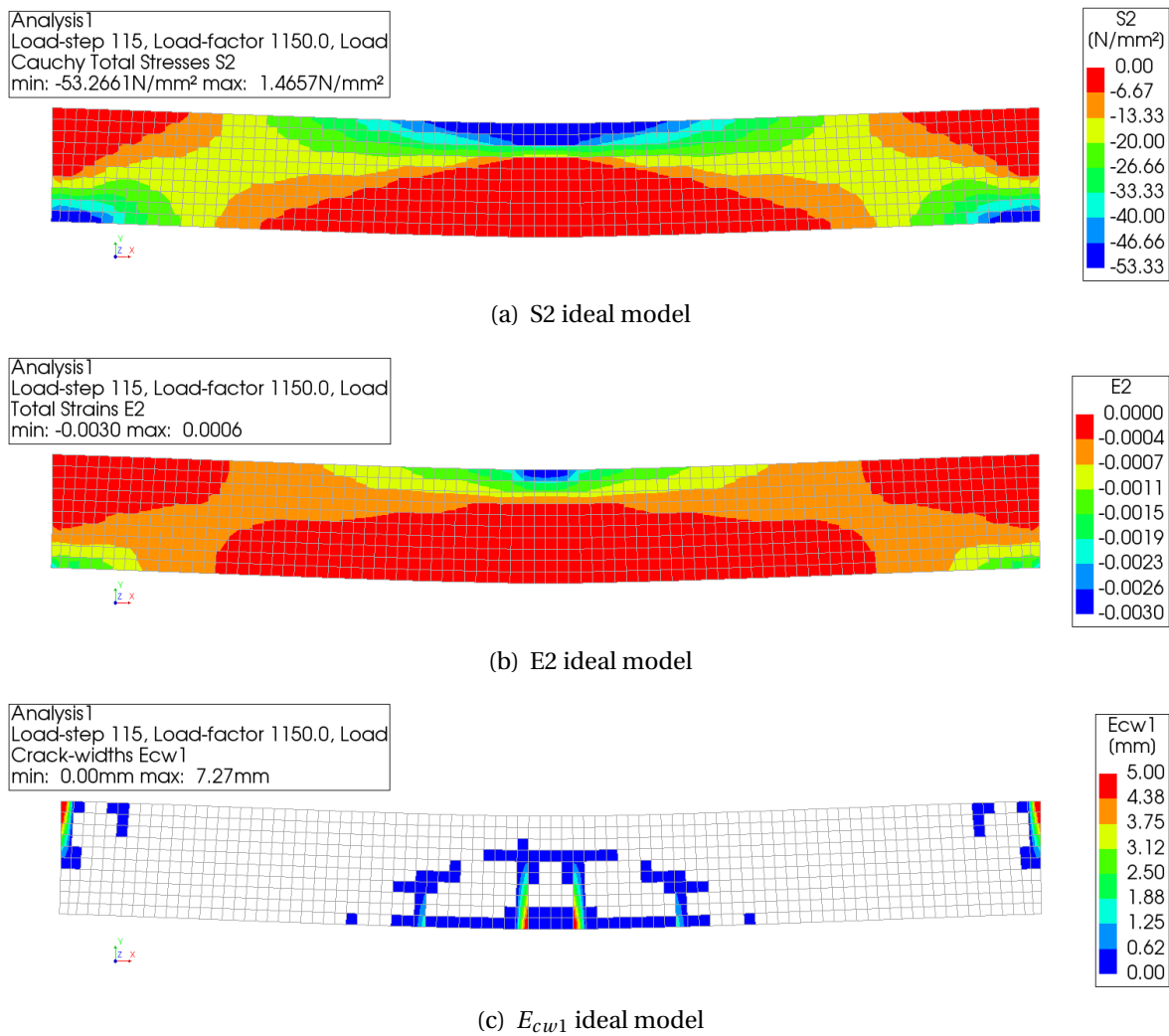


Figure 4.2: General behavior of PCC ideal model

The cracking patterns also fulfill the basic requirement for the generation of arch action i.e. cracking at the edges and at the mid-span so the neutral axis shifts towards the compressive side. However, it must also be noted that there are 4 cracks at the mid-span contrary to the assumption of the analytical model of a single crack. As an idea to have similar crack pattern a discrete crack model was also produced but satisfactory results were not

found due to rapid concentration of stresses at the mid-span. The cracks seem to become horizontal after penetrating a certain depth in to the beam at mid-span, an effect which might be explained by the higher compressive stress at the top acting as prestress and forcing the cracks to change orientation.

4.1.2. PCC Parabolic Model

This model is the same as PCC ideal model except that the compressive behavior of concrete is parabolic. The results discussed in this section corresponds to the model as described in table 4.2.

Table 4.2: PCC parabolic model

Property	Value
Width of the beam	1000mm
Stiffness of end restraint (k_{DIANA})	25 N/mm^3
$k_{analytical}$	$12.5 \times 10^6 \text{ N/mm}$
Total length	8700mm
Height of the beam	1000mm
Compressive model	Parabolic

The results of the PCC ideal model (figure 4.2) and the PCC parabolic model (figure 4.3) are very similar in terms of stress distribution and crack pattern as only the compressive behavior is different. It can be said that even with parabolic compressive behavior, all the made assumptions seem logical and expected results are obtained. Therefore, the parabolic stress-strain model is used for the compression and prestressed models.

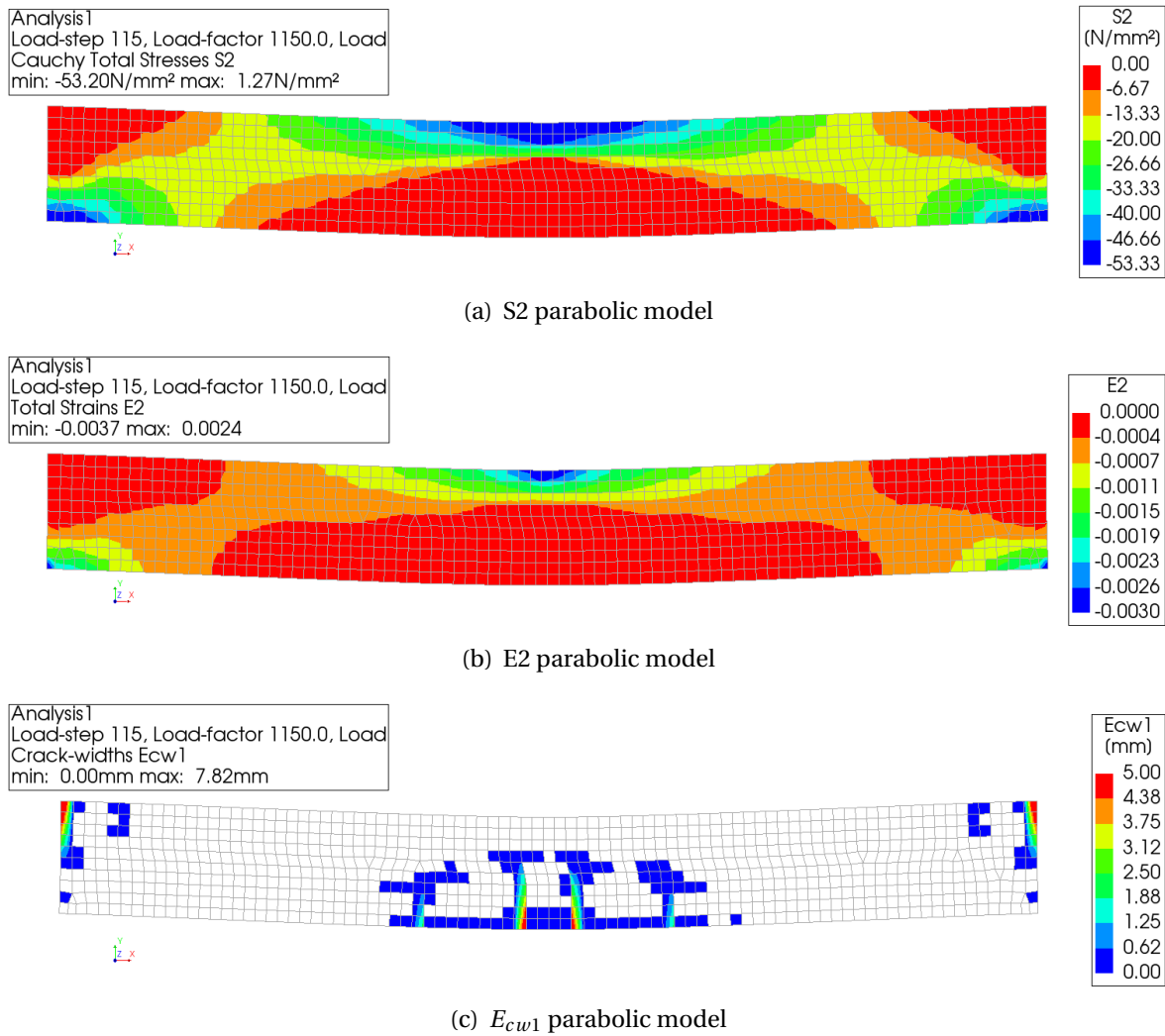


Figure 4.3: General behavior of PCC parabolic model

4.1.3. Compression Model

Compression model allows to study the effect of initial prestressing on the system without the influence of prestressing tendons on the behavior. The results discussed in this section corresponds to the model as described in table 4.3.

Table 4.3: Compression model

Property	Value
Width of the beam	1000mm
Stiffness of end restraint (k_{DIANA})	25 N/mm^3
$k_{analytical}$	$12.5 \times 10^6 \text{ N/mm}$
Total length	8700mm
Height of the beam	1000mm
Compressive model	Parabolic
Initial prestress	4 MPa

The stress plot of the compression model seems comparable with the PCC ideal and parabolic model as expected because in all the cases the ultimate failure of the structure is due to crushing of concrete at sides and at the edges following the arch. The cracking behavior is also similar as the edge cracking and the change in orientation of the crack at mid-span can be seen. However, there is a significant difference in the load deformation response which is discussed later in the chapter.

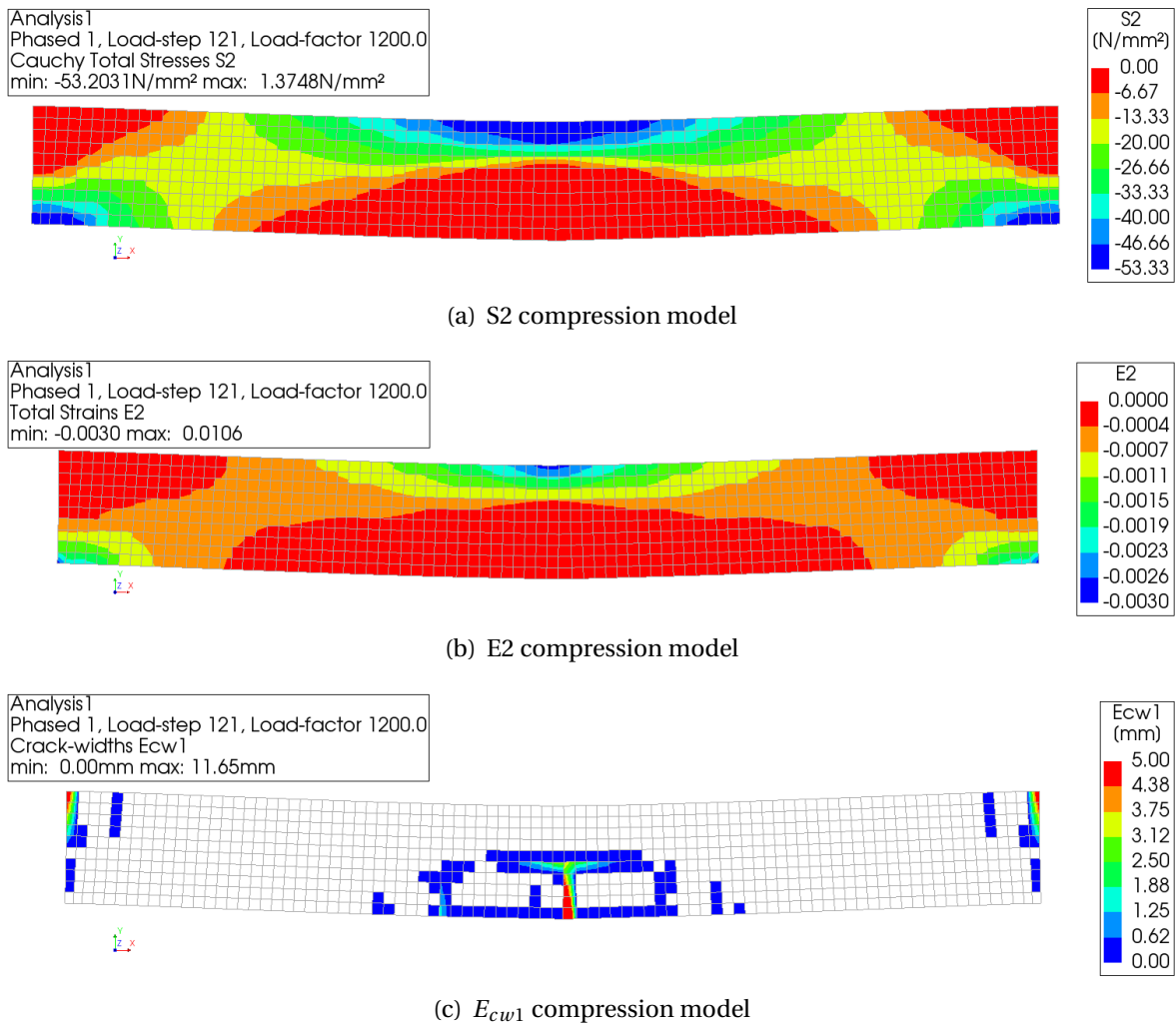


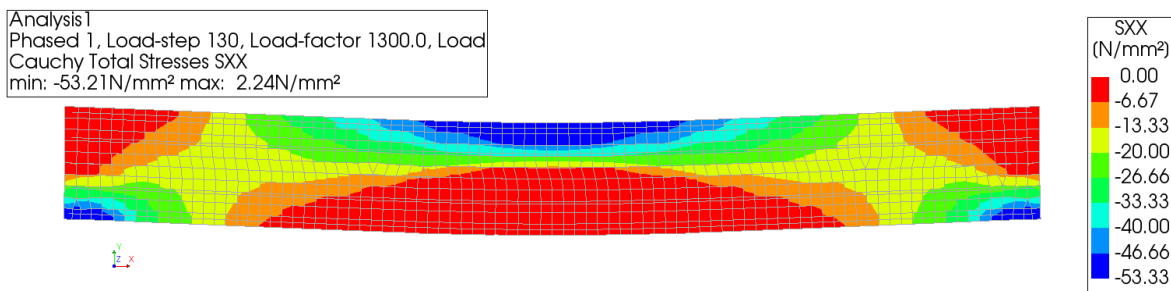
Figure 4.4: General behavior of compression model

4.1.4. Prestressed Model

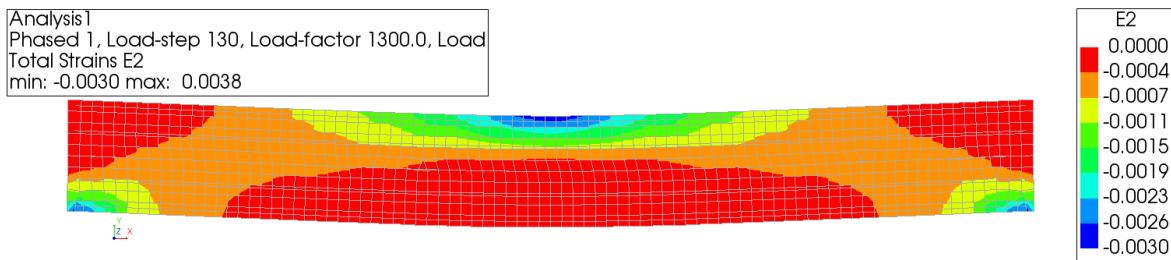
Prestressed model is a more realistic model as the prestressing tendons are also modeled so the effect of their presence can also be studied. The results discussed in this section corresponds to the model as described in table 4.4.

Table 4.4: Prestressed model

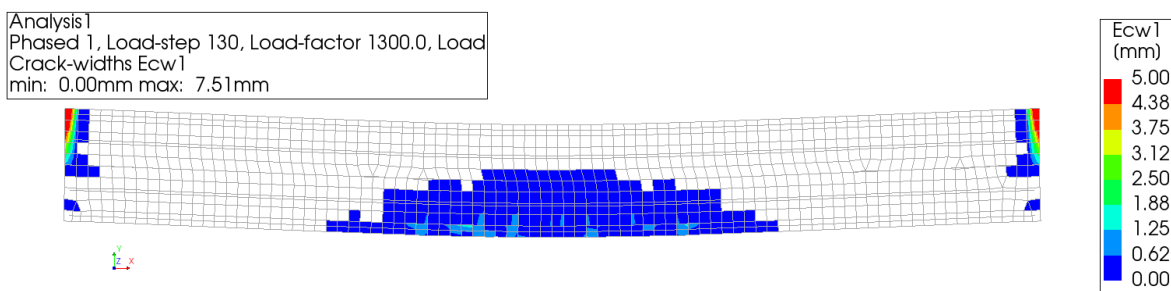
Property	Value
Width of the beam	1000mm
Stiffness of end restraint (k_{DIANA})	25 N/mm^3
$k_{analytical}$	$12.5 \times 10^6 N/mm$
Total length	8700mm
Height of the beam	1000mm
Compressive model	Parabolic
Initial prestress	4 MPa
Area per tendon	924 mm^2



(a) S2 prestressed model



(b) E2 prestressed model



(c) E_{cw1} prestressed model

Figure 4.5: General behavior of prestressed model

The cracking pattern in figure 4.5 is quite different from the one observed for all the other models, possibly because of the presence of the tendons which act as reinforcement using the residual part of the stress-strain curve once the loading is applied. Therefore, more distributed and smaller cracks are observed when compared to other models. How-

ever, the failure mode is still the same i.e. the crushing at mid-span and at the edges so the stress plot is very similar to other models.

4.1.5. Comparison of the Numerical Models

A typical behavior of all the 4 variants is shown in figure 4.6. Comparing the load-deformation response of the models, it can be seen that for PCC ideal and parabolic model, there is hardly any difference. Both crack at around 100 KN/m/m resulting in the plateau of increasing deformation. Beyond that the arch action takes over and allows the member to resist a much higher load. The compression model has a larger linear elastic part i.e. it cracks at a higher load of around 350 KN/m/m because of the initial prestressing which delays the cracking and also allows the model to resist a bit higher load of 1200 KN/m/m. The prestressed model is able to resist even higher load due to the presence of tendons which act as reinforcement and share a part of the load in concrete member.

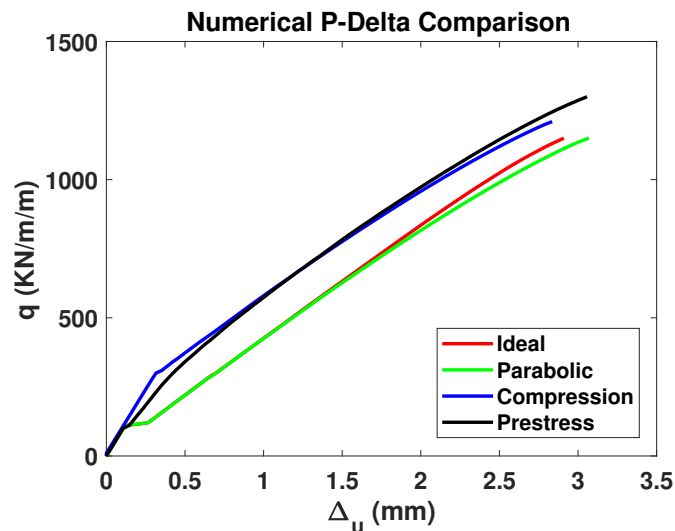


Figure 4.6: Load deformation comparison of the variants

The load-deformation behavior of the numerical model is also compared with the load-deformation behavior predicted by the analytical model in figure 4.7. From the sub-figure (a) of figure 4.7, it can be seen that the behavior of analytical and numerical model is indeed quite comparable, especially in terms of peak load and deformation at peak load, for both ideal and parabolic concrete compression models. In sub-figure (b) two graphs are plotted for the analytical model (i) CUR 0 MPa, which is the analytical model without the consideration of prestressing and (ii) CUR 4 MPa, which includes the initial prestress of 4 MPa as F_0 . From the results it can be seen that inclusion of prestress in CUR model using F_0 might not be suitable as the result of numerical model are quite comparable with the analytical model without the consideration of prestress. This has been further discussed in section 4.5.

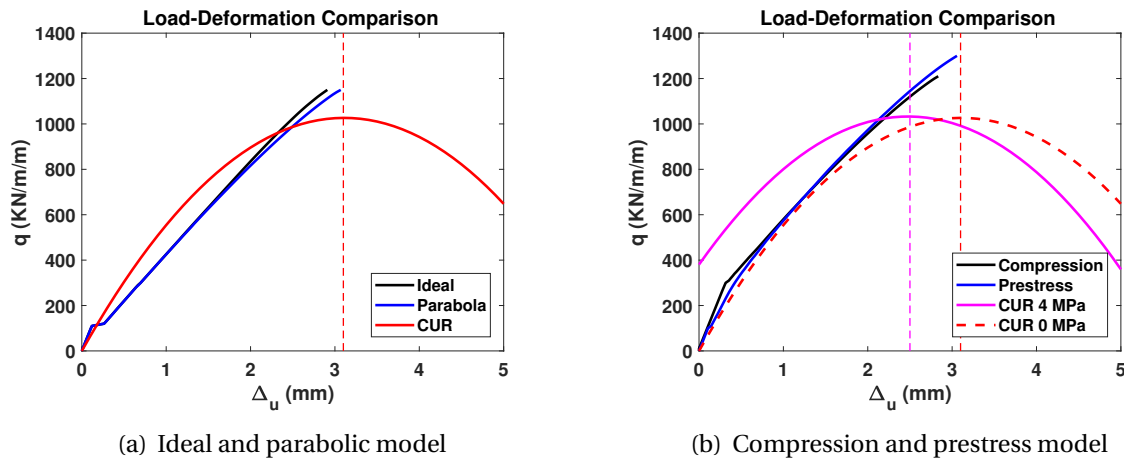


Figure 4.7: Comparison of analytical and numerical load-deformation behavior

4.2. Slenderness Sensitivity Analysis

To study the effect of varying span-to-depth ratio on arch action in concrete beams, the total length of the beam, width of the beam and the end restraint is kept constant in all the models and the height of the beam is varied from 500mm to 1500mm to vary the slenderness. A summary of the model description is presented in table 4.5. Note that a lower prestress of 2MPa is used for the sensitivity analysis of span-to-depth ratio because the normally used value of 4MPa resulted in significant cracking at anchor locations of the tendons when applied on the beam with the height of 1500mm. In all other comparisons, the value of prestress is kept constant at 4MPa.

For comparison in graphs, all the results of the analytical model are referred to as CUR but they correspond to their respective models as described in chapter 2. For slenderness sensitivity analysis, the analytical model used is as per section 2.2 of the report.

Table 4.5: Summary - Slenderness sensitivity analysis

Property	Value
Width of the beam	1000mm
Stiffness of end restraint(k_{DIANA})	$25 N/mm^3$
$k_{analytical}$	$6.25 - 18.75 \times 10^6 N/mm$
Total length	8700mm
Height of the beam	500-1500mm
Compression model prestress	2 MPa
Prestressed model prestress	2 MPa

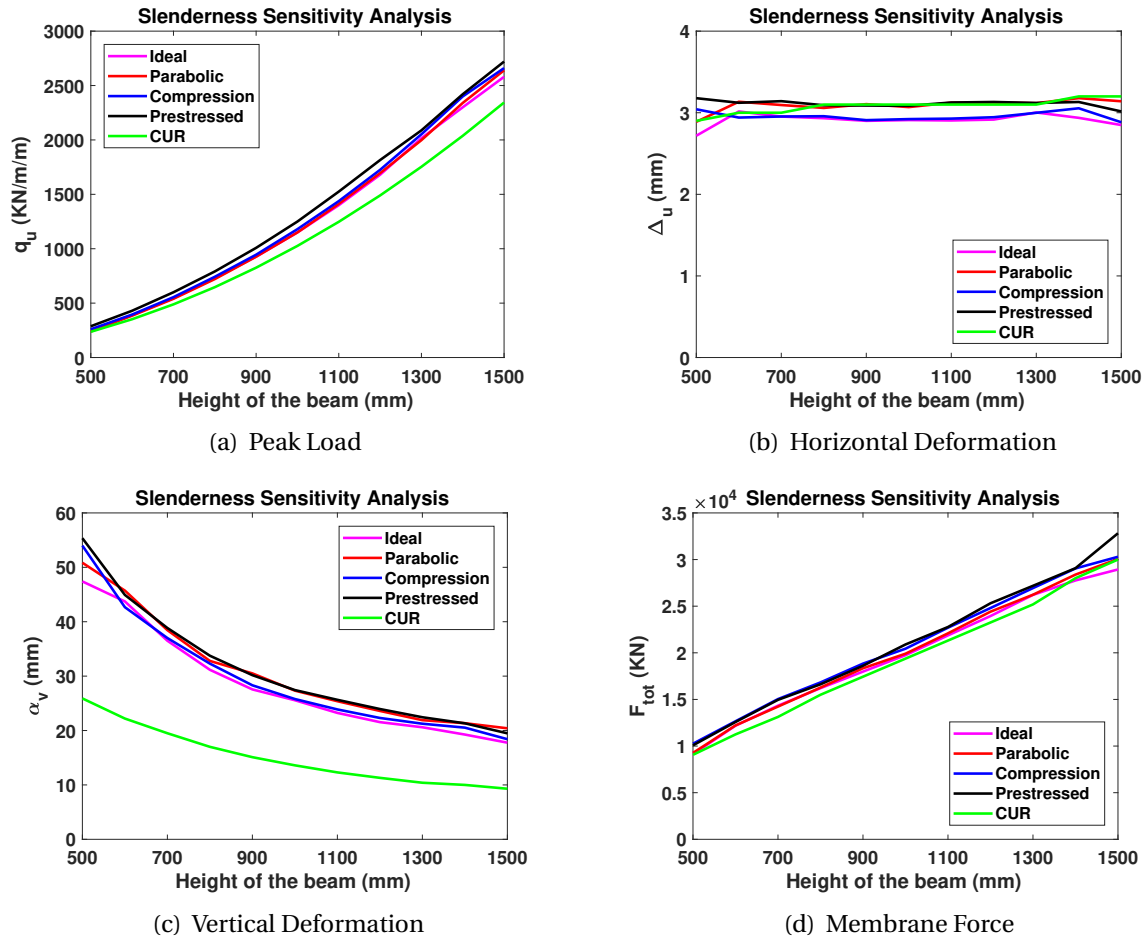


Figure 4.8: Slenderness sensitivity analysis

For sensitivity analysis the peak load, horizontal deformation, vertical deformation and membrane force are compared among all the models as shown in figure 4.8. The values plotted in sub-figures (b)-(d) are at the peak load shown in sub-figure(a). The peak load graph shows that indeed the span-to-depth ratio has a significant effect on the arching capacity of concrete member as also concluded by several authors [12, 15, 17, 19] - given that enough restraint is available. It can also be seen that the CUR method is able to conservatively predict the capacity of all the beams with slenderness ranging from 17.40 to 5.80. When compared to the PCC ideal model, the prediction of arching capacity is within 12% for all the studied slenderness ratios. Furthermore, it can be seen that for the beam with 500mm height (slenderness = 17.40), the difference in analytical and numerical capacity is rather small i.e. 1% when compared to PCC ideal model therefore it is suggested to not make use of this model for beams with $l/h < 15$ - this is also not explicitly mentioned in the CUR recommendations as the underwater concrete floors are assumed to meet this criterion. As also discussed before, the results of PCC ideal and parabolic model are very similar. The inclusion of prestressing (2MPa) slightly increases the capacity of all the models but the effect is not very significant. Similar conclusion has also been made by FarhangVesali [8] for reinforced concrete beams i.e. the reinforcement has only minor effect on the load capacity of structures where the arching capacity is larger than the capacity provided by reinforcement. The sub-figure (b) of figure 4.8 shows that the horizontal deformation predicted by

the analytical and numerical approach is also rather comparable for all the models with a maximum difference of 5% for all the studied slenderness ratios. The peak loads and horizontal stretch of the system are the most important parameters in the study of arch action and the approximate analytical method seems to be able to predict both of them in good comparison with the numerical results.

The vertical deformation however, is rather underestimated by the analytical model as shown in sub-figure (c) of figure 4.8. This difference is possibly because of the simplistic assumptions of the model i.e. the ignorance of axial deformation of the strut due to increasing membrane force and the ignorance of the bending deformation of the member as only the rigid body rotation is taken in to account. For all the studied slenderness ratios, the analytically calculated vertical deformation is almost 50% lower than the numerically obtained results. The vertical deformation of all the numerical models is however rather comparable and shows the same trend so it can be said that the prestressing does not significantly effect the vertical deformation at mid-span. In general, both analytical and numerical model show a decrease in the deformation of the beam with decreasing slenderness due to deep beam effect.

Sub-figure (d) of figure 4.8 shows that the membrane force predicted by the analytical model is also in accordance with the results of numerical analysis with a maximum difference of 10%. The slightly higher value of membrane force in non-linear analysis might be due to the plasticity of concrete which is not considered in the analytical model. Similarly, as for the vertical deformation, all the numerical models have rather comparable membrane force at the ultimate load i.e. prestressing seems to have very minor effect.

The load against horizontal deformation plots of the ideal PCC model for varying span-to-depth ratios is shown in figure 4.9.

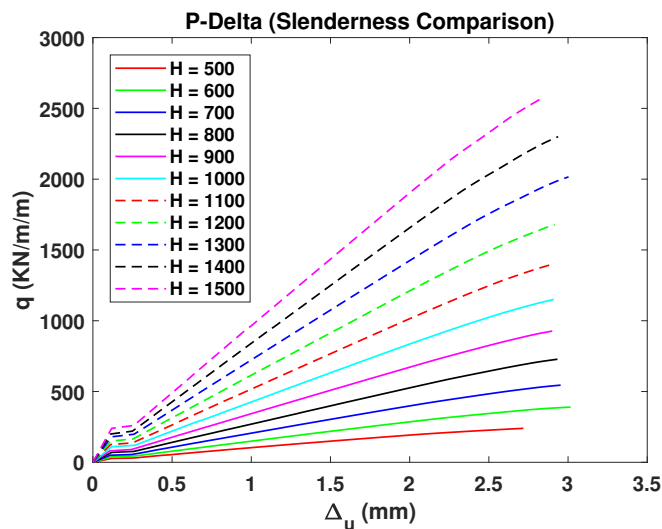


Figure 4.9: Peak load against horizontal deformation for ideal PCC model (Slenderness Sensitivity)

The effects of varying the slenderness can also be visualized in figure 4.9, which shows that not only the ultimate load carrying capacity is enhanced for beams with lower slenderness but also the cracking load increases due to the increased section modulus as expected.

4.3. End Stiffness Sensitivity Analysis

To study the effect of varying end restraint on the arch action in concrete beams the stiffness of restraint is varied from 50 N/mm^3 to a very low value of 2.5 N/mm^3 . All other parameters i.e. the total length of the beam, width of the beam and height of the beam are kept constant. A summary of model description can be seen in table 4.6.

Table 4.6: Summary - End stiffness sensitivity analysis

Property	Value
Width of the beam	1000mm
Stiffness of end restraint (k_{DIANA})	2.5-50 N/mm^3
$k_{analytical}$	$1.25 - 25 \times 10^6 \text{ N/mm}$
Total length	8700mm
Height of the beam	1000mm
Compression model prestress	4 MPa
Prestressed model prestress	4 MPa

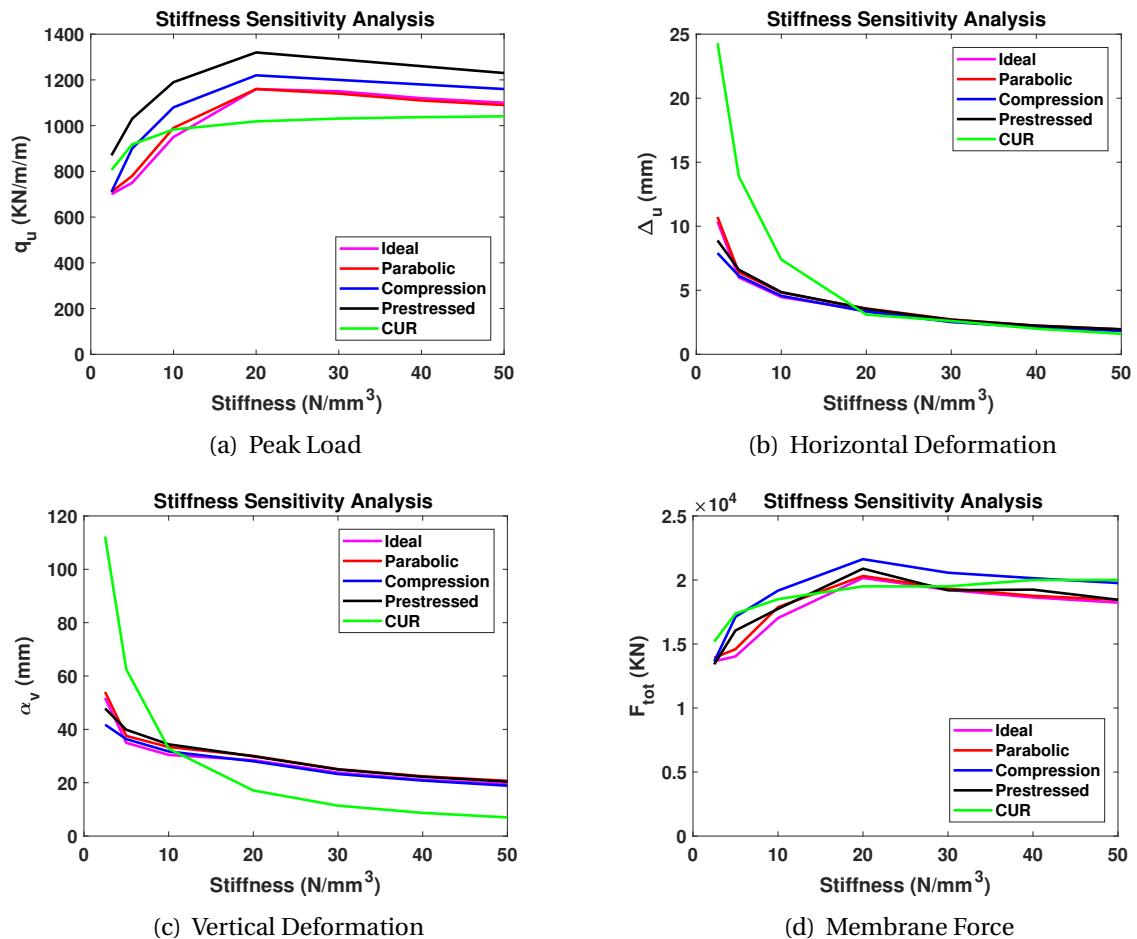


Figure 4.10: End stiffness sensitivity analysis

It must be noted that the end stiffness is a function of beam geometry which, in this

case, is the same for all the models so the effect visualized is purely because of the change in the stiffness of horizontal end restraint. The analytical model used for comparison in this section is as per section 2.2 of the report. As seen from the results in sub-figure (a) of figure 4.10, the stiffness of horizontal restraint only has a significant effect on the arching capacity of the concrete members when the stiffness is rather low, as also concluded by Valipour [18], who made comparison between the stiffness of end restraint and the axial stiffness of the restraint member to develop a minimum criterion for the development of arch action - similar efforts are made to come up with a minimum support stiffness for applicability of the CUR method. Yu [19] has also concluded that the end support stiffness only effects the arching capacity of beams at very low values. When comparing the analytical and numerical results it can be seen that the approximate analytical model is able to conservatively predict the arching capacity of concrete member above a certain horizontal stiffness. This effect is rather pronounced in the sub-figure (b), as the analytical model starts significantly overestimating the horizontal deformations. This is one of the limitations of the analytical model as it allows stretching of the member until the membrane force responsible for the compressive failure of concrete is reached because there is no limitation on the stretching of the system. It is therefore believed that for the application of this analytical model, there must be a minimum criterion for the stiffness of end restraint. This is not explicitly mentioned in the CUR recommendation [2] because for underwater concrete this restraint is always assumed to be available because of the surrounding retaining walls. As an effort to come up with a suitable minimum stiffness, the relation is made with the axial stiffness of concrete member as shown in equation (4.1) and equation (4.2).

$$k_{axial} = \frac{E_c \cdot A_c}{0.5L_x} = \frac{37564 * 1000000}{4350} = 8.63 * 10^6 N/mm \quad (4.1)$$

$$k_{DIANA} = \frac{2 \cdot k_{axial}}{b \cdot h} = \frac{2 * 8.63 * 10^6}{1000000} = 17.27 N/mm^3 \quad (4.2)$$

It is around the stiffness of $17.27 N/mm^3$ where the analytical model start overestimating the horizontal deformations of the concrete member but if the stiffness of the restraint is more than the axial stiffness of the concrete member, the CUR formulation is able to predict the peak load with an accuracy of at least 12% and horizontal deformation with an accuracy of at least 10%. Furthermore, following the results of numerical analysis, there seems to be an optimum value of end restraint stiffness at $20 N/mm^3$. As an extreme value check, the analysis is also performed with fully restrained ends and the numerical peak value dropped to 880 KN/m/m proving that for numerical analysis the optimum end restraint stiffness is also comparable to the member stiffness, possibly because at higher stiffness values the numerical model is less stable due to localization of stresses at the support level. To further verify this conclusion, the analysis is repeated with beams of height 500mm and 1500mm and similar results are obtained. However, the optimum numerical stiffness effects are more visible in members with low slenderness.

Comparing the numerical results, the PCC ideal and parabolic models are very similar but the effect of prestressing with a bit higher prestress (4MPa), is more pronounced - therefore a sensitivity analysis with varying initial prestress is also performed and discussed in section 4.5. The difference in membrane force for compression and prestressed model in sub-figure (d) of figure 4.10 is possibly because of the default composed line option in DIANA, which includes the forces in prestressing tendons and causes the axial force to be

zero just after prestressing in prestressed model, which is not the case in the compression model due to absence of tendons.

Similarly as for horizontal deformation, the vertical deformation is highly over estimated by the analytical model as the stiffness gets rather low, see sub-figure (b) and (c) of figure 4.10. At higher stiffness the vertical deformation is underestimated because the analytical model ignores the axial and bending deformation as discussed earlier. For the end restraint stiffness higher than the axial stiffness of the member, the approximate analytical model predicts the membrane force with an accuracy of at least 10% when compared to the PCC ideal model as seen in sub-figure (d) of figure 4.10.

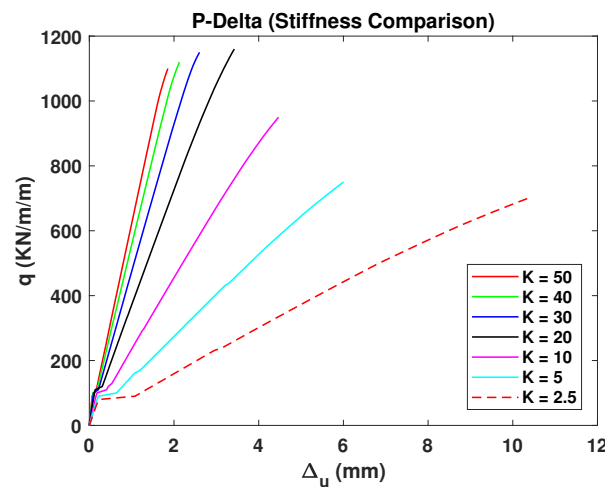


Figure 4.11: Peak load against horizontal deformation for ideal PCC model (Stiffness Sensitivity)

The load-deformation for the PCC ideal model is shown in figure 4.11. It can be seen that the peak load is rather comparable for the models with higher stiffness but as the stiffness becomes rather low, the peak load begins to reduce and deformations become very large. It can also be seen that at lower stiffness the plateau at cracking is bigger because of the lower restraint available at the edges which allows the system to stretch more.

4.4. Beam Width Sensitivity Analysis

The CUR formulation is derived for a slab with a unit width but as this approach is to be applied to a T-Beam, a sensitivity analysis is also performed with varying beam width to verify the applicability of the method on more beam like cross-sections. The summary of the models analyzed for this is given in table 4.7. It must be noted that the stiffness of end restraint is a function of beam geometry so the relative stiffness of the loaded beam and end restraint is the same for all the models.

The analytical model used for comparison in this section is as per section 2.2 of the report.

Table 4.7: Summary - Beam width sensitivity analysis

Property	Value
Width of the beam	200-1000mm
Stiffness of end restraint (k_{DIANA})	25 N/mm^3
$k_{analytical}$	$2.5 - 12.5 \times 10^6 \text{ N/mm}$
Total length	8700mm
Height of the beam	1000mm
Compression model prestress	4 MPa
Prestressed model prestress	4 MPa

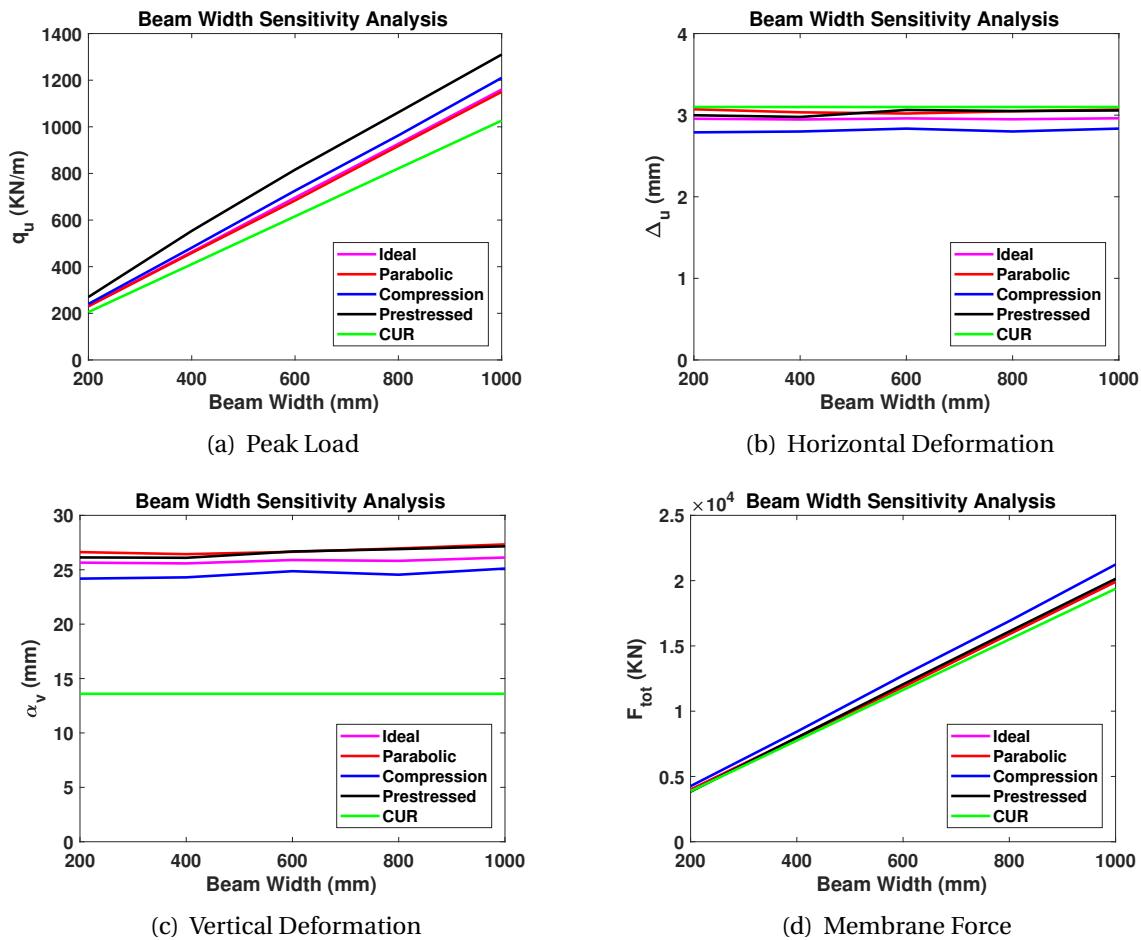


Figure 4.12: Beam width sensitivity analysis

As expected, a linear graph passing through origin is obtained for peak load comparison of all the models (sub-figure (a) of figure 4.12). The difference in the analytically estimated and numerically obtained arching capacity is almost constant around 10% for the studied beam widths. The CUR method also seem to be able to estimate the peak load of beam like members with rectangular cross-sections without any influence of the varying beam width on the accuracy of the model. The prestressing seems to have only minor effect on the load carrying capacity as discussed earlier. The horizontal deformations predicted by

CUR formulation are also very similar to the results of numerical models with an accuracy of around 1.5% for all the beam widths when compared to PCC ideal model.

The vertical deformations are underestimated by the analytical model, as described and explained earlier for the slenderness and stiffness of end restraint sensitivity analysis. The analytical vertical deformations are again around 50% of the deformations obtained as a result of numerical analysis. However, there is a good co-relation between analytical and numerical membrane force in the system with an accuracy of 2.5% for all the beam widths.

The load-deformation behavior of PCC ideal model with varying width of the beam also shows expected results with almost equal increase in ultimate and cracking load with equal increase in the width of the member.

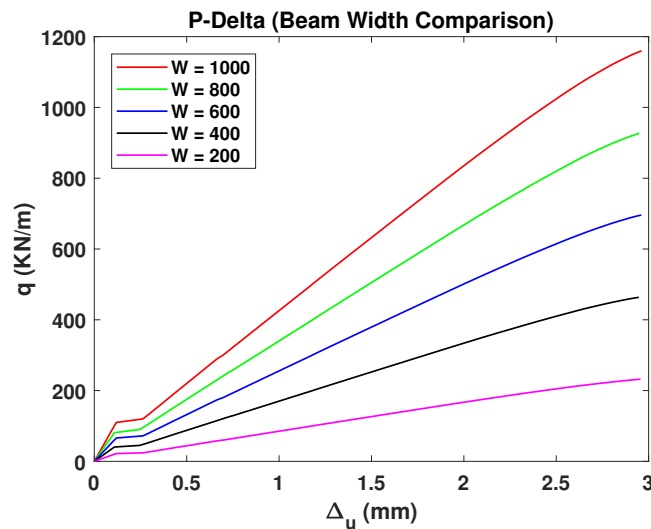


Figure 4.13: Peak load against horizontal deformation for ideal PCC model (Beam width sensitivity)

4.5. Prestressing Sensitivity Analysis

As a side study, the effect of increasing initial prestress is also studied on the structural response of the system. It must be noted that in this comparison the prestressed model is not included and the prestressing is applied only as external load.

The analytical model used for comparison in this section is as per section 2.2 of the report.

Table 4.8: Summary - Prestressing sensitivity analysis

Property	Value
Width of the beam	1000mm
Stiffness of end restraint (k_{DIANA})	25 N/mm ³
$k_{analytical}$	12.5x10 ⁶ N/mm
Total length	8700mm
Height of the beam	1000mm
Compression model prestress	0-10 MPa

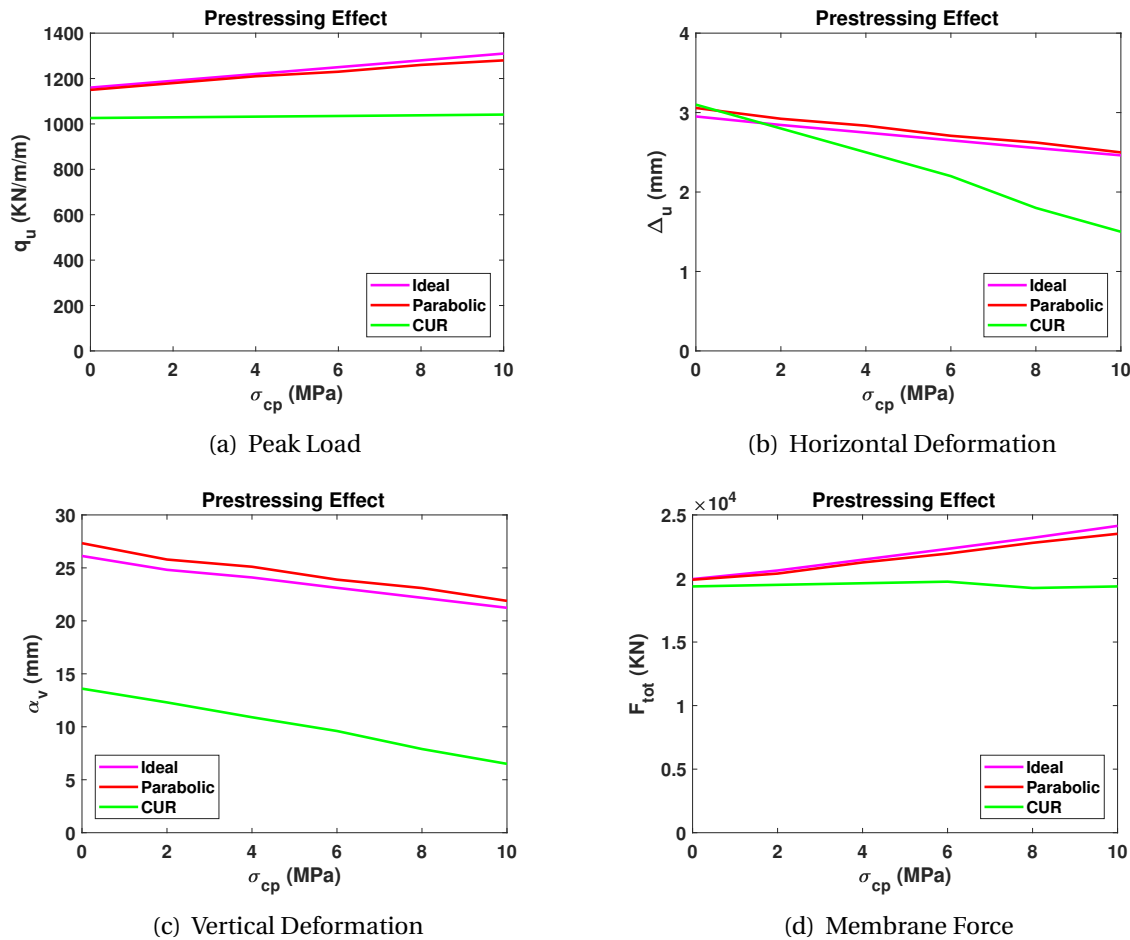


Figure 4.14: Prestressing sensitivity analysis

The sub-figure (a) of figure 4.14 shows that the increase in prestressing only slightly increases the ultimate load carrying capacity of the concrete members due to arch action. Increasing the prestress from 0 to 10MPa increases the peak load carrying capacity by only 11.3%. It can be seen that the CUR method is not able to capture this effect as for all the initial prestressing values the same capacity is predicted by CUR method. At 0 MPa prestress the difference in analytical and numerical capacity is 2.5% which increases almost linearly to 20% at 10 MPa prestress. The horizontal deformation estimated by CUR is also only comparable with no prestress applied (difference of only 1.3%), increasing the prestressing force in the CUR method underestimates the horizontal deformation as seen in sub-figure(b) of figure 4.14. At 10 MPa prestress the difference in analytical and numerical horizontal deformation at peak load is around 40%. This is possibly because the CUR method takes the initial prestress load as F_0 which already compresses the system and the strength of concrete is reached with lesser stretching as shown in figure 4.15 (the graph shifts leftward). Although this is also observed in numerical models but to a much lower extent because the beneficial effects of prestressing are also taken into account while the CUR method ignores any positive effects of prestressing. It can be said that including the prestress load as F_0 might not be a suitable method to include the effect of prestressing in CUR formulation.

The vertical deformation shows similar behavior as described and discussed in previous

sections i.e. vertical deformations are underestimated by 50% at zero prestress and 70% at 10 MPa prestress. The analytical model is not able to capture the effect of prestressing on the membrane force as well, the difference in membrane force with no prestress is only 2.6% when compared to the PCC ideal model which increases to 20% with 10 MPa prestress.

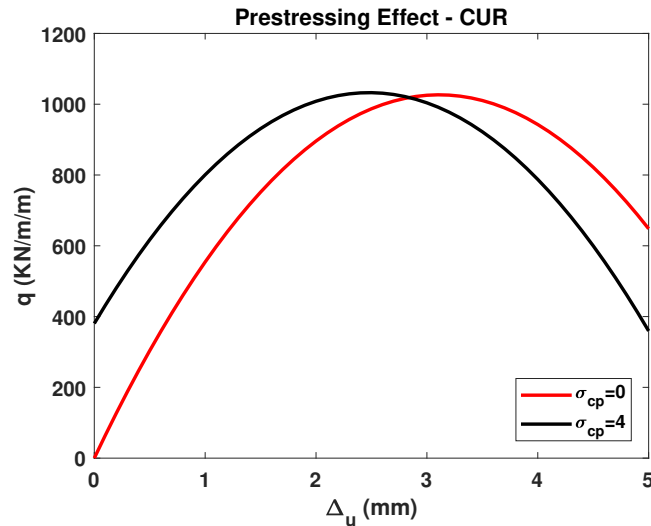


Figure 4.15: Effect of prestressing on CUR formulation

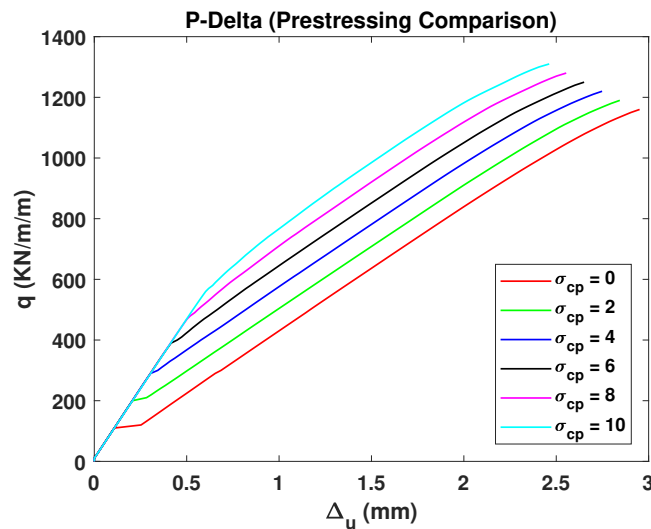


Figure 4.16: Peak load against horizontal deformation for ideal PCC model (Prestressing Sensitivity)

Looking at the load-deformation response of the PCC ideal models with varying initial prestress, it can be seen that the increase in prestress delays the cracking of the member as expected and reduces the maximum deformation at ultimate load as discussed earlier.

4.6. Load Location Sensitivity Analysis

The load location sensitivity analysis is performed to study the effect of point of application of load on the arching capacity of concrete members. It must be noted that the CUR

formulation can only be used for uniformly distributed loads, hence some modifications are made to CUR formulation as described in section 2.3. A summary of the analysis performed to study the effect of location of load on the arching capacity of concrete members is described in table 4.9.

Table 4.9: Summary - Load location sensitivity analysis

Property	Value
Width of the beam	1000mm
Stiffness of end restraint (k_{DIANA})	25 N/mm^3
$k_{analytical}$	$12.5 \times 10^6 \text{ N/mm}$
Total length	8700mm
Height of the beam	1000mm
Compression model prestress	4 MPa
Load location	4000 to 1000mm

From figure 4.18, it can be seen that the compressive stress at the application of point load is higher than at the supports, as assumed in the analytical model. Furthermore, as the loading point gets closer to the support this difference in stress reduces but so does the height of compressive zone and the contribution of the compressive zone in the membrane force (area under stress plot) almost remains the same as described in section 2.3. This concentration of stress might also be explained through the crack pattern comparison, as shown in figure 4.19. Generally, a single main crack seems to develop at the point of application of load which results in a rather rapid concentration of stresses at the top when compared to a beam loaded with uniform load. It is also of interest to note that for most of the models, the failure of the structure is still due to crushing of concrete, which is in line with the assumptions of the analytical model. However, as expected, the farther end of the beam is rather less compressed but the horizontal equilibrium is maintained by a larger height of compressive zone as can be seen in sub-figure (d) of figure 4.18. The comparison of height of compressive zone and maximum stress at support level can be seen in sub-figure(a) of figure 4.17. Sub-figure (b) of figure 4.17 shows that the compressive zone at mid-span is not much effected until there is a direct transfer of load to the supports.

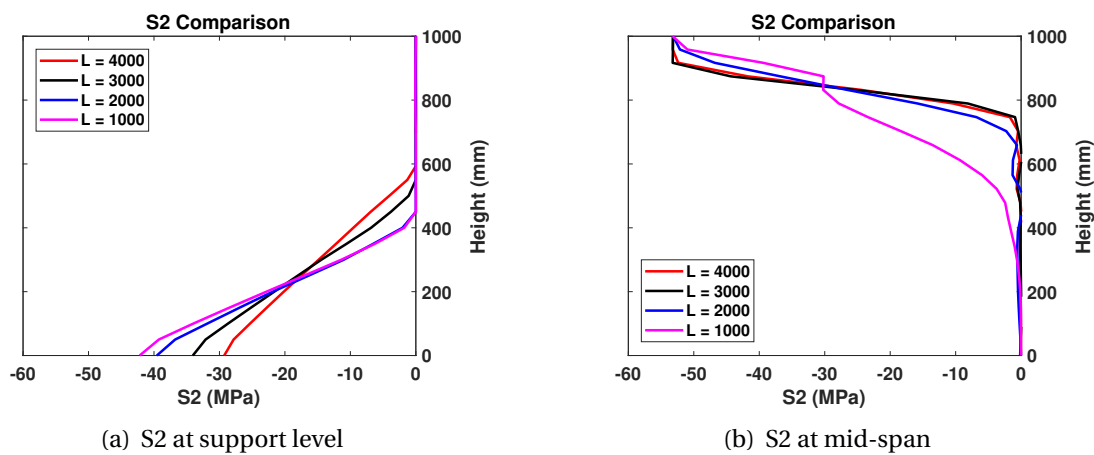
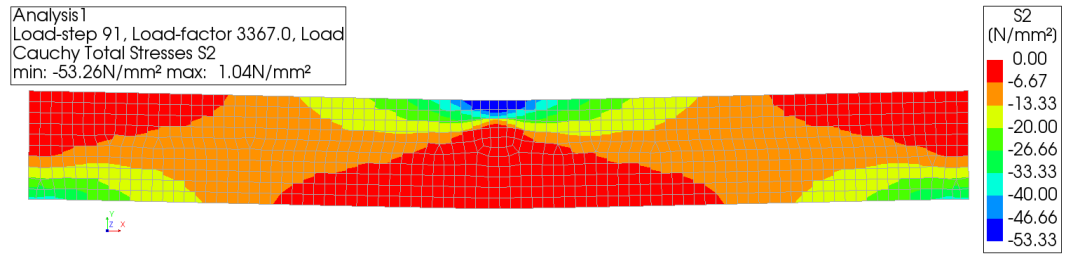
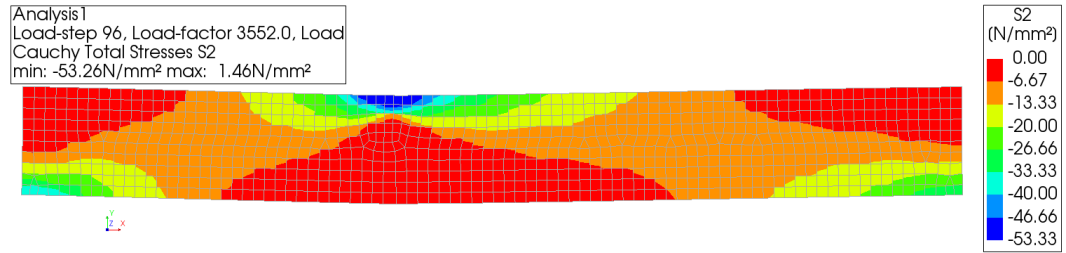


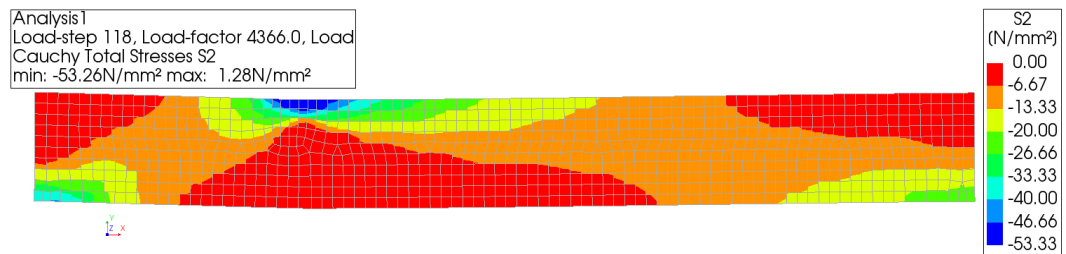
Figure 4.17: S2 and compressive zone height comparison for varying load location



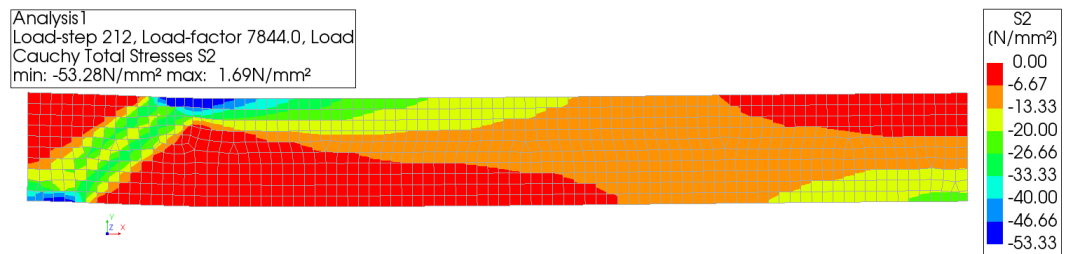
(a) S2 plot for load at 4000mm



(b) S2 plot for load at 3000mm

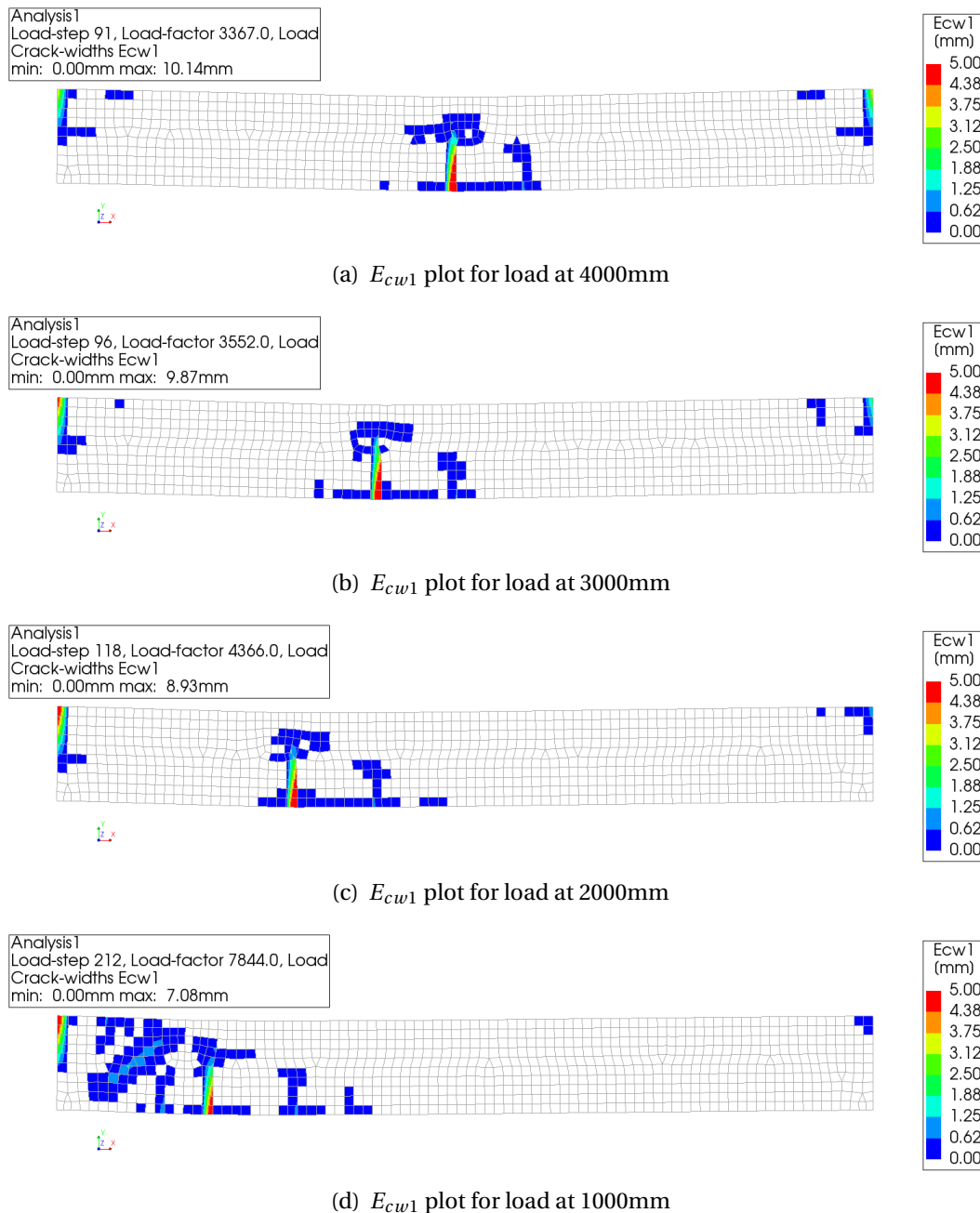


(c) S2 plot for load at 2000mm



(d) S2 plot for load at 1000mm

Figure 4.18: S2 comparison for varying load location

Figure 4.19: E_{cw1} comparison for varying load location

From the results shown in sub-figure (a) of figure 4.20, it can be seen that the numerical arching capacity of restraint concrete members is not significantly effected if the load is in the middle half (from $L/4$ to $3L/4$) of the beam. However, significant increase in the capacity is observed when the load is in the first $L/4$ of the span, possibly because of the direct transfer of load from the loading point to the support. It can also be seen that the modifications made to the CUR model are able to capture the change in numerical capacities if the load is within the central $L/2$ span of the beam with an accuracy of at least 15%. Beyond that the difference rapidly grows to 30% due to direct transfer of load to the supports. The prediction of maximum horizontal deformation is also within 5% for the described range.

The vertical deformation is underestimated as in the previous studies but follows the

same trend as the results of numerical analysis. However, the adapted CUR model is able to predict the membrane force in accordance with the results of numerical analysis. The difference in analytical and numerical membrane force is a maximum of 6.5% for all load locations. This also shows that the membrane force at failure is independent of the load location.

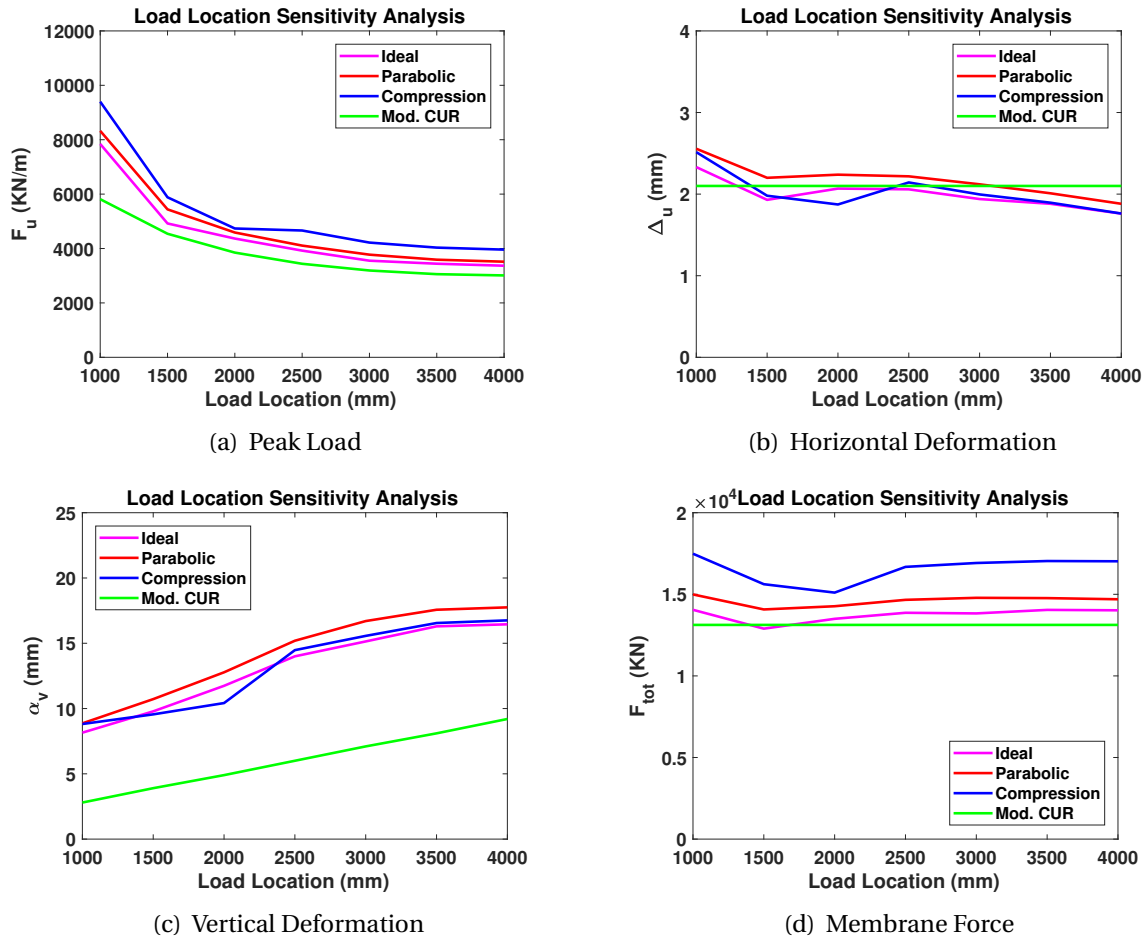


Figure 4.20: Load location sensitivity analysis

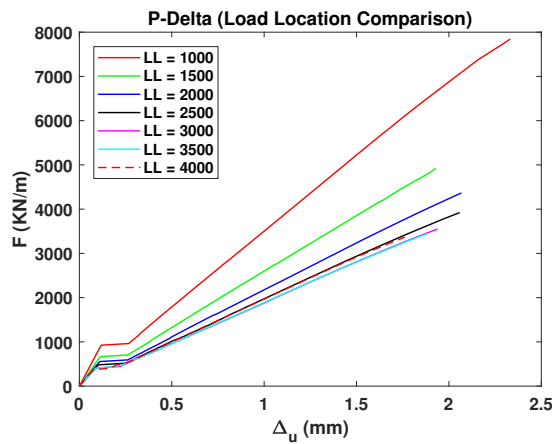


Figure 4.21: Peak load against horizontal deformation for ideal PCC model (Load Location Sensitivity)

Looking at the individual load-deformation behavior, the same conclusion can be drawn that for the load in the central half of the beam, the arching capacity and behavior of the beam is not significantly effected. However, for the load in the first $L/4$ of the span significant increase in the capacity is observed due to the direct transfer of load to the supports.

4.7. Web-width Sensitivity Analysis (T-beams with UDL)

As the main objective is to apply the analytical model on the Vechtbrug beam to determine its arching capacity, efforts were made to study the applicability of the modified CUR method on beams with T-shaped cross-section. The details of modifications made to the analytical method for this comparison are as mentioned in section 2.4. Most of the cross-sectional dimensions of the T-beam are kept similar to the Vechtbrug beam but a relatively simple shape is used to understand the working mechanism. A typical cross-section used for this analysis and its comparison with the Vechtbrug beam is shown in figure 4.22.

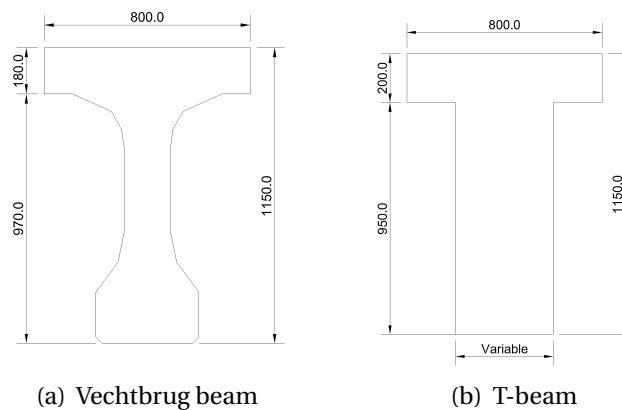


Figure 4.22: T-beam cross-section for sensitivity analysis

The width of the web is varied from 200mm to 600mm as shown in table 4.10 and only the PCC parabolic model is used. It must also be noted that for this sensitivity analysis, the stiffness of end restraint is not a function of beam geometry because of the T-shaped cross-section and the stiffness is a constant value of 25000 N/mm^2 . The load is applied as a uniformly distributed load on the top fiber of the beam.

Table 4.10: Summary - Web width sensitivity analysis

Property	Value
Width of top flange	800mm
Width of the web	200 - 600mm
Height of top flange	200mm
Height of the web	950mm
Stiffness of end restraint (k_{DIANA})	25000 N/mm^2
$k_{analytical}$	$14.375 \times 10^6 \text{ N/mm}$
Total length	8700mm
Total height of the beam	1150mm

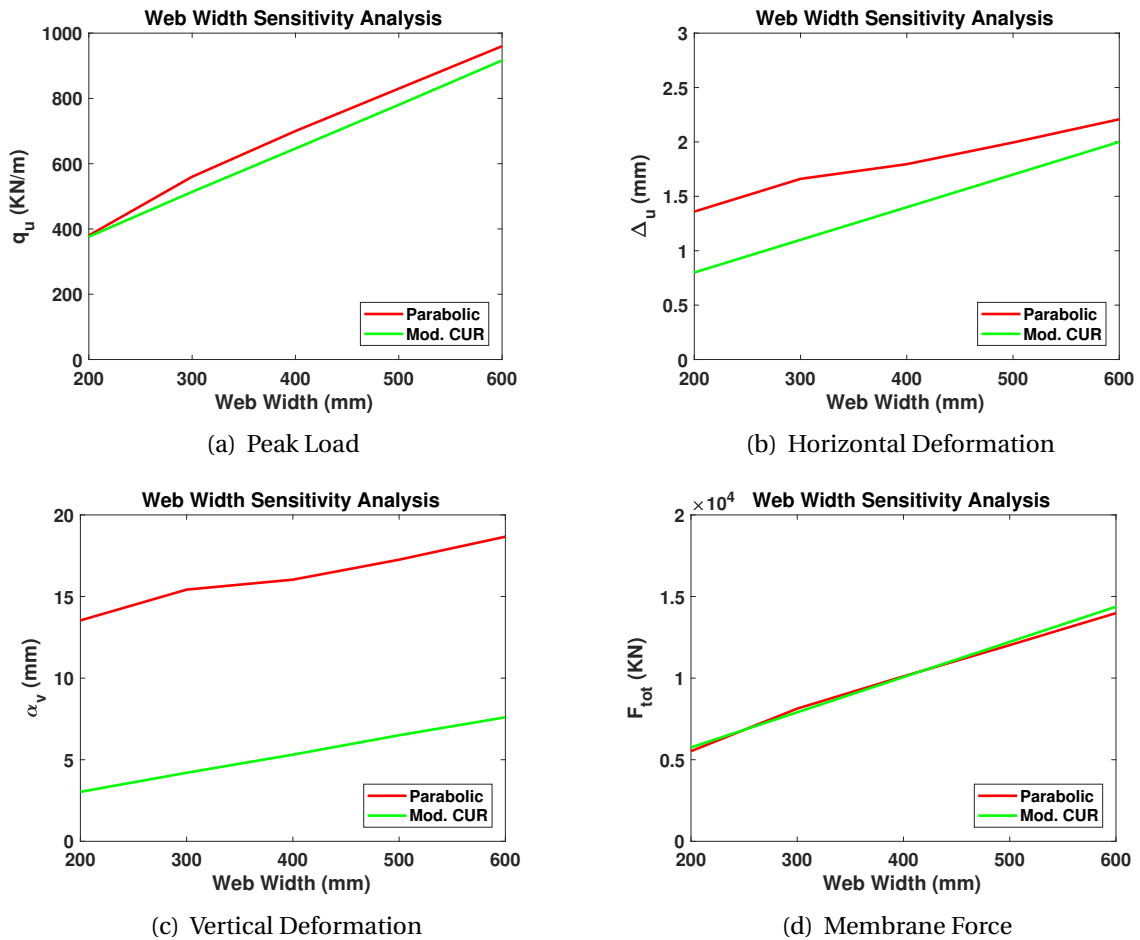
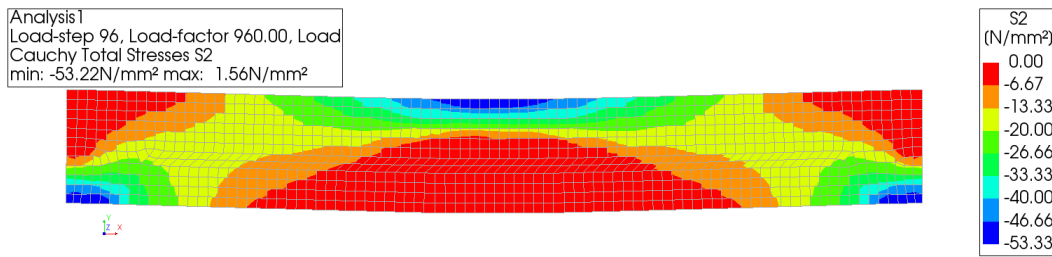


Figure 4.23: Web width sensitivity analysis for T-beam with UDL

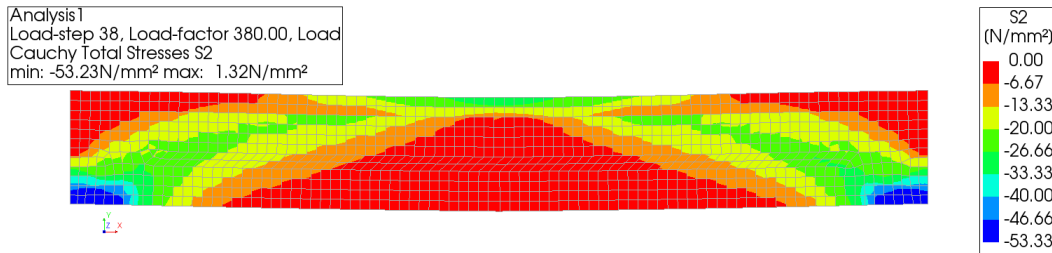
Table 4.11: Summary - Web width effect in numerical models

Web Thickness (mm)	Failure Mode
600	Web Crushing
500	Web Crushing
400	Web Crushing
300	Web Crushing + Strut Failure
200	Web Crushing + Strut Failure

From sub-figure (a) of figure 4.23, it can be seen that after modifications the CUR method is able to predict the capacity of beams with T-shaped cross-sections even when the strut failure due to thin web is observed, possibly because even in the models with strut failure, the final numerical failure of the model is because of crushing of concrete. The difference in analytical and numerical capacity is found to be a maximum of 8%. The horizontal deformation at failure is however a bit underestimated by the modified analytical approach as the accuracy is within 20% for the compression failure i.e. $b_w > 400\text{mm}$. The stress and cracking plots of the beam with a web thickness of 600mm and 200mm are compared in figure 4.24 and figure 4.25.

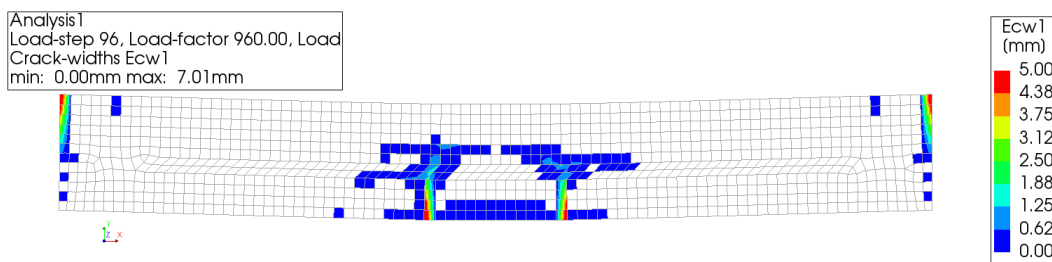


(a) S2 plot for web width of 600mm

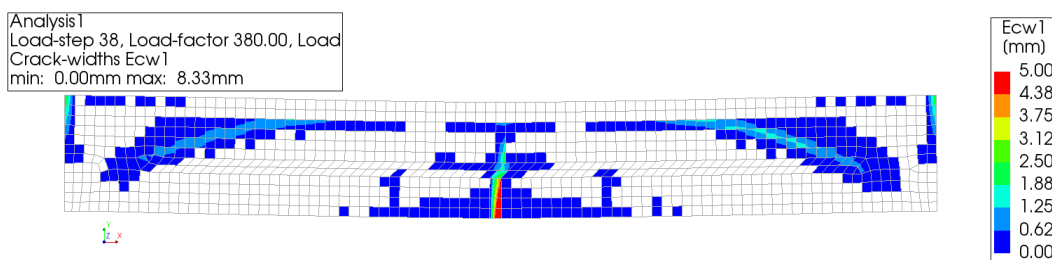


(b) S2 plot for web width of 200mm

Figure 4.24: S2 comparison for varying web width



(a) E_{cw1} plot for web width of 600mm



(b) E_{cw1} plot for web width of 200mm

Figure 4.25: E_{cw1} comparison for varying web width

It can be seen that both the beams have quite different failure modes as the beam with a web width of 600mm fails in compression (in line with the assumption of the analytical model) but the beam with the web width of 200mm also shows a strut failure following the arch. The summary of the results is also presented in table 4.11 and it can be concluded that the modified CUR method is able to predict the capacity of T-beams if the ultimate failure is due to crushing of concrete, hence it should only be applied for beams where a compression failure is expected, as it is one of the basic assumptions of the model and all

other failure mechanisms are not taken into account. Furthermore, as can be seen from sub-figure (b) of figure 4.24, the stress distribution at mid-span is quite different from the one assumed in the analytical model.

The vertical deformations show similar trends as discussed in previous sections. However, the membrane forces predicted by the modified CUR formulation are comparable to the numerical results with an accuracy of at least 5% for all the studied web-widths.

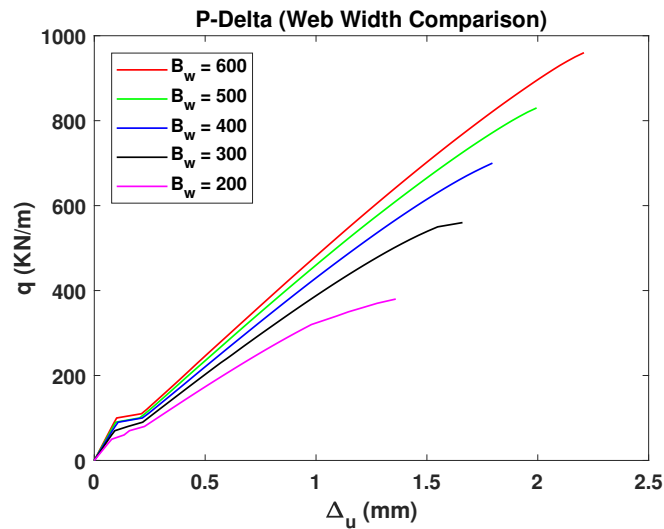


Figure 4.26: Peak load against horizontal deformation for parabolic PCC model (Web width sensitivity)

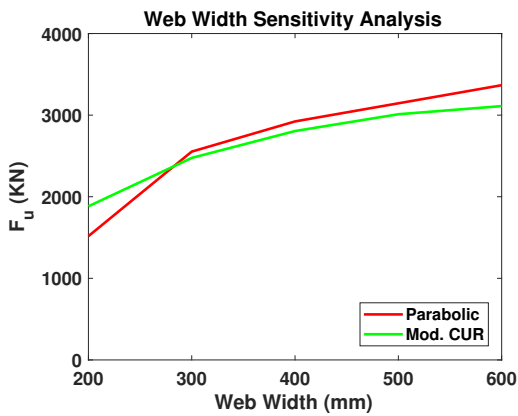
The load-deformation graph of individual analysis can be seen in figure 4.26. An expected trend of increasing peak load and horizontal deformation is observed as the web width increases because of the availability of more material which contributes to a higher membrane force and higher capacity.

4.8. Web-width Sensitivity Analysis (T-beams with Point Load)

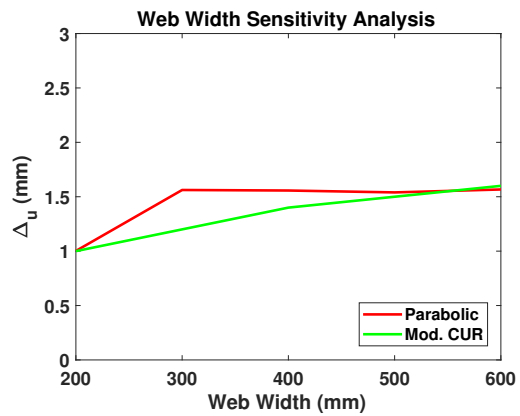
Numerical models are also developed to verify the modified analytical model described in section 2.5 of the report which takes into account both, the differences in the web width and width of the flange and the variation in shear span. The summary of the preformed analysis can be seen in table 4.12.

Table 4.12: Summary - Web width and load location sensitivity analysis

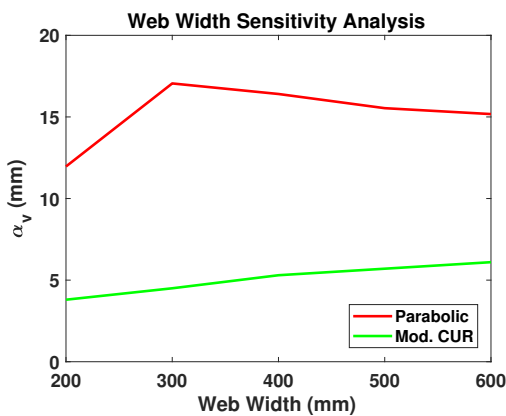
Property	Value
Width of top flange	800mm
Width of the web	200 - 600mm
Height of top flange	200mm
Height of the web	950mm
Stiffness of end restraint (k_{DIANA})	25000 N/mm^2
$k_{analytical}$	$14.375 \times 10^6 N/mm$
Total length	8700mm
Total height of the beam	1150mm
Load location	4000 and 2250mm



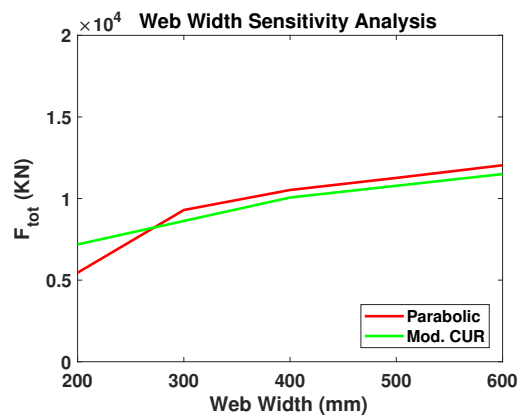
(a) Peak Load



(b) Horizontal Deformation

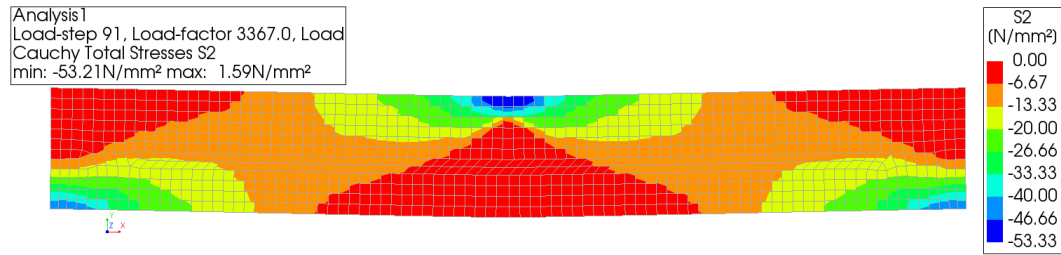


(c) Vertical Deformation

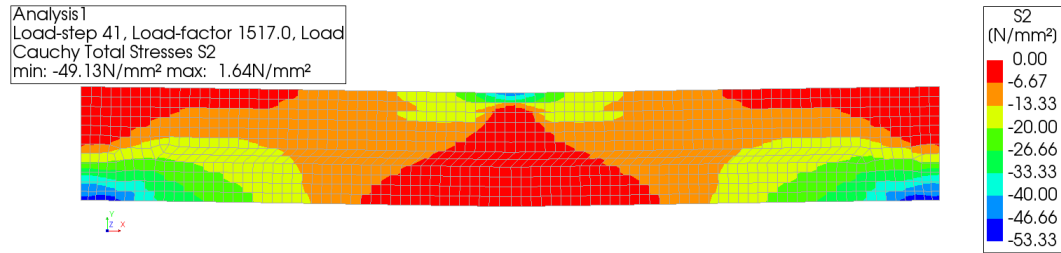


(d) Membrane Force

Figure 4.27: Web width sensitivity analysis for T-beam with point load at 4000mm

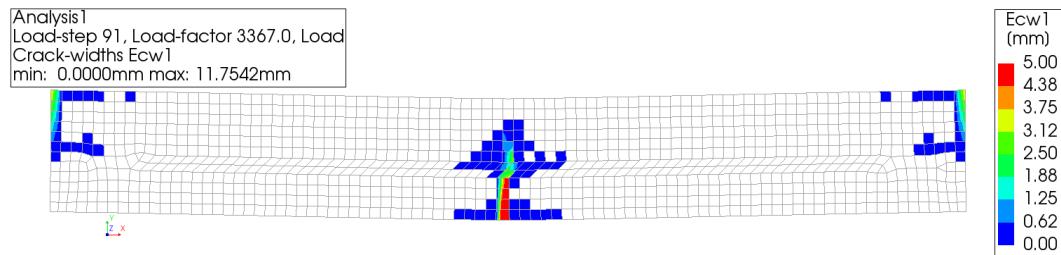
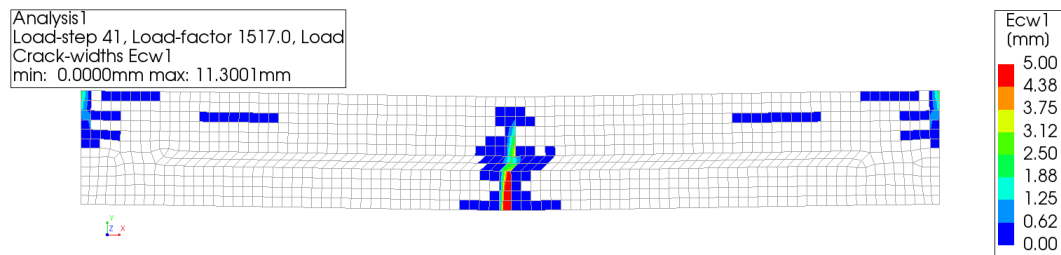


(a) S2 plot for web width of 600mm



(b) S2 plot for web width of 200mm

Figure 4.28: S2 comparison for varying web width with load at 4000mm

(a) E_{cw1} plot for web width of 600mm(b) E_{cw1} plot for web width of 200mmFigure 4.29: E_{cw1} comparison for varying web width with load at 4000mm

From sub-figures (a) of figure 4.27, it can be seen that the modified CUR approach is able to conservatively predict the load carrying capacity of T-beams loaded with point load at mid-span for web widths greater than 300mm within an accuracy of 7.5%. The horizontal deformation predicted by the analytical approach shows a constant reduction as the web width is reduced whereas the numerical model shows little variation but the values are within 10% for web-widths greater than 300mm i.e. crushing failure of concrete. As seen before, vertical deformations are highly underestimated (60%) and the membrane forces are within 5% of the numerical results for $b_w > 300$ mm.

Comparing the sub-figures (a) and (b) of figure 4.28, it can be seen that for web width of 600mm the concrete at mid-span has reached plasticity but not at supports while for web width of 200mm the stress distribution is quite different due to strut failure. Furthermore, in sub-figure (b) of figure 4.29, the start of the shear crack is visible which results in the numerical instability of the analysis, hence the capacity predicted by the modified analytical model in sub-figure (a) of figure 4.27 is higher than the numerical capacity. It can be concluded that the analytical model is able to predict the arching behavior of T-beams loaded with point load if the failure of concrete is in compression at supports or at point of application of load.

Similarly, as for the load at 4000mm the comparison has been made for the point load at 2250mm from the supports for varying web widths and the results are shown in figure 4.30. This has been done to also study if the modified analytical model is able to predict the arching behavior of the T-shaped cross-section loaded asymmetrically.

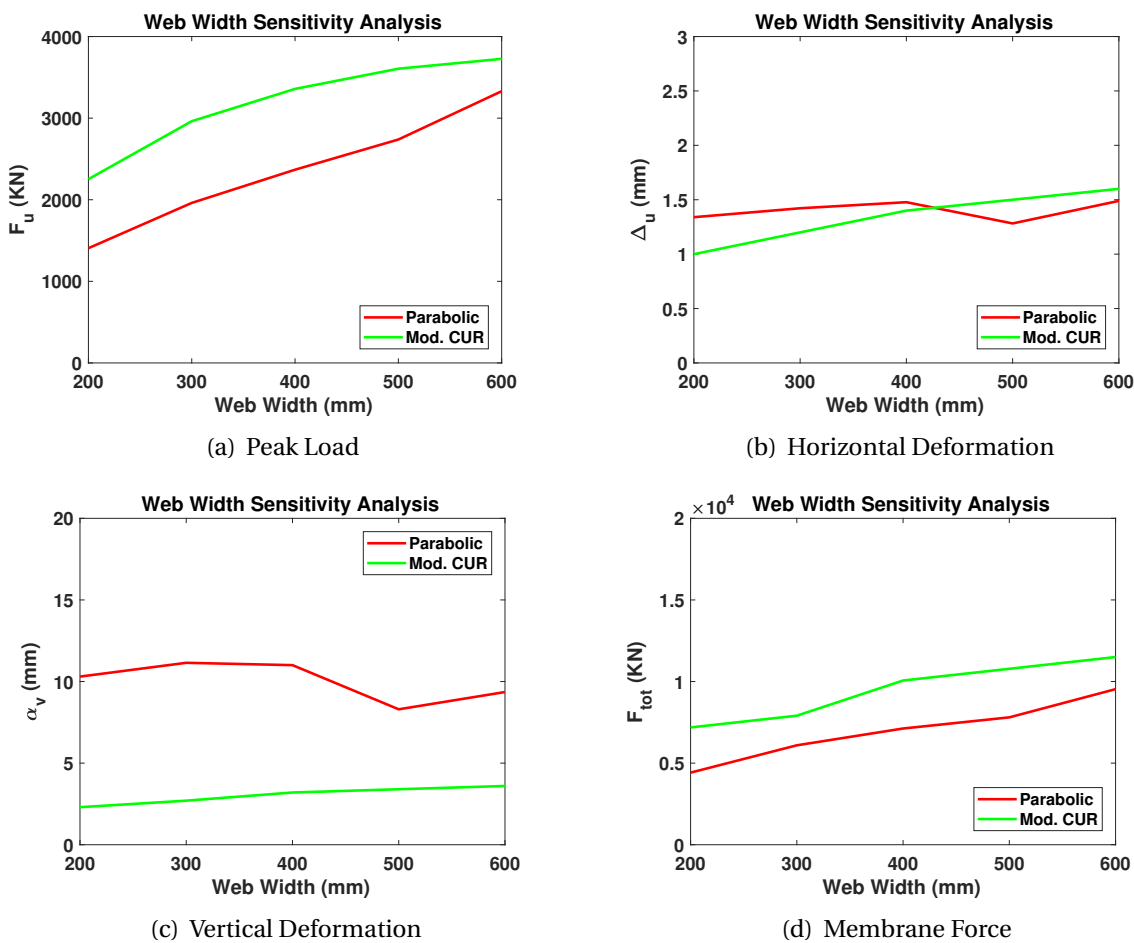


Figure 4.30: Web width sensitivity analysis for T-beam with point load at 2250mm

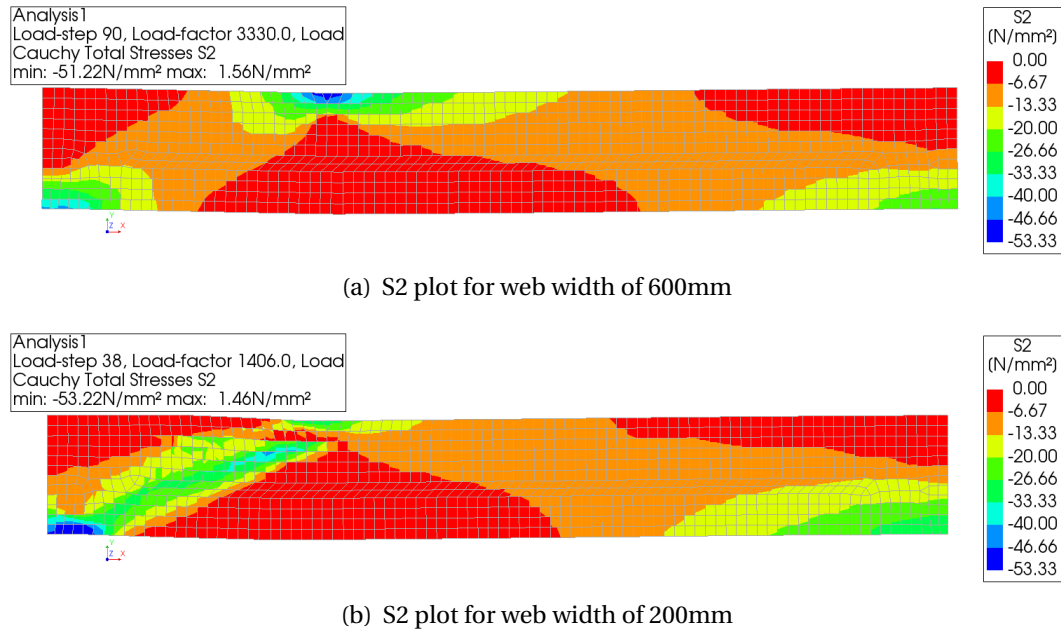
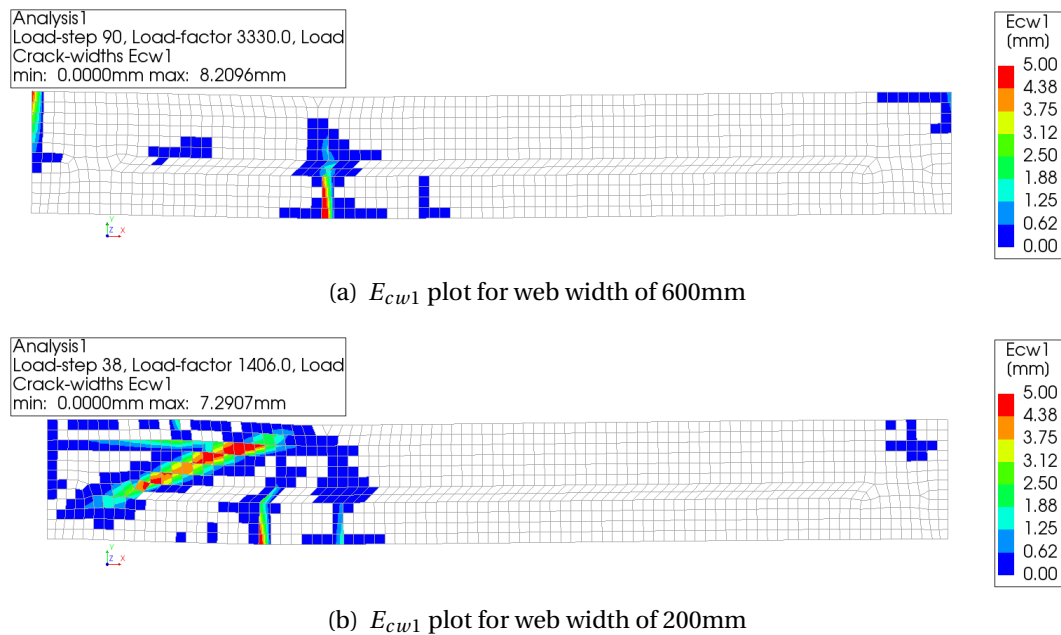


Figure 4.31: S2 comparison for varying web width with load at 2250mm

Figure 4.32: E_{cw1} comparison for varying web width with load at 2250mm

As seen from figure 4.30, the modified analytical model overestimates the capacity of T-beam for all the web widths, possibly because for all the analyses the numerical failure is because of the strut failure and not plasticity of concrete. However, the over prediction increases as the web-width reduces because strut failure becomes more dominant for the structure. The comparison of the horizontal deformation, vertical deformation and membrane force is also shown in figure 4.30.

The stress distribution in sub-figure (b) of figure 4.31 is not in line with the assumption of analytical model and the failure mechanism can also be seen in sub-figure(b) of

figure 4.32. Similar failure is observed with the web width of 600mm. This reinforces the previous conclusion that the modified analytical model is only able to predict the arching capacity of T-beams for which the compression failure of concrete is expected at mid-span or at supports as it is one of the basic assumptions of the model and any other failure mode is not taken into account.

Conclusions (Part-I)

1. The numerical arching capacity of concrete members highly depends on the slenderness ratio and stiffness of end restraint (below a certain value) whereas central prestressing, with or without the tendons, has very limited effect on the ultimate load carrying capacity. However, the crack pattern of concrete members with tendons is quite distributed when compared to un-reinforced members due to presence of tendons.
2. CUR method as described in CUR-077 [2] underestimates the vertical deformations by almost 50-60% when compared with the results of numerical models, possibly because it ignores the axial shortening of the strut and bending deformations of the beam.
3. The analytical model suggested in CUR-077 [2] is able to predict the arching capacity of concrete members in terms of peak load carrying capacity with an accuracy of at least 12%, horizontal stretch with an accuracy of at least 5% and membrane force in the system with an accuracy of at least 10% when compared to PCC ideal model for all the studied slenderness ratios. It is also concluded that the approximate analytical model suggested in CUR-077 should be used only when the slenderness (l/h) of the concrete member is less than 15. This is not explicitly mentioned in CUR recommendations as this criterion is always assumed to be not governing for underwater concrete floors.
4. To analytically determine the arching capacity of concrete members using CUR method, there should be a minimum end restraint stiffness equal to the axial stiffness of the restrained concrete member. This is not explicitly mentioned in the CUR recommendation as sufficient deformation capacity and restraint is always assumed to be available. When this criterion is fulfilled, the CUR method is able to predict the arching capacity with an accuracy of 12%, horizontal stretch with an accuracy of 10% and membrane force with an accuracy of 10% when compared to the PCC ideal model.
5. The CUR formulation is recommended for slabs with a unit width but it can be used to predict the capacity of rectangular cross-sections with varying width without any effect on the accuracy of the model. The predicted peak load, horizontal deformation and membrane force have a difference of 10%, 1.5% and 2% respectively, when compared to the results of numerical models.
6. Prestressing seems to have only minor effect on the arching capacity of concrete beams. Increasing the initial prestress from 0 MPa to 10 MPa results in an increase of only 11.3% in the arching capacity. It has also been concluded that the inclusion of prestress in the analytical model using F_0 , as described in chapter 2, might not be a suitable method. The error in the prediction of horizontal deformation and membrane force increases from 1.5% to 40% and 3% to 20% respectively, when the prestress is increased from 0 MPa to 10 MPa.

7. The adapted CUR model for point load gives comparable peak loads with the numerical models, especially when the load is applied in the central $L/2$ of the beam span. Beyond this region the direct transfer of load occurs between the loading point and the supports and this is not captured by the analytical model. For the load in the central $L/2$ of the span the maximum error in peak load, horizontal deformation and membrane force is 15%, 5% and 5% respectively.

8. The adapted CUR model for T-beams with uniformly distributed load (UDL) is able to conservatively predict the load carrying capacity of concrete members with an accuracy of 7.5% if the failure of the numerical model is due to crushing of concrete. For T-beams with rather thin web, strut failure is also observed which is not taken into account by the assumptions of the analytical model. Therefore, it is concluded that the adapted analytical model should only be used if the crushing failure of concrete is expected.

9. The adapted CUR model for T-beams with point load is also able to predict the arching capacity with an accuracy of 7.5% if the failure of the member is due to crushing of concrete. In T-beams with thin webs the strut failure is also observed and the analytical model developed in this study should not be used as it does not take into account this mode of failure and overestimates the arching capacity.

Part-II Assessment of Vechtbrug Beam

This part of the report focuses on the numerical modeling of the Vechtbrug beam for a simply supported case, as tested on-site, and as part of the bridge deck system, ignoring the distribution of load in transverse direction. The results of the numerical 2D, 2.5D and 3D models are compared with the experimental data and efforts are made to model the behavior of the beam as part of the bridge system by modeling only the loaded sub-span.

5

Vechtbrug - Layout and Details

This chapter describes the layout and details of the Vechtbrug. The experimental set-up for the experiments performed by Ensink as part of his PhD are also discussed so a comparison can be drawn with the numerical models - discussed in the next chapter.

5.1. Location and Layout of Vechtbrug

Vechtbrug was a part of the former Dutch highway A1, see figure 5.1, starting from Amsterdam to the German border in the east of the Netherlands. As a part of project SAAOne, some parts of the highway were renovated and re-positioned. Owing to this, the Vechtbrug was no longer in use and had to be demolished. This gave a unique opportunity to test the full scale bridge on-site and use the experimental data for understanding of the mechanisms working in the bridge system.



Figure 5.1: Location of the Vechtbrug [13]

A partial layout view of the Vechtbrug is shown in figure 5.2 with marked test locations. The materials investigation section in figure 5.2 is used to determine the mean material properties of the bridge materials including the concrete for girder, the concrete for slab in between girders, the reinforcing steel and the prestressing steel - a detailed account on the investigation can be found in [5, 13]. The results obtained are tabulated in table 5.2 with the corresponding class of material that the obtained properties can be classified to. Tests 1-3 are performed on the bridge system to study the effect of neighboring beams and the development of compressive membrane action in bridge deck slab, this study is beyond the scope of the MSc. project and hence is not discussed further.

The most relevant tests for this project are the tests 4-7, as they have been performed on a single beam. The beams have been disconnected from the bridge system using a saw cut through deck slab and cross-beams (figure 5.6). However, the end cross-beam on the far side of the beam is left intact for stability of the beam during the test. Tests 4, 5 and 6 are performed with the load at a distance of 2250mm from the support while test 7 is performed with the load at a distance of 4000mm from the support. A summary of the relevant test description is presented in table 5.1.

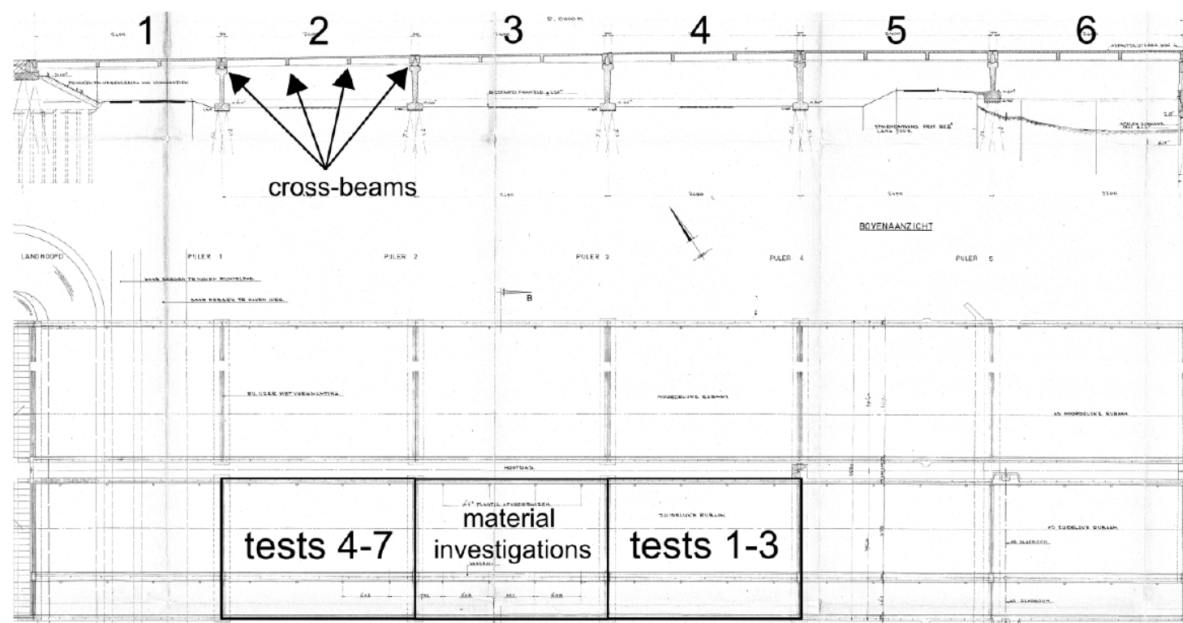


Figure 5.2: Layout of the Vechtbrug with marked test locations [7]

Table 5.1: Test description - summary

Test No.	Load (mm)	Description
4	2250	Single beam
5	2250	Single beam
6	2250	Single beam
7	4000	Single beam

5.2. Description of Vechtbrug Beam

The standard cross-section of the Vechtbrug beam is T-shaped, as shown in sub-figure (a) of figure 5.3, with the reinforcement detailing. Each beam has a 750mm long end block on both sides with the thickness equal to the thickness of bottom flange i.e. 400mm. For the transition from end block to the standard cross-section, a 1000mm long curved transition piece is used. All the beams are post-tensioned using 7 tendons - 6 tendons are anchored in the end block while the seventh tendon is anchored in the top flange at a distance of 1902mm from the support as shown in figure 5.4. The tendons have both, vertical and horizontal curvature along the length of the beam.

For individual beam tests the slab has been cut through the center line of the deck slab in between girders (figure 5.6) resulting in a total top flange width of 1225mm, from which 800mm is girder concrete and 425mm is slab concrete - 212.5mm on both sides of the flange. The beams are supported using elastomeric bearings with a size of 206x306mm, following the construction drawings of the Vechtbrug.

The total span of the beam is 24m with a cross-beam at every 8m. The end cross-beams are 400x850mm and are prestressed using 5 tendons while the intermediate cross-beams are 500x950mm and are prestressed using 8 tendons. The details of cross-beams can be seen in figure 5.5.

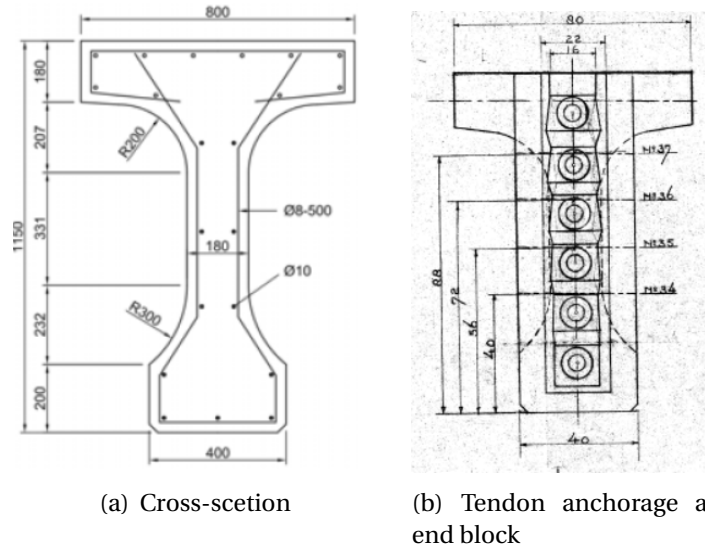


Figure 5.3: Cross-section and tendon anchorage

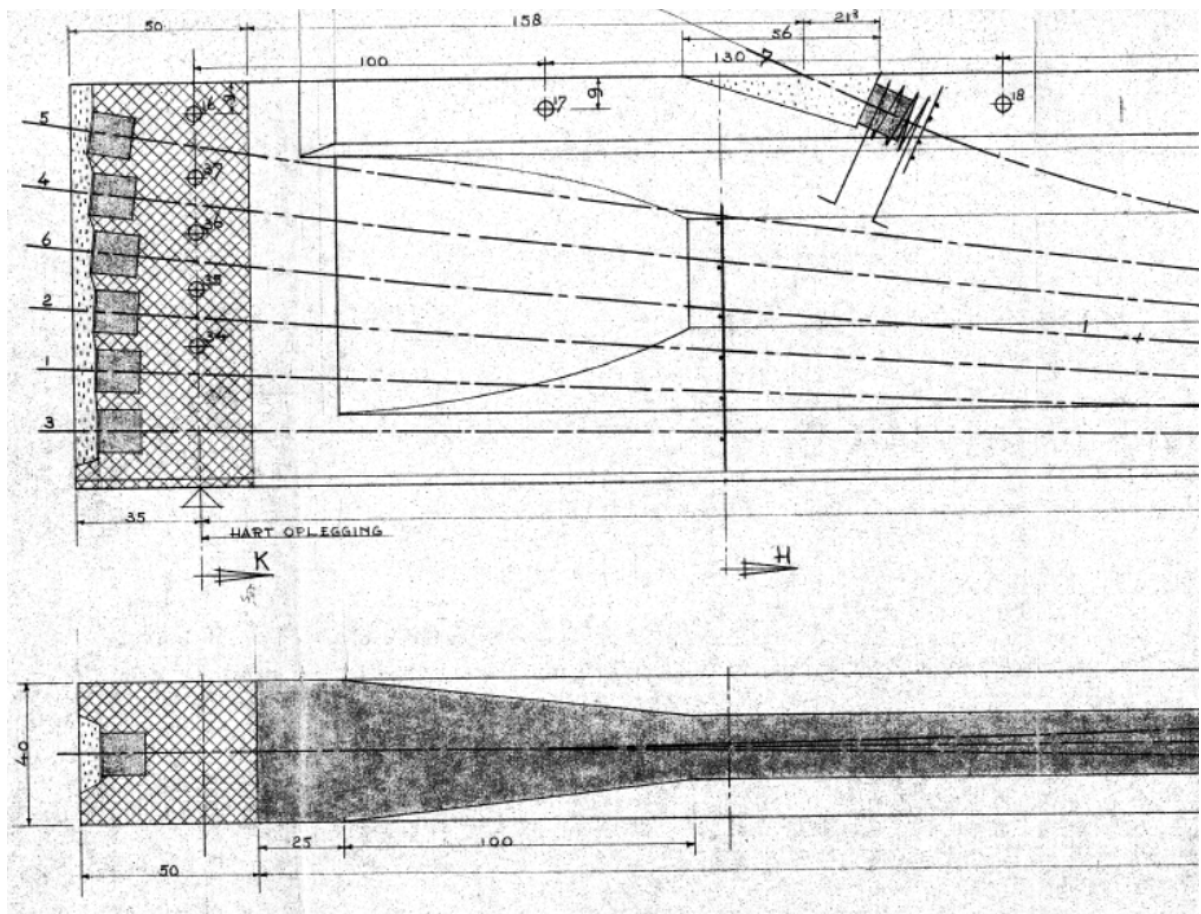


Figure 5.4: Beam geometry and tendon anchorage

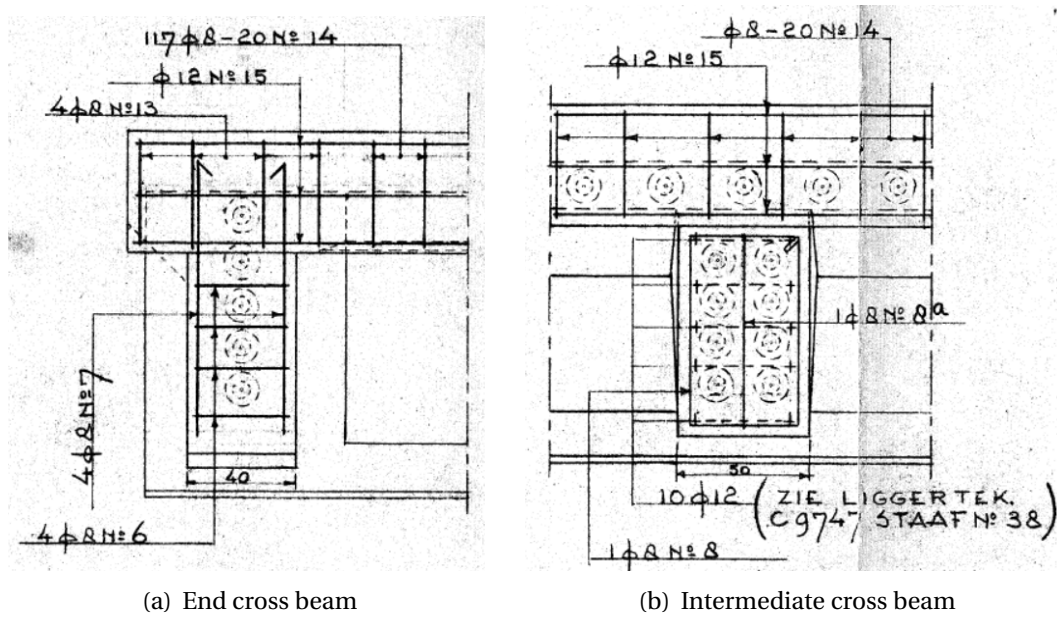


Figure 5.5: Cross beam detail

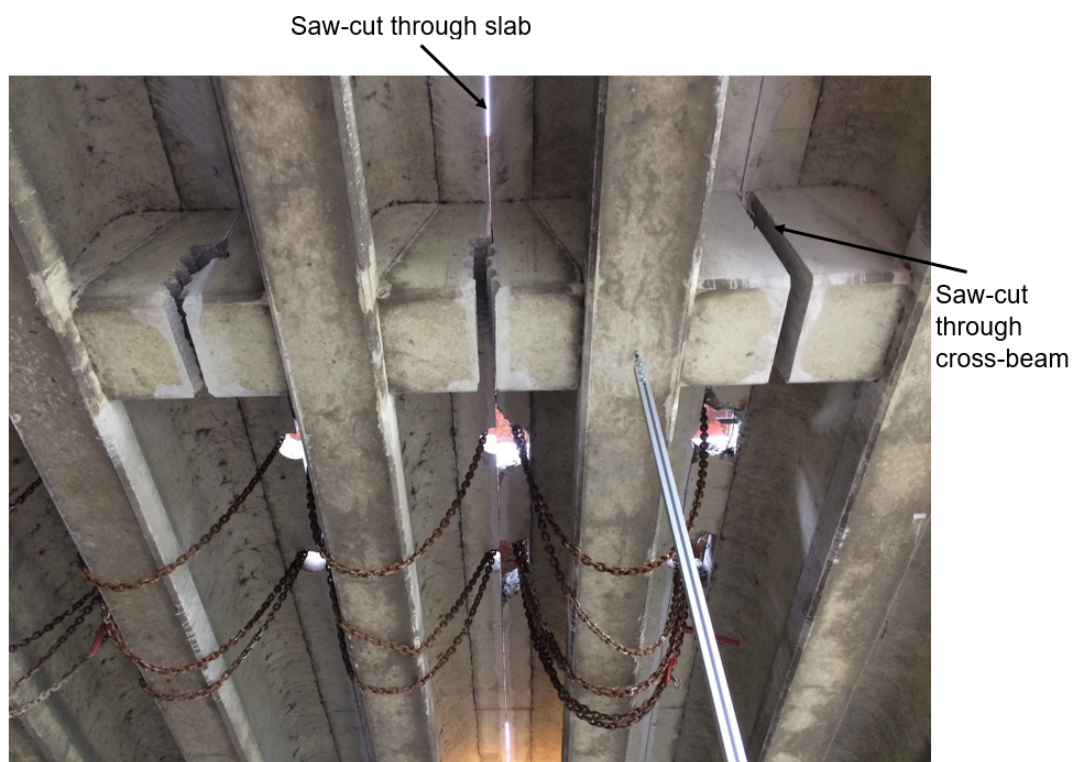


Figure 5.6: Saw-cuts used for individual beam tests

5.3. Results of Material Testing

The material testing on span 3 of the bridge as shown in figure 5.2 shows that the average compressive strength of the girder concrete is 106.7 MPa and the compressive strength

of slab concrete is 73.5MPa [5]. Owing to the dimensions of the tested cylinders, the resulting values are multiplied with a factor of 0.85 to obtain the mean cylindrical compressive strength of concrete which comes out to be 90 MPa for girder concrete and 62MPa for slab concrete. The yield strength of reinforcing steel is found to be 288MPa and a fracture strength of 352MPa - this corresponds to the steel quality QR24 as mentioned in the measurement report [13]. Similarly, the prestressing tendons are found to be of class QP170, which was used quite a lot during the 60s and 70s, with $f_y = 1505$ MPa and $f_u = 1770$ MPa [13]. The results are also summarized in table 5.2.

Table 5.2: Material investigation results

Material	Strength (MPa)	Class
Girder Concrete	90	C90
Slab Concrete	62	C60
Reinforcing Steel	$f_y = 288, f_u = 352$	QR24
Prestressing Steel	$f_y = 1505, f_u = 1770$	QP170

5.4. Results of Individual Beam Tests

For all the individual beam tests, the deformation readings are measured at 3 locations - at the point of application of load, at the level of the first intermediate cross-beam and near the support. Part of the bridge deck used for the single beam tests with location of load and LVDTs to measure the vertical deformation is shown in figure 5.7. It must be noted that the deformation at supports is measured at 20cm from the end of the elastomeric bearing. It can also be seen that the end-beam at the far end of the bridge is left intact as described earlier. An overview of the experimental set-up at the site can also be seen in figure 5.9.

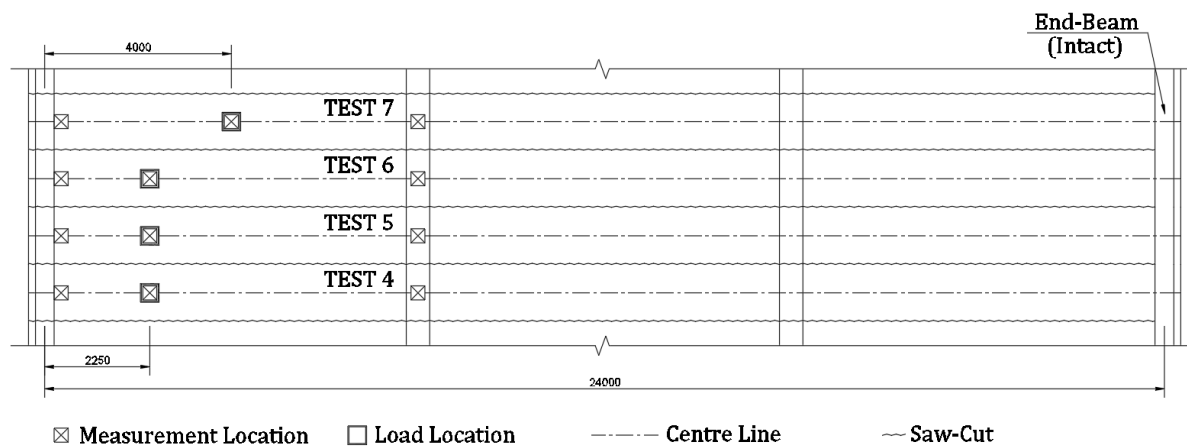


Figure 5.7: Experimental set-up and location of LVDTs

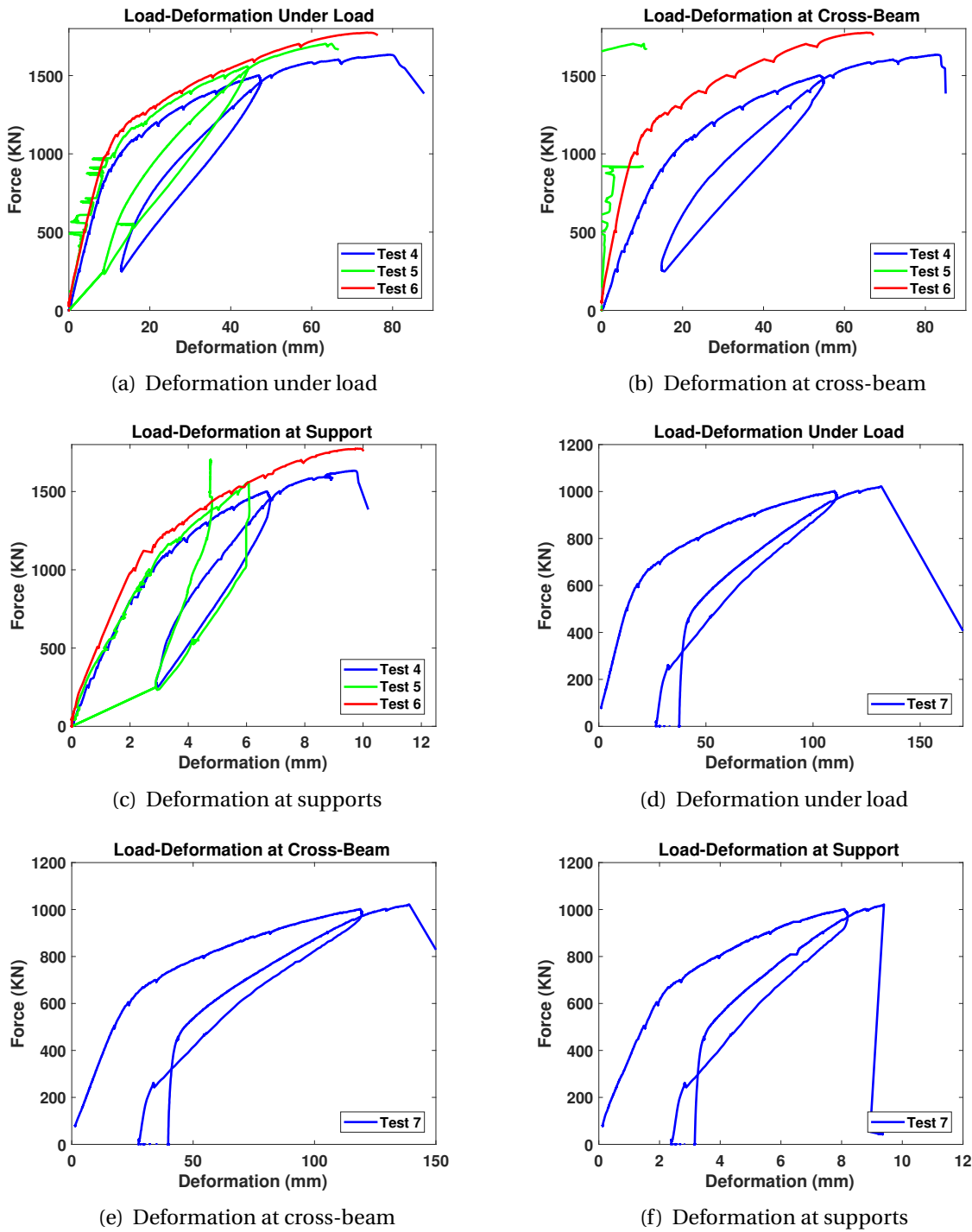


Figure 5.8: Results of individual beam tests

From the experimental results in sub-figures (a-c) of figure 5.8, it can be seen that Test 5 is within the range described by Test 4 and Test 6 but shows some unexpected readings, possibly due to an error in installing the LVDT. Hence, the results of Test 5 would not be used to make the comparison with the numerical models.



Figure 5.9: Overview of the test set-up used at site

6

Vechtbrug - Numerical Model

This chapter describes the 2D, 2.5D and 3D numerical models developed in DIANA for the individual beam tests (tests 4-7). The comparison of the numerical model results is made with the experimental results to validate the finite element models so they can be used further to study arching in beams as part of the bridge system (ignoring the distribution of load in the transverse direction).

6.1. Description of Vechtbrug Beam

The Vechtbrug beam has a total span of 24m with cross-beams at every 8m. A detailed description of the beam geometry, reinforcement and prestressing layout can be found in chapter 5. The longitudinal view of the beam is also shown in figure 6.1.

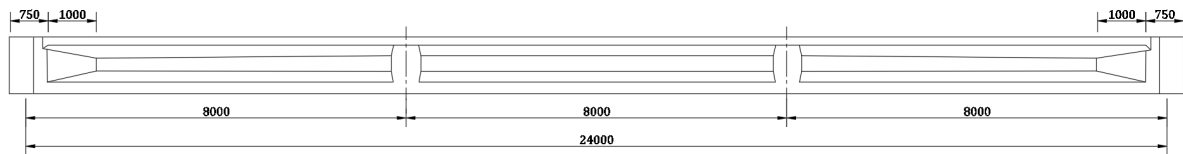


Figure 6.1: Longitudinal view of the beam

6.2. Geometry of the Beam

The standard cross-section of the beam is T-shaped with some variations along the length of the beam, like the 750mm long end blocks on both sides which have flanges of the same width as the standard cross-section but a constant web width of 400mm. Furthermore, as the beam is cut from the bridge system using saw cuts, it has some parts of the end and intermediate cross-beams connected to the main girder. This has also been modeled in the numerical analysis.

There is also a curved concrete transition piece of 1000mm on each side of the beam, but this has not been included in the numerical models. The beam is supported on linear elastic steel plates (206x306mm) and an interface has been used between the supporting plates and the beam to model the effect of elastomeric bearings. The loading plate is modeled either at a distance of 2250mm from the support or at 4000mm following the experiments.

6.2.1. 2D Model

To develop the 2D geometry in DIANA, use of spatial functions have been made which describe the variation in the cross-section of the beam as a factor of the maximum width. It must also be noted that for the 2D model, the concrete of the deck slab is transformed into the concrete of the girder using the ratio of compressive strengths, however this somewhat overestimates the stiffness. The total length of the slab extending from the flange was 425mm which is transformed to 293mm to give a total flange width of 1093mm. Based on the variations in the cross-section along the beam length, 4 different functions are defined (i) Girder (Standard cross-section) (ii) End blocks (iii) End cross-beam and (iv) Intermediate cross-beam. An overlay of all the functions is shown in figure 6.2. This must also be noted that the radii in the cross-section have been approximated using small linear lines for ease of modeling.

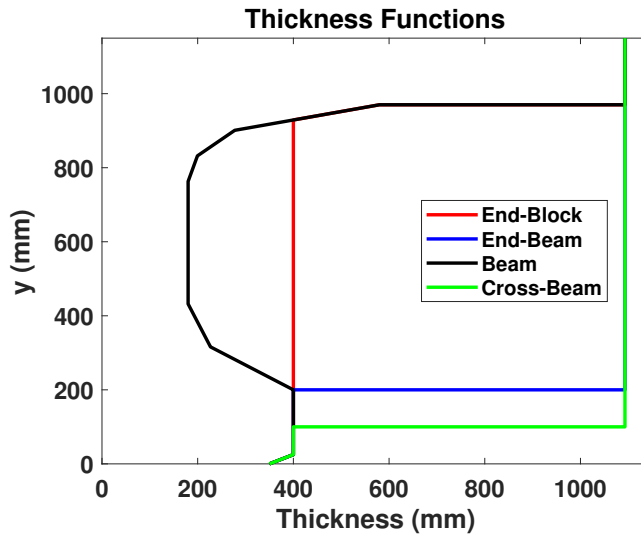


Figure 6.2: Cross-sectional function definition in 2D

In 2D model, all the reinforcing steel along the width of the beam is added up and shown as a single bar and the horizontal curvature of the tendon has also not been modeled owing to the restraints of 2D work environment. The longitudinal view of the 2D DIANA model is shown in figure 6.3 and the thickness function assigned to each part is also labeled with the same name as described in figure 6.2. The same color codes have been used in 3D and 2D shell model for each part of the beam.

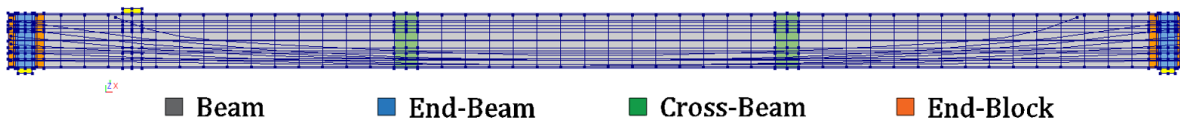


Figure 6.3: Longitudinal view of 2D model

6.2.2. 3D Model

In 3D model, both the deck slab concrete and the girder concrete have been modeled separately with the actual slab dimensions of 425mm at the flange level of the beam. The stirrups are modeled as per the details in the drawings (figure 5.3). The support and load plates are also modeled as solids with respective interfaces connecting them to the beam. The 3D work environment allowed the modeling of horizontal curvature of the tendons and it has also been included in the model. The 3D geometry and reinforcement layout of the model are shown in figure 6.4 and figure 6.5 respectively. It must be noted that the one of the end cross-beam is also modeled because it was not cut during the experiments. The reinforcement and prestressing tendons of this part of end cross-beam are also included in the model.

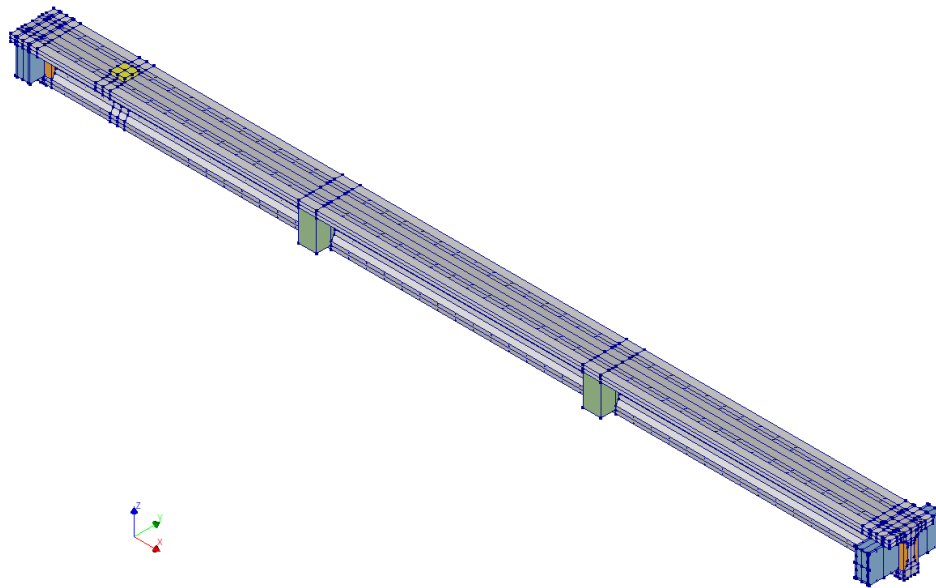


Figure 6.4: Isometric view of the 3D model

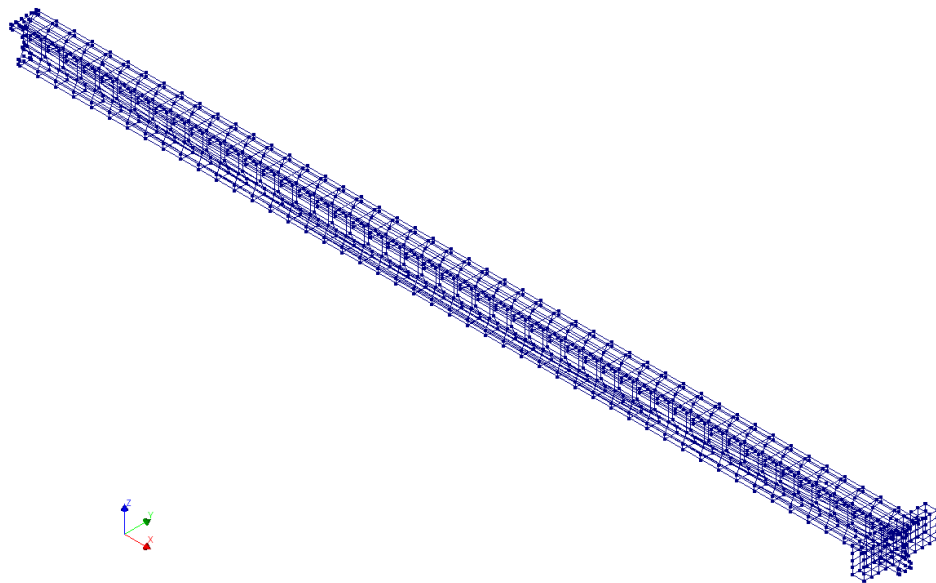


Figure 6.5: Isometric view of the reinforcement in 3D model

6.2.3. 2D Shell Model

A so-called 2.5D model of the beam is also prepared using shell elements. This has been done to be able to model the torsional behavior of the end-beam in a better way and still be able to produce a computationally cheap model. Apart from the end cross-beam, the shell elements have been assigned the geometry as described for the 2D model in subsection 6.2.1. The end cross-beam and the reinforcement layout is modeled as described for the 3D model in subsection 6.2.2. The 2D shell model with reinforcement is shown in figure 6.6. At the level of end cross-beam, the 2D shell sheet meets the 3D solid and results in a concentrated line load, to avoid this the use of tying has been made for a width of 400mm

i.e. the width of the end-block. The horizontal deformation (T1) and the shell element rotations (R1 and R3) of the edges of the end-block are tied to the point of connection of the shell elements with the end-block as shown in figure 6.7

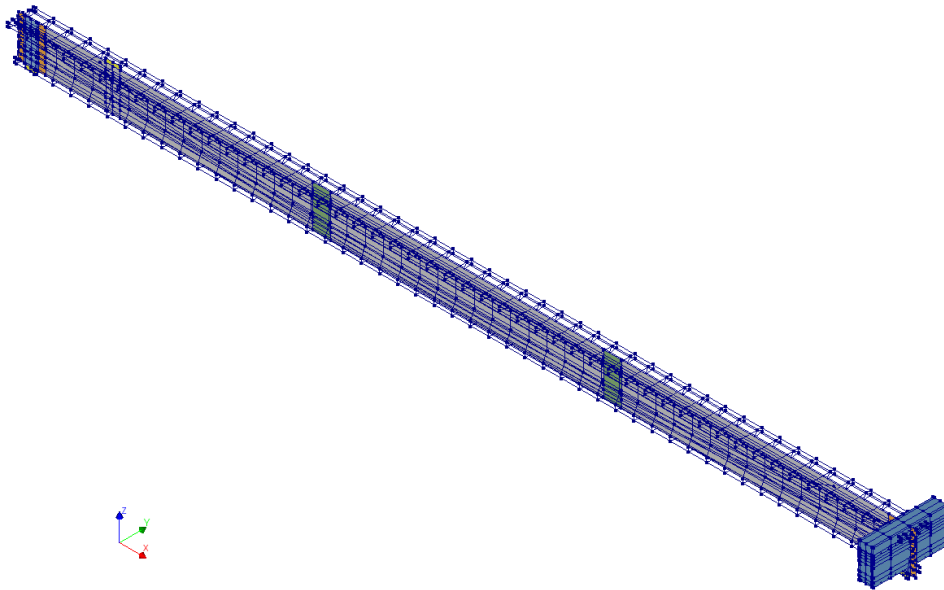


Figure 6.6: Isometric view of the 2D shell model

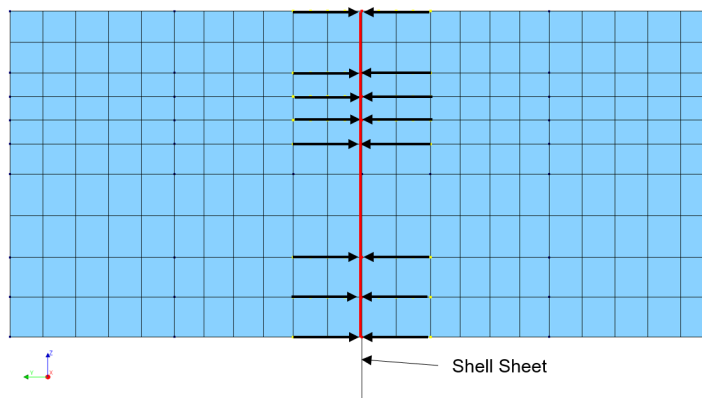


Figure 6.7: Tying used in shell model

6.3. Material Properties

The material properties used for concrete, reinforcing steel and prestressing steel are the same for all the models. The properties are derived from the experimental results as described in chapter 5. The mean material values are used because a comparison of the model has to be made with the experimental results.

6.3.1. Concrete

The girder concrete has a mean compressive strength of 90MPa while the slab concrete has a mean compressive strength of 62MPa. For the compressive behavior of concrete a parabolic compressive curve is used and for tensile behavior, Hordijk's tension softening

curve has been used. The modeled compressive and tensile behavior of concrete is shown in figure 6.8 and table 6.1.

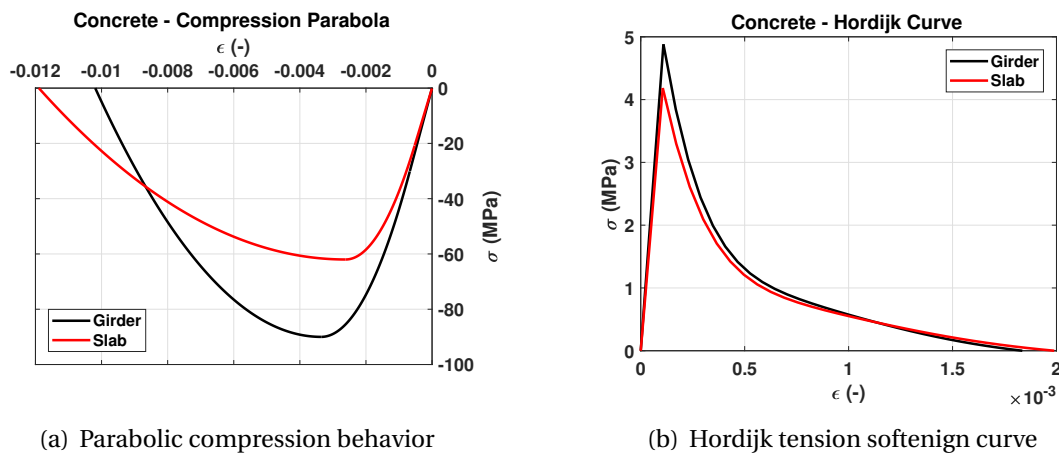


Figure 6.8: Behavior of concrete for Vechtbrug beam model

Table 6.1: Properties of concrete in DIANA for Vechtbrug models

Property	Girder Concrete	Slab Concrete
Material class	Concrete and Masonry	
Material model	Total strain based crack model	
Young's modulus, E	44722 MPa	39497 MPa
Poisson ratio, ν	0.15	
Mass density	2400 kg/m^3	
Crack orientation	Rotating	
Tensile curve	Hordijk	
Tensile strength, f_{ct}	4.84 MPa	4.19 MPa
Mode-I tensile fracture energy, G_f	0.153 N/mm	0.149 N/mm
Crack band-width	Govindjee	
Poisson's ratio reduction	Damage based	
Compressive curve	Parabolic	
Compressive strength, f_c	90 MPa	62 MPa
Compressive fracture energy	41 N/mm	38 N/mm
Reduction model	Vecchio and Collins 1993	
Lower bound reduction curve	0.40	
Confinement model	Selby and Vecchio	

6.3.2. Reinforcing and Prestressing Steel

Following the results of the experiments, the reinforcing steel is classified as QR24 and the prestressing steel as QP170. All the reinforcements are modeled as embedded reinforcements i.e. they are fully bonded to the mother elements or no slip is considered between concrete and steel. The modeled behavior of both the materials is shown in figure 6.9.

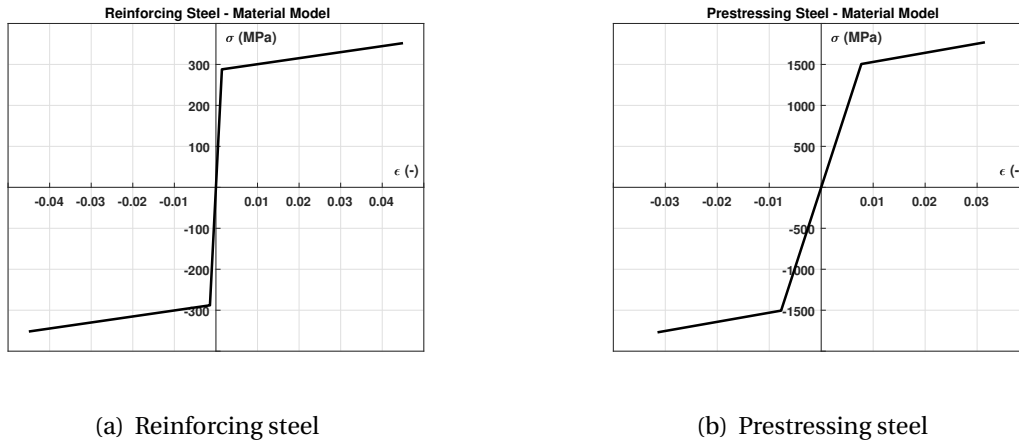


Figure 6.9: Behavior of reinforcing and prestressing steel

6.3.3. Load and Support Plate Interface

The load and support plates are modeled as linear elastic steel since these are subjected to concentrated loads in the model. These plates are connected to the beam through an interface to avoid localization of stresses and to model the effect of elastomeric bearings on the beam deformations.

The properties of load interface are derived from the properties of girder concrete as suggested in RTD 1016-3B [3]. The normal stiffness of the interface is equal to the Young's modulus of girder concrete and the shear stiffness is a factor of 1000 lower. This helps avoid the localization of stresses at the point of application of the load.

The properties of support interface are determined using the calibration of the model as per the experimental results by Ensink and can be expressed using equation (6.1) and equation (6.2).

$$k_{normal} = \frac{475 * 1000}{l_s b_s} = \frac{475 * 1000}{306 * 206} = 7.53 N/mm^3 \quad (6.1)$$

$$k_{shear} = \frac{0.90}{2 * 15.5} = 0.029 N/mm^3 \quad (6.2)$$

Where, l_s and b_s are dimensions of the elastomeric bearing.

6.4. Loads

6.4.1. Prestressing Loads

The beam is prestressed using 7 tendons which are modeled as embedded reinforcement, as mentioned earlier. All the tendons are loaded using the reinforcement bar prestress option in DIANA, which means that the stress is same throughout the length of the tendons. The time dependent losses of the prestress are assumed to be 20%, which results in a working stress of 867 MPa in the prestressing tendons. Hence, a stress of 867 MPa is assigned to all the tendons.

In 3D model, the end beam is also modeled which is prestressed in the transverse direction using 5 similar tendons. The equivalent stress on the concrete has been calculated as shown in equation (6.3).

$$\sigma_{cp} = \frac{\sigma_{p\infty} * n * A_p}{A_c} = \frac{867 * 5 * 462}{400 * 850} = 5.89 N/mm^2 \quad (6.3)$$

This stress has been applied on the faces of the end beam as an external face load to model the effect of prestress in the transverse direction.

As a refinement of the models, the post-tension load option is also used in DIANA. This allows to take into account the effects of wedge set, friction losses and wobble affects to get a more realistic stress distribution in the tendons. The values used for the friction and wobble coefficients are taken from section 3.3 of RBK 1.1 [16] and are listed in table 6.2 along with the recommended value of normal wedge set for the used prestressing system (Tabel B4-1 of RBK). All the tendons are stressed from both sides with left side as first anchor for all odd numbered tendons and right side as first anchor for even numbered tendons. In all the tendons, overstressing of 10% has been used to take into account the anchorage losses.

Table 6.2: Properties used for post-tensioning load

Description	Value	Unit
Friction coefficient (μ)	0.26	-
Wobble coefficient (ω)	0.01	/m
Wedge set	7	mm
Over-stressing	10	%

6.4.2. Applied Load

The load on the beam is applied as a point deformation at a distance of 2250 or 4000mm from the support, depending on the experiment. As an imposed deformation is applied a support is also needed at the point of application of the load and it has also been modeled as shown in figure 6.10. The applied deformation has a magnitude of 1mm.

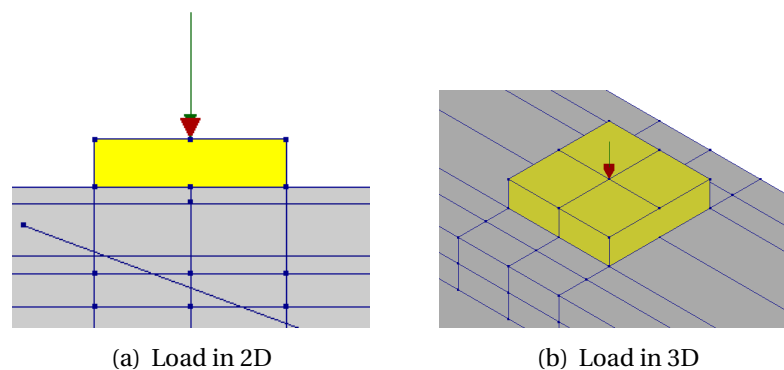


Figure 6.10: Application of load in DIANA

6.5. Behavior of the End-Beam

As the end cross-beam at the far end of the beam is not sawed during the experiments, its behavior under loading has to be determined. This beam is believed to be loaded in torsion, given the Vechtbrug beam geometry, and it is known that after cracking the torsional

stiffness reduces to around 20% of its initial value - this knowledge has been used to verify the numerically obtained behavior of the end-beam. To study the behavior of the end-beam under torsion, a 3D model of the end-beam is generated with the same dimensions, reinforcement and prestressing layout as the end-beam in the Vechtbrug beam model. The beam (gray in sub-figure (a) of figure 6.11) is assigned the properties of non-linear end-beam concrete while the central part (yellow in color) is assigned the properties of linear elastic steel to avoid any effect of localization due to point loads. The edge face of the end-beam is divided in top and bottom part using the imprint command in DIANA (red line in sub-figure (b) of figure 6.11) and the use of tying option is made to tie the deformations of top and bottom half of the edge faces to the corner node as shown by black lines in sub-figure(b) of figure 6.11 - this allows to model the restrained offered by neighboring beams and to extract the reaction forces on the edge face as concentrated loads. The model is also initially prestressed using external force as in actual beam model and then the point loads are applied to load beam in torsion. The applied prestressing can be seen in sub-figure (a) of figure 6.11.

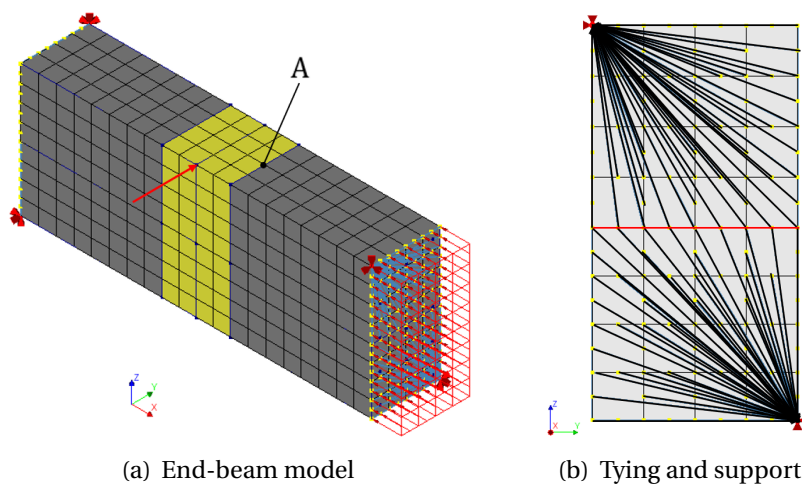


Figure 6.11: Tying and supports for end-beam model

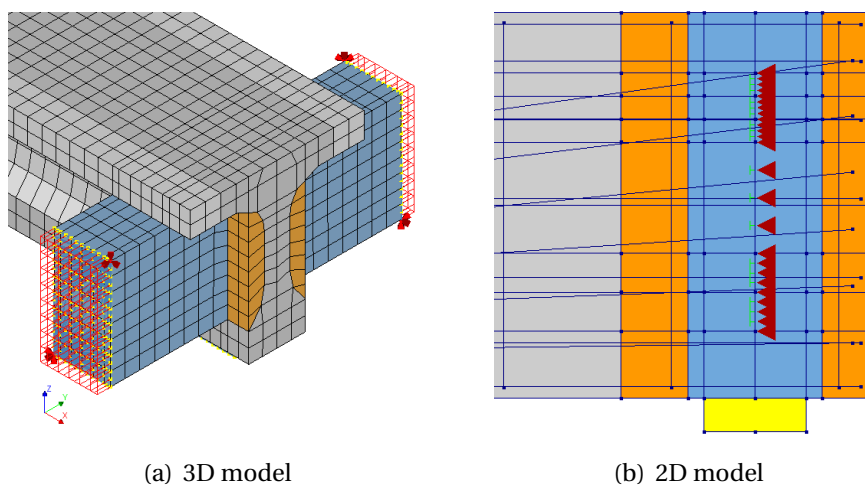


Figure 6.12: Tying and supports for end-beam

To further verify the assumed loading condition of the end-beam in Vechtbrug, similar support and tying options are used for the end-beam in the Vechtbrug beam model as shown in figure 6.12.

In both, the end beam model and the Vechtbrug beam model, the crack pattern is quite similar with diagonal torsional cracks in the non-linear concrete. A comparison of the cracks in the end-beam at the final load step for Vechtbrug beam loaded at 2250mm and 4000mm is shown in figure 6.13. The bigger cracks in the end-beam for load at 4000mm might be explained by the relative proximity of the load to the end-beam and higher ductility of the Vechtbrug beam due to shear bending effect.

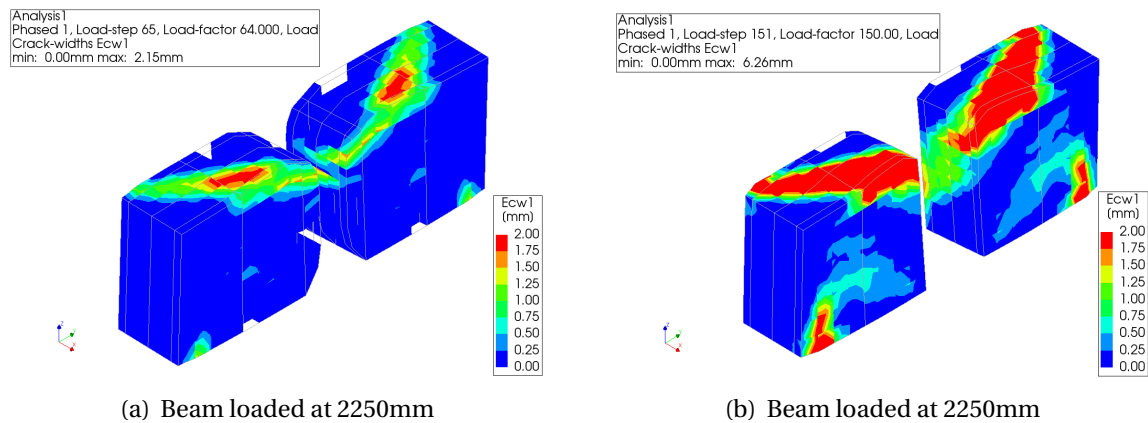


Figure 6.13: Torsional cracks in the end-beam

Using the reaction forces from the tying option and the deformations at the central inner node of the end-beam (Point marked A in sub-figure (a) of figure 6.11), the moment-rotation behavior of the model is obtained.

In the 2D work environment it is not possible to directly model the end-beam on the Vechtbrug beam hence a linear spring interface is used as shown in sub-figure (b) of figure 6.12. The input for the line interface is a force-displacement behavior hence the moment-rotation plot is transformed into a force-displacement plot using beam geometry. The resulting load-deformation plots are shown in figure 6.14 which is in accordance with the expectations i.e. the stiffness reduces to around 20% of the initial stiffness after cracking.

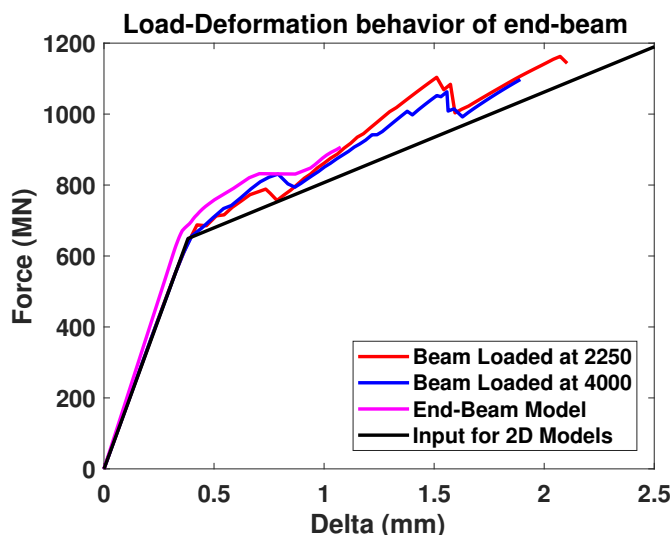


Figure 6.14: Force-deformation behavior of end-beam

It can be seen that the model generated for the study of torsional behavior gives quite comparable results with the end-beam in the actual beam model, for the load at either 2250 or 4000mm, hence the same approach is also used to determine the torsional behavior of the intermediate cross-beam. The selected input for the behavior of the linear interface in 2D model is also shown in figure 6.14, as the end-beam cannot directly be modeled.

6.6. Support Conditions

The Vechtbrug beam is supported using elastomeric bearing (properties in section 6.3). To model this behavior an interface is used between the support plates and the beams. The deformation of the support plates are tied to a single (central) node of the bottom edge and the left support plate is supported in vertical direction while the right support plate is restrained in both vertical and horizontal direction as shown in figure 6.15 - the same has been done for 3D and 2D shell models. As mentioned earlier, an additional support is added at the center of the top edge/face of the loading plate for the application of imposed deformation.

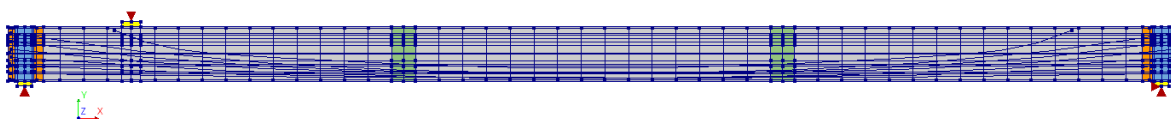


Figure 6.15: Supports of beam in 2D

The supports and tying option used to model the torsional behavior of the un-cut end-beam are discussed in section 6.5.

6.7. Mesh

A wide range of structural elements can be used in DIANA [9] for analysis of structures. As both 2D and 3D models are developed, different element types have been used for the analysis. It must be noted that for the same given size of element the 3D model requires a lot more computation time and storage than the 2D model.

6.7.1. 2D Model

The mesh set-up for the 2D model is quadratic with regular plane stress element i.e. $\sigma_z = 0$. The elements size is specified using the edge meshing option and a size of 100mm. The elements used in 2D model are shown in figure 6.16.

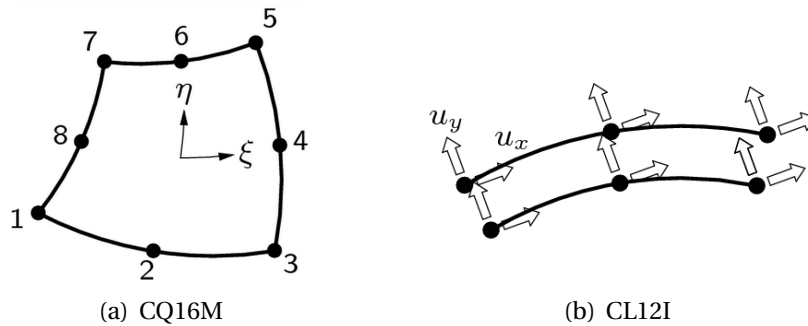


Figure 6.16: Elements used in 2D model

CQ16M is an eight-node quadrilateral isoparametric plane stress element which uses quadratic interpolation and Gauss integration. It has 2 degrees of freedom per node (u_x and u_y). By default a 2x2 integration scheme is used to yield optimal stress points. The interface elements used in the 2D model are CL12I, these also have quadratic interpolation scheme and 2 variables per node making them compatible with the plane stress elements. By default a 3-point Newton-Cotes integration scheme is used for these elements.

6.7.2. 3D Model

The mesh generating algorithm in DIANA for 3D structures sometimes results in a mesh with quite sharp edges which causes convergence issues and compromises the reliability of the finite element model. Hence the mesh is generated using the 2D sheet element and these elements are then extruded to give a 3D solid structure - this allows to have more control over the mesh. As for 2D model, a general element size of 100mm is used with quadratic elements. The cross-sectional view of the final mesh is shown in figure 6.17 and an isometric view of the mesh is shown in figure 6.18.

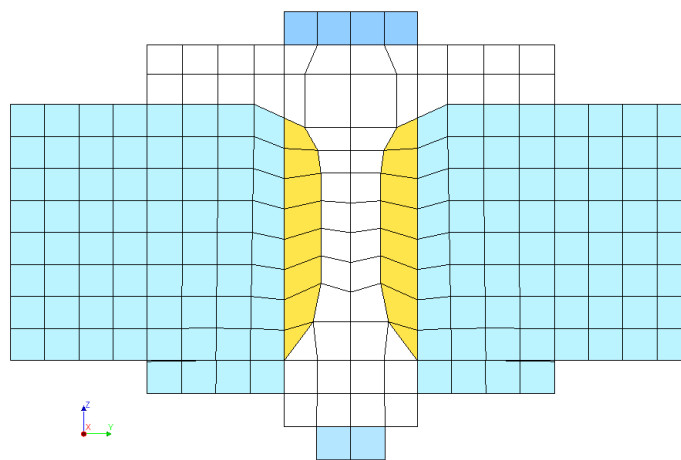


Figure 6.17: 3D cross-sectional mesh

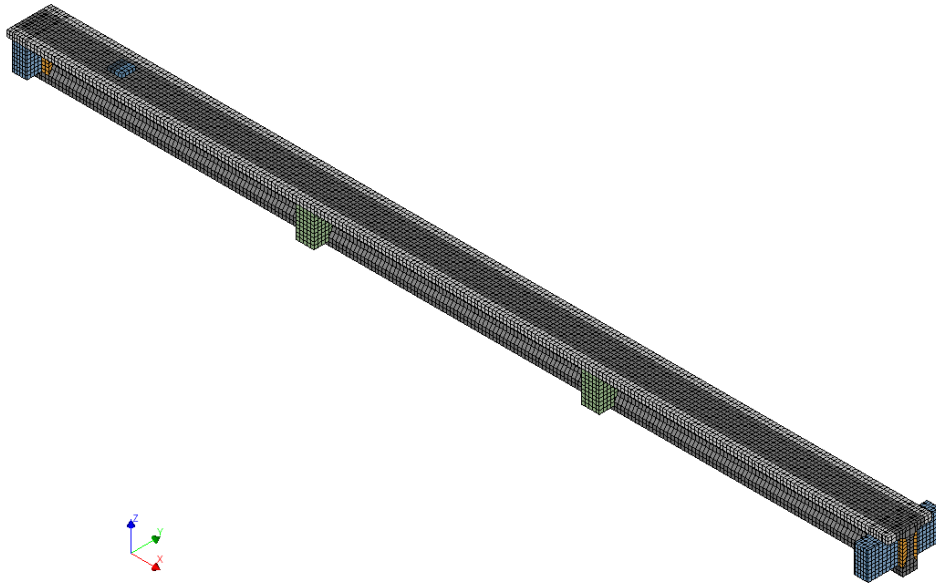


Figure 6.18: 3D isometric mesh

As can be seen from figure 6.17, most of the elements used are cubic brick elements with few wedge shaped elements. In brick element not only the geometry of the element is 3D but the stress situation is also 3-dimensional. All the elements used in 3D model are shown in figure 6.19.

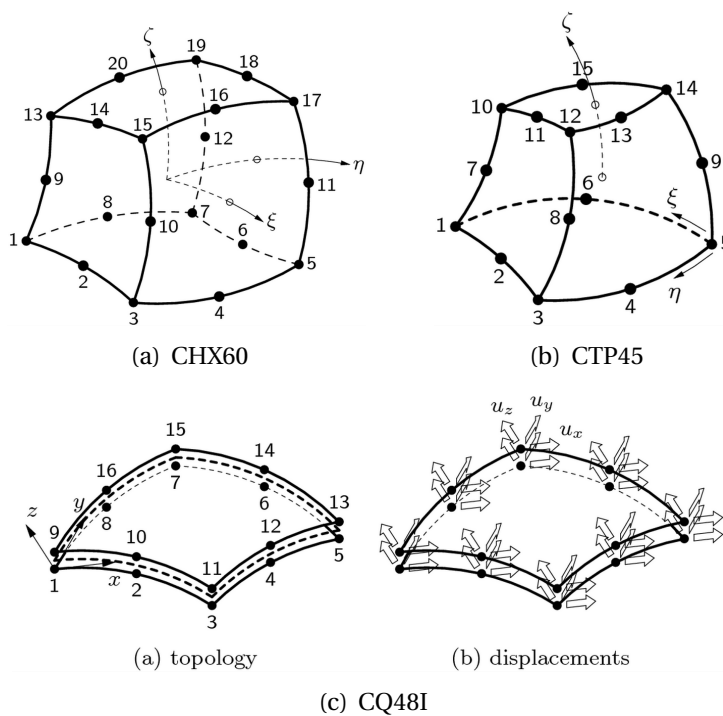


Figure 6.19: Elements used in 3D model

The most commonly used brick element is CHX60. It is a twenty-node isoparametric solid brick element which uses quadratic interpolation and Gauss integration. CHX60 has

3 degrees of freedom per node (u_x , u_y and u_z). A $3 \times 3 \times 3$ integration scheme is used by default in DIANA. CTP45 is a fifteen-node isoparametric solid wedge element with quadratic interpolation and numerical integration. It has the same degrees of freedom per node as CHX60. CQ48I is a surface interface element between two 3-dimensional bodies, it uses quadratic interpolation and a $3 \times 3 \times 3$ Newton-Cotes integration scheme.

6.7.3. 2D Shell Model

The mesh setting used for 2D shell model is the same as for the 2D model with plane stress elements. The elements used in the 2D shell model are shown in figure 6.20.

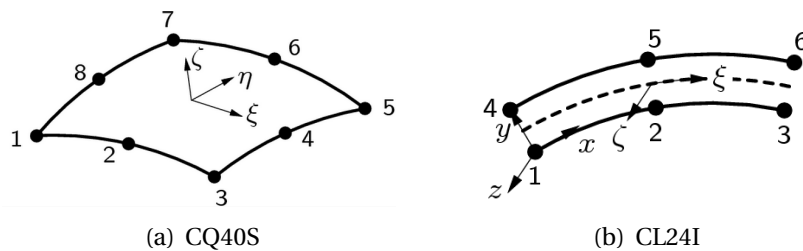


Figure 6.20: Elements used in 2D shell model

CQ40S is an eight-node quadrilateral isoparametric curved shell element which uses quadratic interpolation and Gauss integration in ξ and η , in thickness direction Simpson integration is used. It has 5 degrees of freedom per node i.e. u_x, u_y, u_z, ϕ_x and ϕ_y . To avoid shear and membrane locking a reduced integration scheme of 2×2 is used by default. CL24I acts as an interface element between the two curved shell elements. In ξ direction a 3-point Newton-Cotes and in thickness direction a 3 point Simpson scheme is used.

6.8. Analysis Set-up

The Vechtbrug beam is prestressed and a displacement controlled analysis is performed, which means that the use of phased analysis has to be made. In the first phase the prestressing and dead weight of the beam are applied simultaneously using 4 load steps (0.5 0.25 0.125(2)) and the support for deformation application is switched off. This phase results in a beam with a certain camber as expected. Once the prestressing is applied, the support for load application is switched on and a start step is used to let the model adjust to this change. Following this, the load is applied on the beam with a step size of 1mm until numerical failure which corresponds to the energy norm exceeding 1%, crushing of concrete or fracture of steel. For 3D and 2D shell model, there is an additional load step after the prestress and before switching on the support for load application. This is to apply the transverse prestressing in the end-beam on the far side of Vechtbrug beam. The supports for the end-beam are switched on once the transverse prestressing has been applied.

An energy norm is used for all the analysis with a tolerance of 0.001. A maximum of 100 iterations for 2D and 50 iterations for 3D and 2D shell model are used. The convergence behavior for all the 2D and 3D models described in this section can be seen in Appendix A.

6.9. Results

For the validation of the numerical models, the numerical results are compared with the experimental data in terms of load-deformation behavior at the point of application of load, at the level of cross-beam and near the support. Comparison is also made in terms of the cracking behavior.

6.9.1. Load at 2250mm

The load-deformation response of all the numerical models with load at 2250mm is shown in the same figure (figure 6.21) and some of the selected results from DIANA output are shown separately for comparison (figures 6.22, 6.23 and 6.24). It can be seen from figure 6.21 that all the numerical models have similar load-deformation behavior with a maximum difference of 10% in the peak load. The peak loads of the numerical models are also comparable to the experimental results with a difference of 2.9%, 7% and 0.3% for 2D, 3D and 2D shell model respectively.

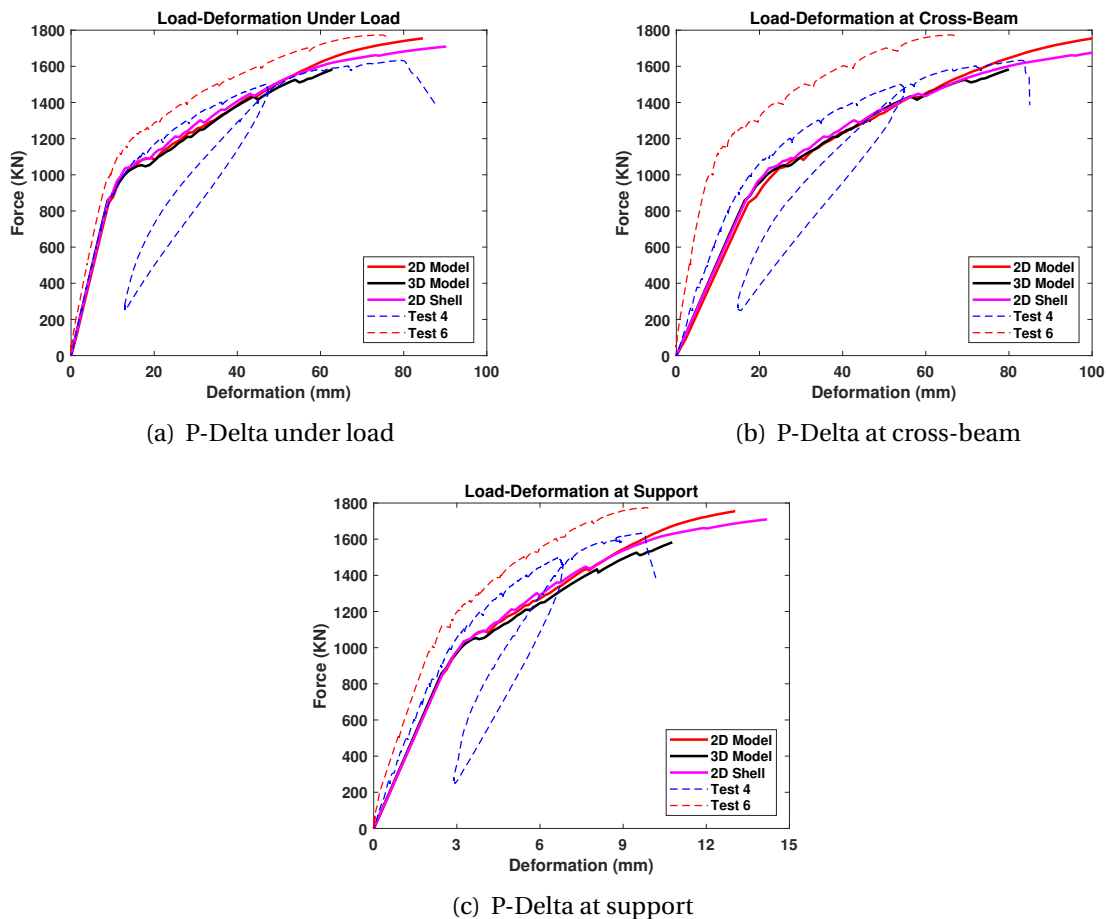


Figure 6.21: Load-deformation comparison of numerical models and experiments for load at 2250mm

In general, the numerical models are also able to capture the load-deformation behavior of the beam, especially under the point of application of the load as both the initial and final stiffness of the models are quite close to the experimental results. In all the models the numerical failure occurs due to the crushing of concrete at the point of application of the

load. The 3D model seems to have lower deformation capacity compared to the 2D and 2D shell models, hence the peak load is also underestimated by 7% - a summary of the peak load comparison is given in table 6.3.

Comparing the sub-figures (a) and (b) of figures 6.22, 6.23 and 6.24 it can be seen that the application of prestressing in all the models has similar effects in terms of stresses in tendon (difference < 1.3%) and camber of the beams (difference < 5%). Similarly, it can be seen that for all the models the prestressing steel has yielded at the final load step but the stresses are still lower than the fracture strength. From the comparison of sub-figure (c) it can be seen that the 3D model is least ductile with the final deformation of 76mm (25% lower) compared to 100mm for 2D and 108mm for 2D shell model.

Comparison of sub-figure (e) shows that the crack pattern is a bit different for 3D and 2D models as the 3D model shows a single major shear crack between the point of application of the load and the supports while in both, the 2D and 2D shell model, an additional crack between the loading point and first intermediate cross-beam is also observed. The results of the 3D model are closest to the experimental observations in terms of cracking - the resulting cracks after test 4 and test 6 can be seen in figure 6.25 for comparison. It must be noted that the crack pattern shown is at the last load step before numerical instability for all the models hence there are some obvious differences in the observed results because the total applied deformation is different.

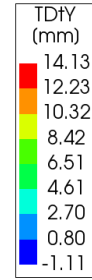
The comparison of the computation time required for each analysis is also shown in table 6.3 and it can be seen that using the 2D model is much economical in terms of time as it take only 2% of the time required for a full 3D analysis.

Table 6.3: Peak load and computation time comparison for load at 2250mm

Description	Peak load (KN)	Time (min)
Test 4	1634	-
Test 6	1773	-
2D model	1754	16
3D model	1582	786
2D shell model	1709	104

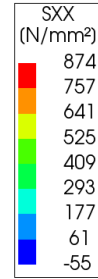
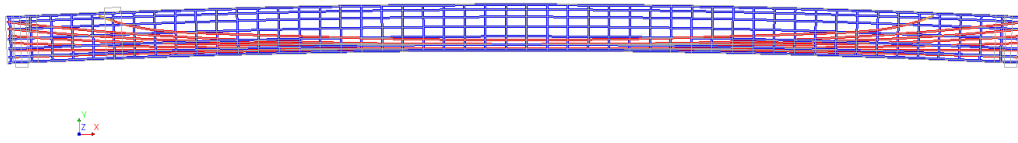
It can be concluded that the numerically cheap 2D models are able to predict the peak load and load-deformation behavior in good accordance with the experiments but for the study of the cracking pattern a 3D model is to be preferred.

Analysis 1
 Phased, Start-step 5, Load-factor 1.0000
 Displacements TDtY
 min: -1.11mm max: 14.13mm



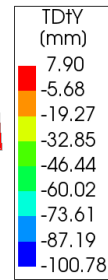
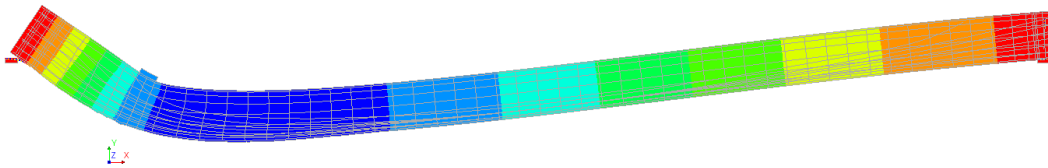
(a) Deformation after prestressing

Analysis 1
 Phased, Start-step 5, Load-factor 1.0000
 Reinforcement Cauchy Total Stresses SXX
 min: -55.43N/mm² max: 873.61N/mm²



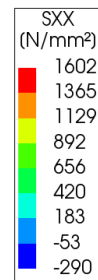
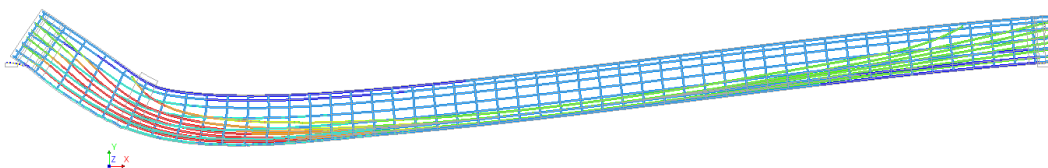
(b) Stress in tendons after prestressing

Analysis 1
 Phased 1, Load-step 85, Load-factor 84.000, Load
 Displacements TDtY
 min: -101mm max: 8mm



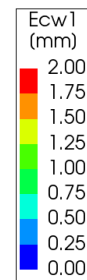
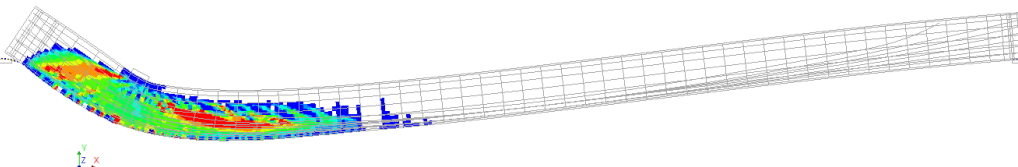
(c) Deformation at final load step

Analysis 1
 Phased 1, Load-step 85, Load-factor 84.000, Load
 Reinforcement Cauchy Total Stresses SXX
 min: -289.78N/mm² max: 1601.75N/mm²



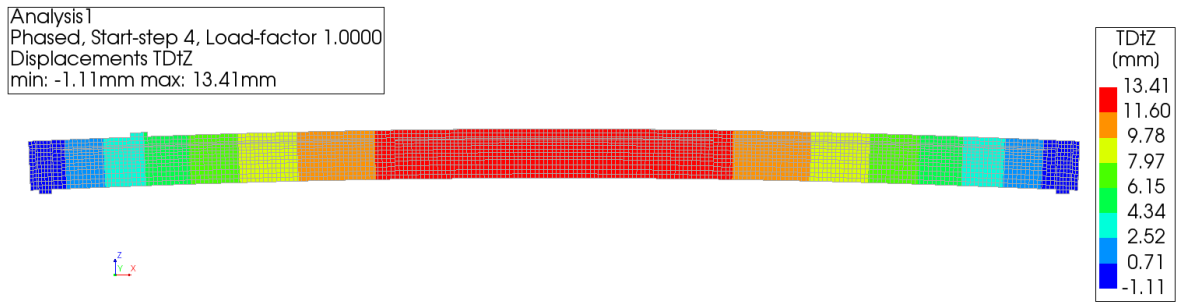
(d) Stress in tendons at final load step

Analysis 1
 Phased 1, Load-step 85, Load-factor 84.000, Load
 Crack-widths Ecw1
 min: 0.00mm max: 3.89mm

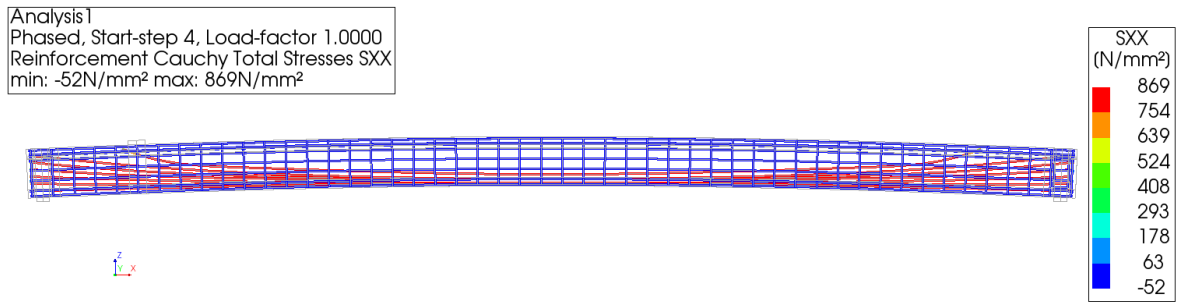


(e) Crack-widths at final load step

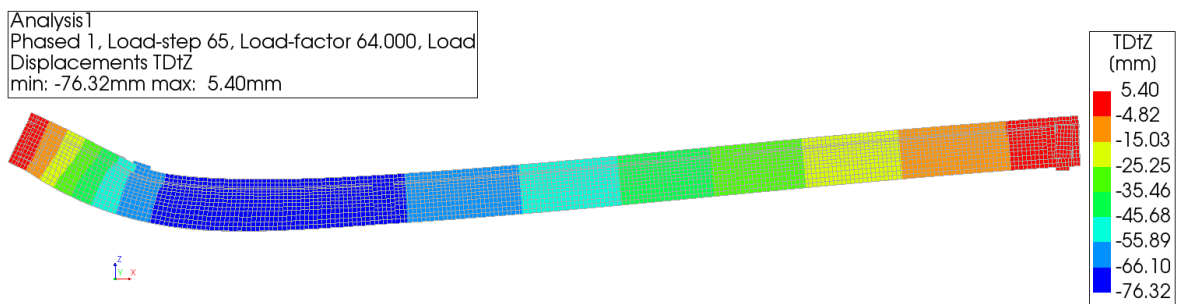
Figure 6.22: Behavior of the 2D model with load at 2250mm



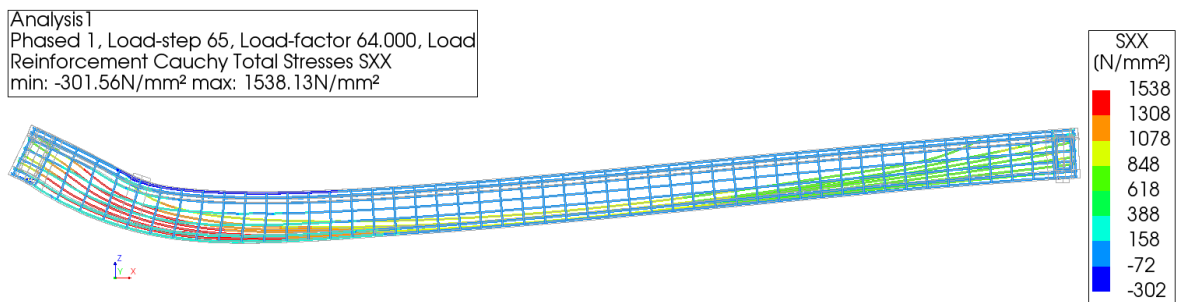
(a) Deformation after prestressing



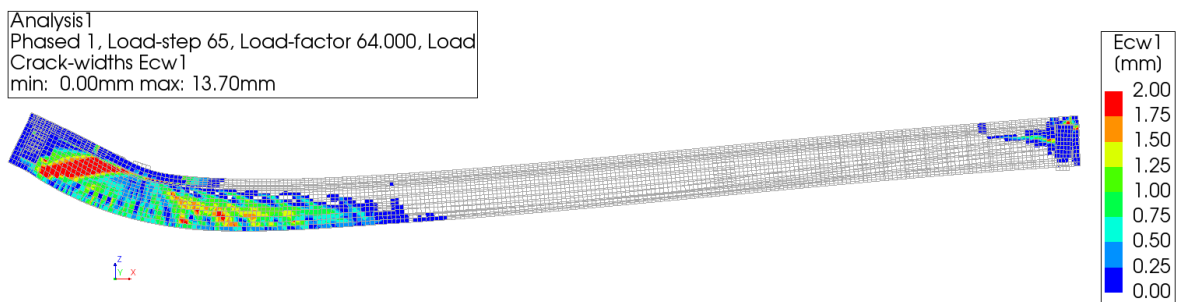
(b) Stress in tendons after prestressing



(c) Deformation at final load step



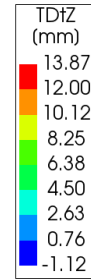
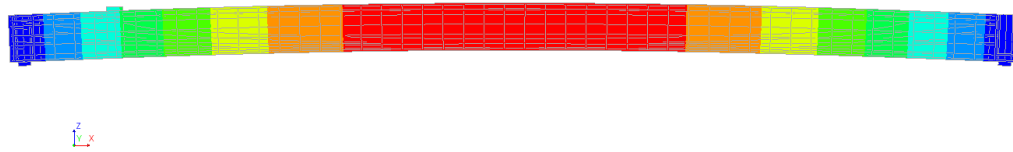
(d) Stress in tendons at final load step



(e) Crack-widths at final load step

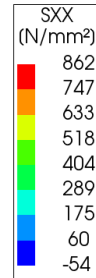
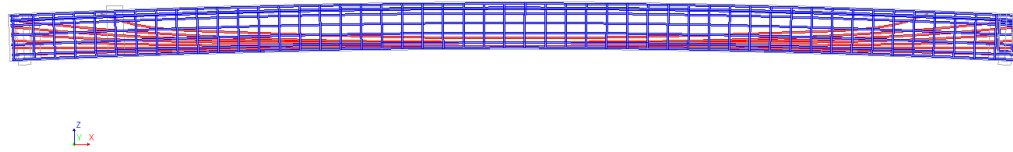
Figure 6.23: Behavior of the 3D model with load at 2250mm

Analysis 1
 Phased, Start-step 4, Load-factor 1.0000
 Displacements TDtZ
 min: -1.12mm max: 13.87mm



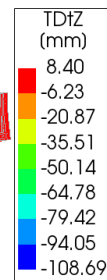
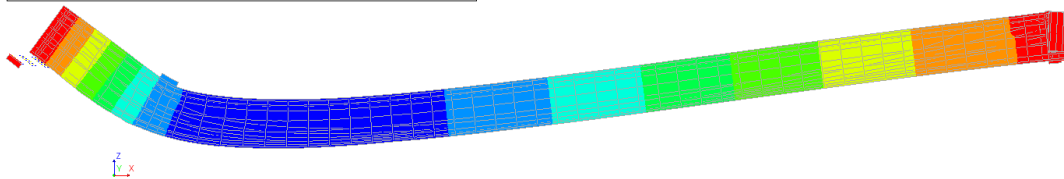
(a) Deformation after prestressing

Analysis 1
 Phased, Start-step 4, Load-factor 1.0000
 Reinforcement Cauchy Total Stresses SXX
 min: -54.14N/mm² max: 861.91N/mm²



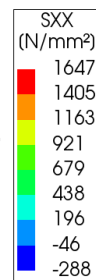
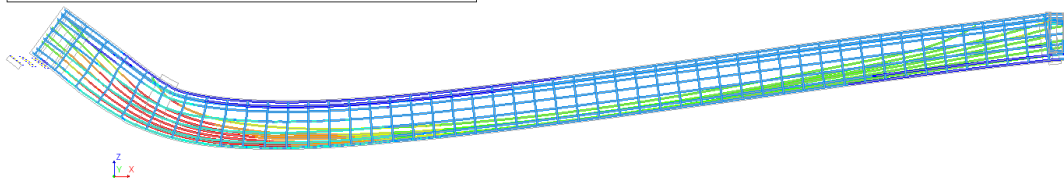
(b) Stress in tendons after prestressing

Analysis 1
 Phased 1, Load-step 91, Load-factor 90.000, Load
 Displacements TDtZ
 min: -109mm max: 8mm



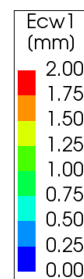
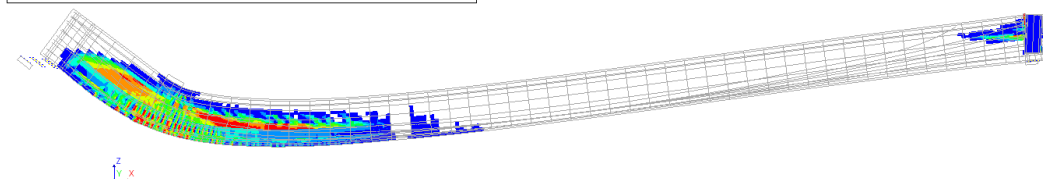
(c) Deformation at final load step

Analysis 1
 Phased 1, Load-step 91, Load-factor 90.000, Load
 Reinforcement Cauchy Total Stresses SXX
 min: -288.28N/mm² max: 1647.23N/mm²



(d) Stress in tendons at final load step

Analysis 1
 Phased 1, Load-step 91, Load-factor 90.000, Load
 Crack-widths Ecw1 layer 1
 min: 0.00mm max: 10.17mm



(e) Crack-widths at final load step

Figure 6.24: Behavior of the 2D shell model with load at 2250mm



(a) Cracks after test 4



(b) Cracks after test 6

Figure 6.25: Cracking behavior of tested beams with load at 2250mm [13]

6.9.2. Load at 4000mm

As for the models with load at 2250mm, a comparison of the 2D, 3D and 2D shell numerical models is made with the experimental data for load at 4000mm (Test 7 in measurement report [13]). For loading at 4000mm on an individual beam, only one experiment is performed and due to safety reasons and lack of clearance below the bridge, the beam was also unloaded during testing as can be seen in figure 6.26. It can also be seen that all the numerical models are in good comparison with each other in terms of peak load (maximum difference of 2.8%) and load-deformation behavior. However, compared to the experiment the peak load is around 21% higher for all the models. All the models are able to capture the behavior of the beam in the linear elastic phase and after flexural cracking, but as soon as the shear crack develops between the point of application of the load and the support, the redistribution of forces is such that the model is not able to capture the subsequent load-deformation behavior.

In terms of maximum deformation (sub-figure (c) of figures 6.27, 6.28 and 6.29), similar behavior is observed as for the load at 2250mm with 2D shell model being the most ductile, however all the models have final deformation within 7.5% of each other. The numerical failure in all these models is also due to crushing of concrete at the point of application of the load. From sub-figure (d) of it can be seen that the prestressing tendons have yielded

but the stresses are still lower than the fracture strength of steel as in the case of the load at 2250mm.

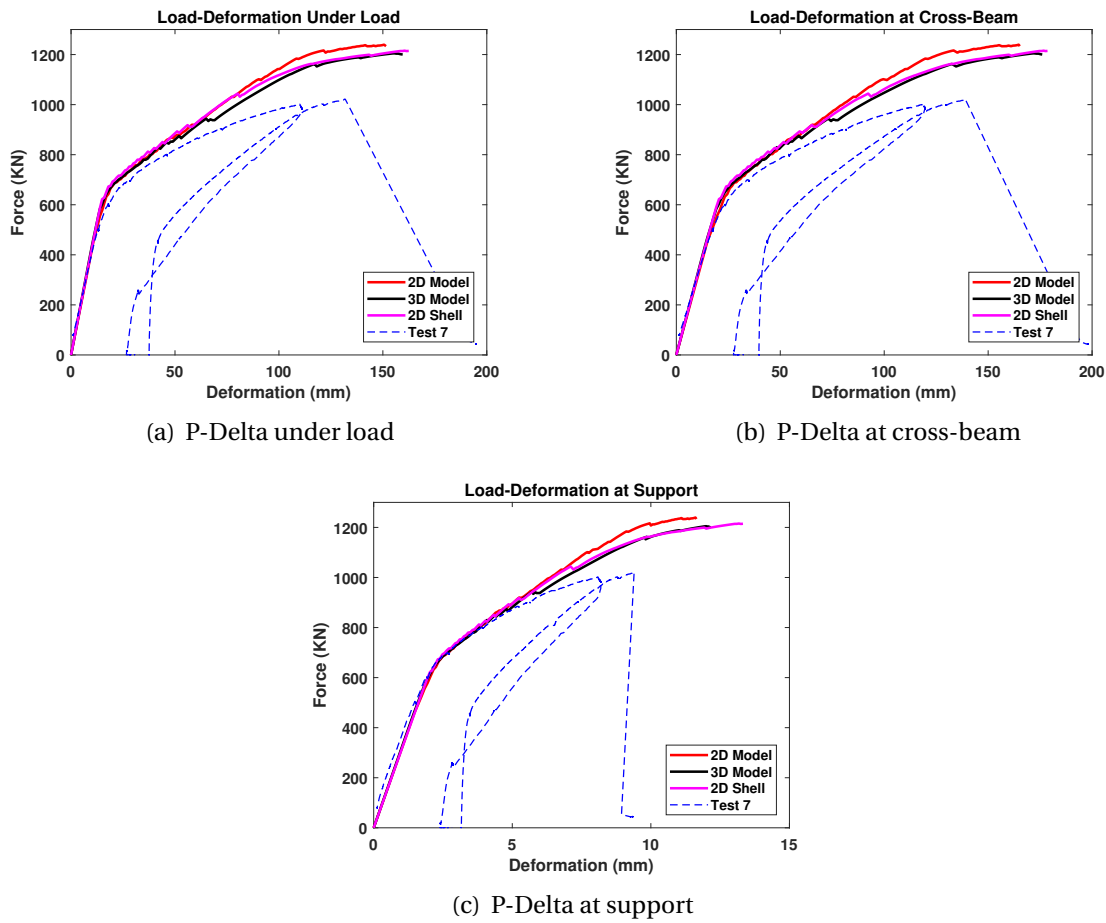


Figure 6.26: Load-deformation comparison of 3D model and experiments for load at 4000mm

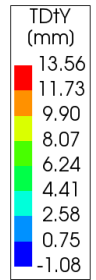
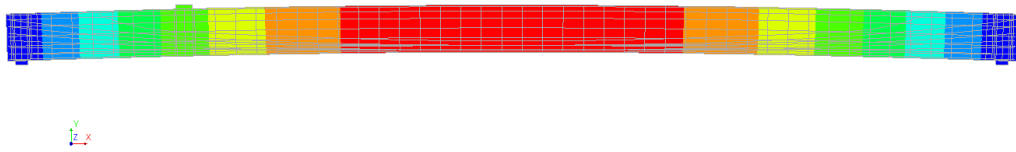
The cracking behavior observed during testing is shown in figure 6.30 which shows a single major crack between the point of application of the load and the supports. As previously discussed, the 3D model is able to capture this behavior in quite good comparison with the experiment but the 2D models show some significant cracking in the other direction as well, reinforcing the previously drawn conclusion that for shear cracking study a 3D model is recommended.

A comparison of experimental and numerical peak load is given in table 6.4 with the computation time required for each analysis.

Table 6.4: Peak load comparison for load at 4000mm

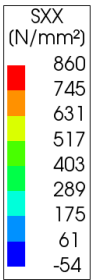
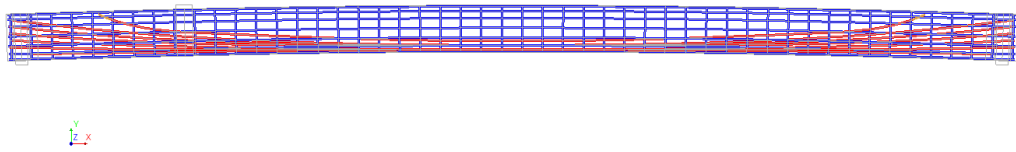
Description	Peak load (KN)	Time (min)
Test 7	1022	-
2D model	1239	73
3D model	1205	1158
2D shell model	1215	121

Analysis 1
 Phased, Start-step 5, Load-factor 1.0000
 Displacements TDtY
 min: -1.08mm max: 13.56mm



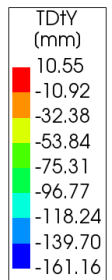
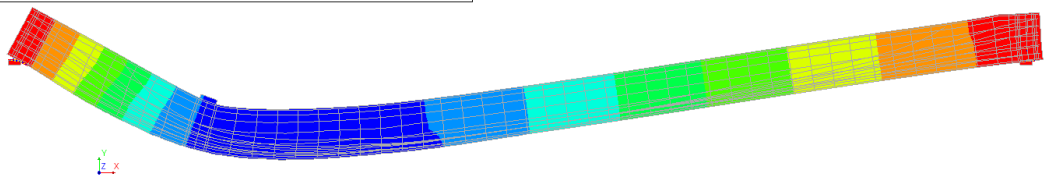
(a) Deformation after prestressing

Analysis 1
 Phased, Start-step 5, Load-factor 1.0000
 Reinforcement Cauchy Total Stresses SXX
 min: -53.63N/mm² max: 859.56N/mm²



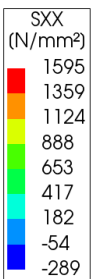
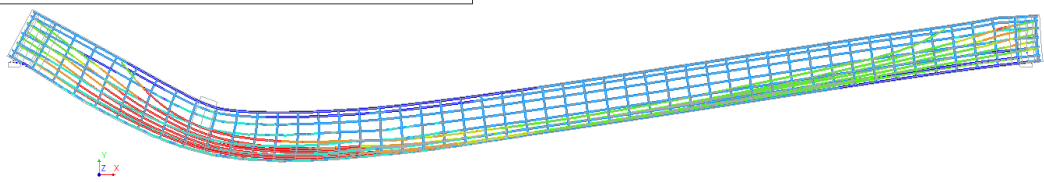
(b) Stress in tendons after prestressing

Analysis 1
 Phased 1, Load-step 151, Load-factor 150.00, Load
 Displacements TDtY
 min: -161.16mm max: 10.55mm



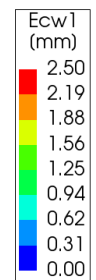
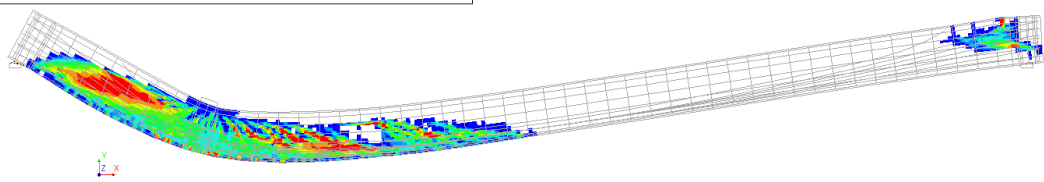
(c) Deformation at final load step

Analysis 1
 Phased 1, Load-step 151, Load-factor 150.00, Load
 Reinforcement Cauchy Total Stresses SXX
 min: -289.48N/mm² max: 1594.88N/mm²



(d) Stress in tendons at final load step

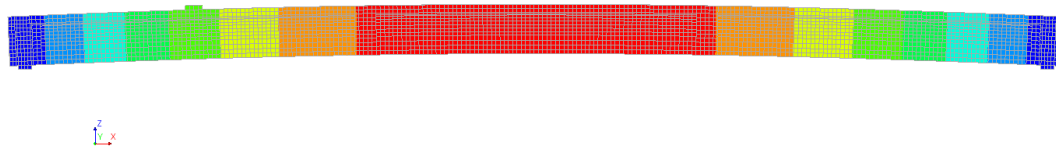
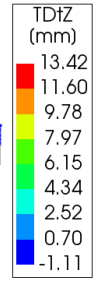
Analysis 1
 Phased 1, Load-step 151, Load-factor 150.00, Load
 Crack-widths Ecw1
 min: 0.00mm max: 7.30mm



(e) Crack-widths at final load step

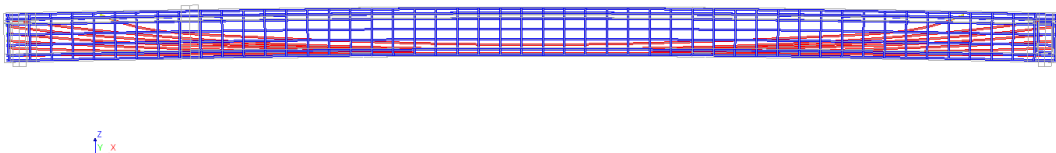
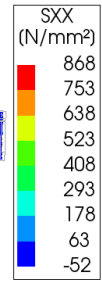
Figure 6.27: Behavior of the 2D model with load at 4000mm

Analysis 1
 Phased, Start-step 4, Load-factor 1.0000
 Displacements TDtZ
 min: -1.11mm max: 13.42mm



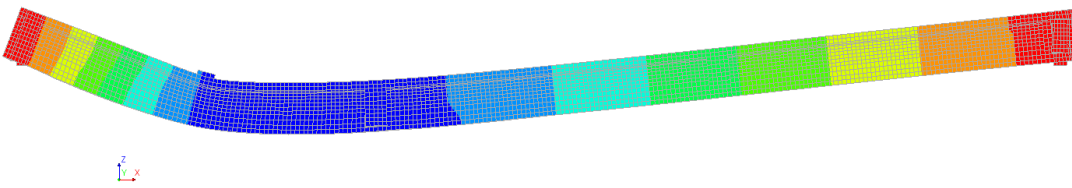
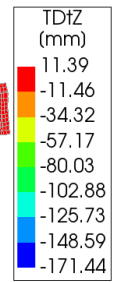
(a) Deformation after prestressing

Analysis 1
 Phased, Start-step 4, Load-factor 1.0000
 Reinforcement Cauchy Total Stresses SXX
 min: -52N/mm² max: 868N/mm²



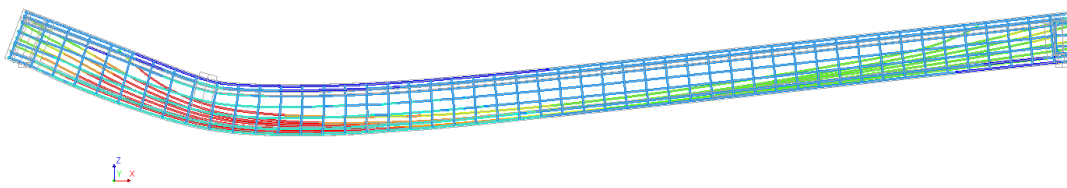
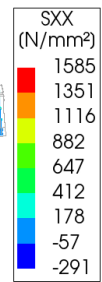
(b) Stress in tendons after prestressing

Analysis 1
 Phased 1, Load-step 160, Load-factor 159.00, Load
 Displacements TDtZ
 min: -171.44mm max: 11.39mm



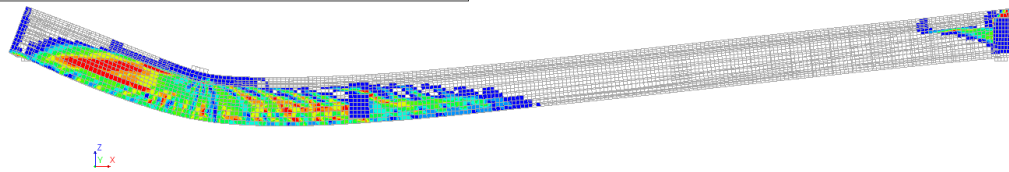
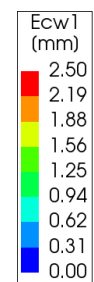
(c) Deformation at final load step

Analysis 1
 Phased 1, Load-step 160, Load-factor 159.00, Load
 Reinforcement Cauchy Total Stresses SXX
 min: -291.44N/mm² max: 1585.49N/mm²



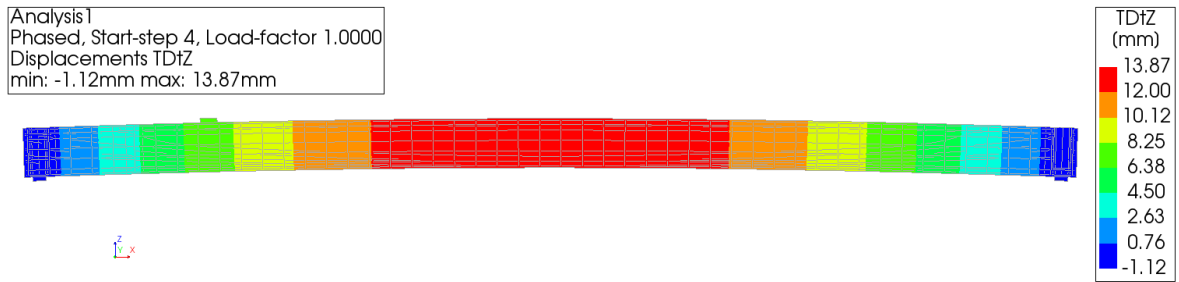
(d) Stress in tendons at final load step

Analysis 1
 Phased 1, Load-step 160, Load-factor 159.00, Load
 Crack-widths Ecw1
 min: 0.00mm max: 14.57mm

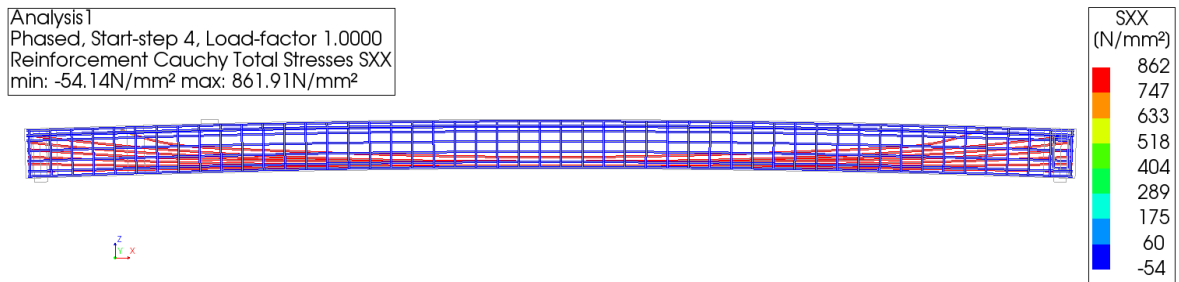


(e) Crack-widths at final load step

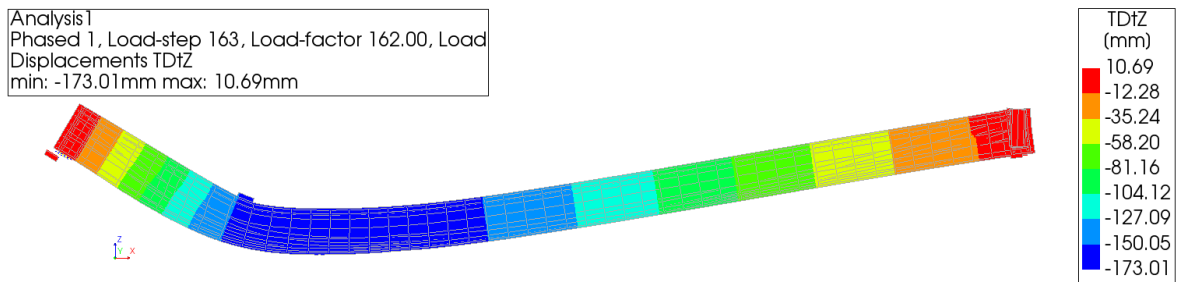
Figure 6.28: Behavior of the 3D model with load at 4000mm



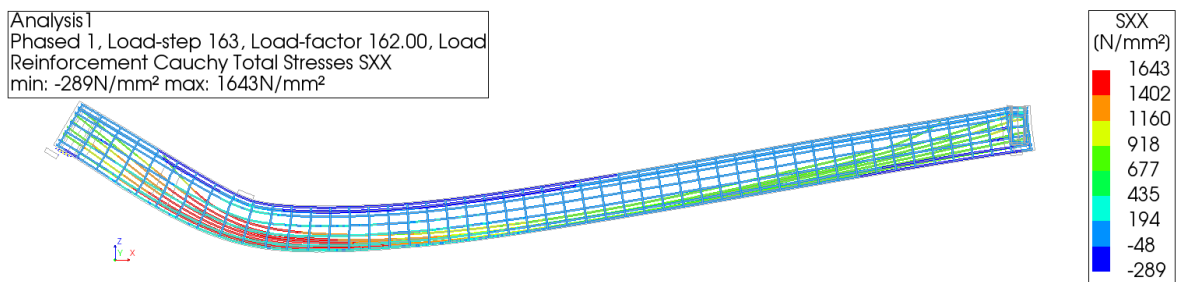
(a) Deformation after prestressing



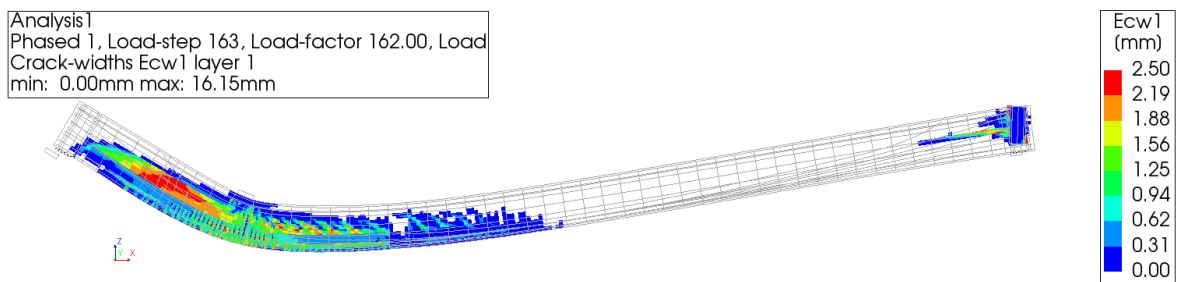
(b) Stress in tendons after prestressing



(c) Deformation at final load step



(d) Stress in tendons at final load step



(e) Crack-widths at final load step

Figure 6.29: Behavior of the 2D shell model with load at 4000mm



Figure 6.30: Cracks after test 7 [13]

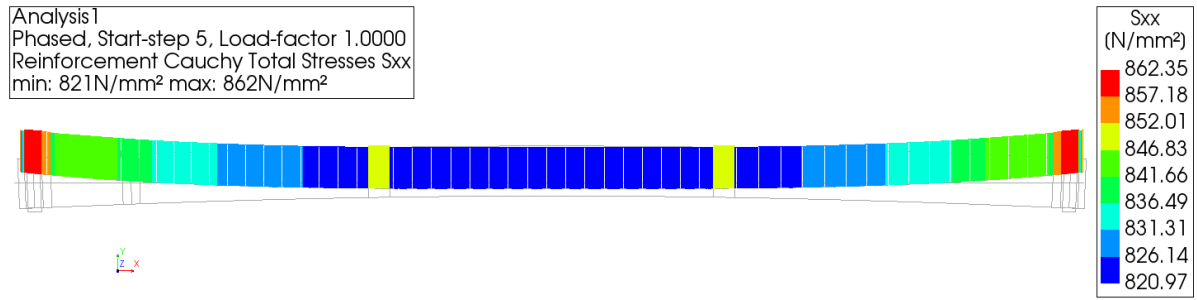
6.10. Refinement using Post-tension Load

In all the discussed models, the prestressing load is applied using the initial bar prestress option in DIANA which assumes a uniform stress along the length of the tendon. As a refinement to the model, the option of post-tension load application is also explored as this allows a more realistic modeling of the stresses in the tendons. The parameters used for the post-tension load application are discussed in section 6.4.

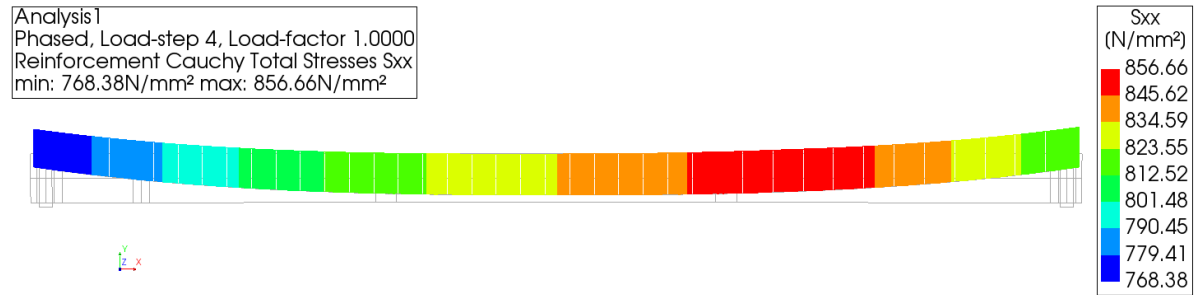
To study the resulting differences in these prestressing load application approaches, comparison has been made between the stress distribution along the length of a single tendon (figure 6.31) and the resulting axial force in the system due to prestressing (figure 6.32). Using the initial bar prestress option results in a relatively uniform stress along the length of the tendon (including the anchor locations) while the post-tension load option results in relatively lower stress at the anchor locations, possibly due to wedge set effects. In general, there is a larger variation in the stresses along the tendon using the post-tension load option because it also considers the losses due to friction and wobble effects.

Comparing the resulting prestressing force in the beam, it can be concluded that the results of using both approaches are quite comparable, as the difference is only 3.5%, but the post-tension load results in a bit higher maximum prestress loss locally (30%) compared to the initial stress option causing a maximum local loss of around 21%.

In light of this discussion, it can be concluded that the use of initial bar prestress option in DIANA gives similar results with the post-tension load option, at least when the tendons are modeled as embedded reinforcements in the mother elements.

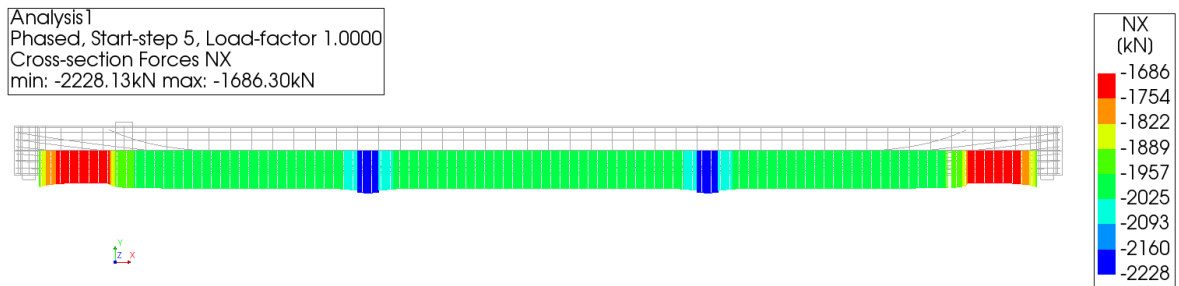


(a) Stress distribution in tendon using initial bar prestress

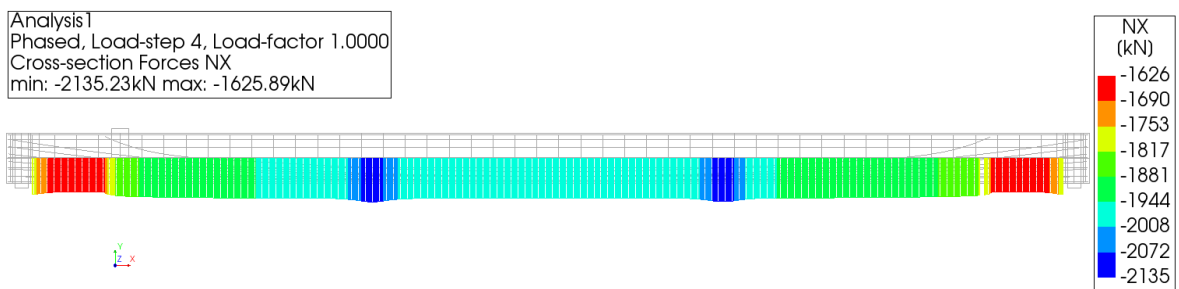


(b) Stress distribution in tendon using post-tension load

Figure 6.31: Comparison for stress distribution in a tendon



(a) Axial prestressing force using initial bar prestress



(b) Axial prestressing force using post-tension load

Figure 6.32: Comparison for axial prestressing force in the system

7

Comparison of Disjointed Bridge and Equivalent Beam Model

This chapter focuses on smart modeling techniques that can be used to simulate the behavior of structural elements as though they were part of a bigger structural system. First the feasibility of modeling the behavior of a beam by only modeling the distance between the cross-beams (loaded sub-span) is analyzed and then efforts are made to model an individual beam that behaves as though it is connected to the bridge through cross-beams.

Note: The distribution of the load in transverse direction has not been taken into account so the observed increase in load bearing capacity is only because of the longitudinal arch action in the beam and not the transverse compressive membrane action in the deck slab.

7.1. Equivalent Beam Model

The equivalent beam model is developed with the idea that it represents the beam as though it is connected to the bridge through cross-beams. The first aim of the equivalent beam model is to analyze if it is possible to model the behavior of the entire beam by modeling only the loaded sub-span i.e. the distance between the cross-beams. For this part of the project, the verified numerical model of the Vechtbrug beam has been used with load acting at mid-span of the beam to study a more symmetric loading scenario.

To model the beam as though it is connected to the bridge system, all the cross-beams are modeled till the neighboring beams and restraints are applied to model the resistance offered by the connection of cross-beam with the rest of the bridge. The reinforcement and prestressing tendons of the cross-beams are also modeled and the transverse prestressing is applied as an external load, as described earlier for end-beam of Vechtbrug in section 6.4. The geometry and reinforcement layout of the equivalent beam model can be seen in figures 7.1 and 7.2 respectively. The behavior of the intermediate cross-beam is modeled in the same manner as for the end-beam in Vechtbrug beam model (A detailed account of the adopted methodology can be found in section 6.5). For the vertical stiffness, calibration has been made relative to the disjointed bridge model (described later in the chapter), ignoring the distribution of the load in transverse direction.

To model the cross-beams as though they are connected to the bridge system, the use of tying is made in global X and Y direction and all the deformations are tied to one of the corners of the cross-beam as described in section 6.5. Whereas, in vertical (global Z) direction, a face boundary interface has been used to model the vertical stiffness offered by the connection of the cross-beams with the bridge. A pictorial representation of these modifications can be seen in figure 7.3.

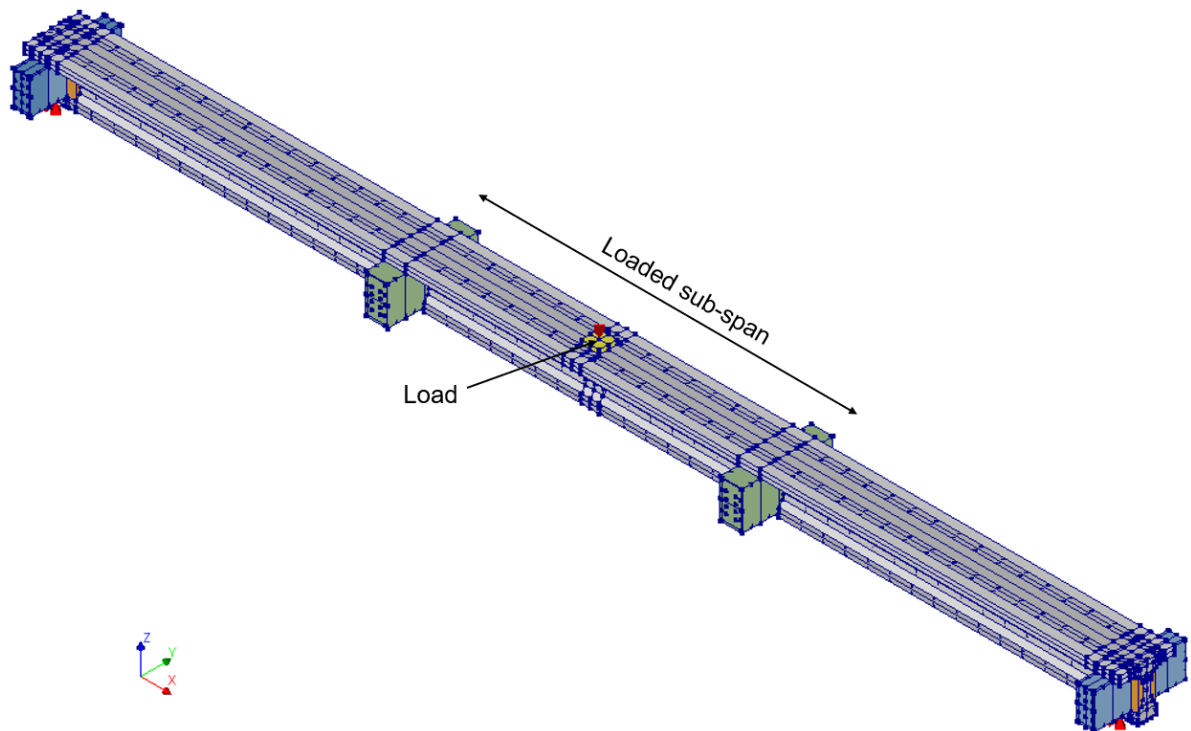


Figure 7.1: Geometry of the equivalent beam model

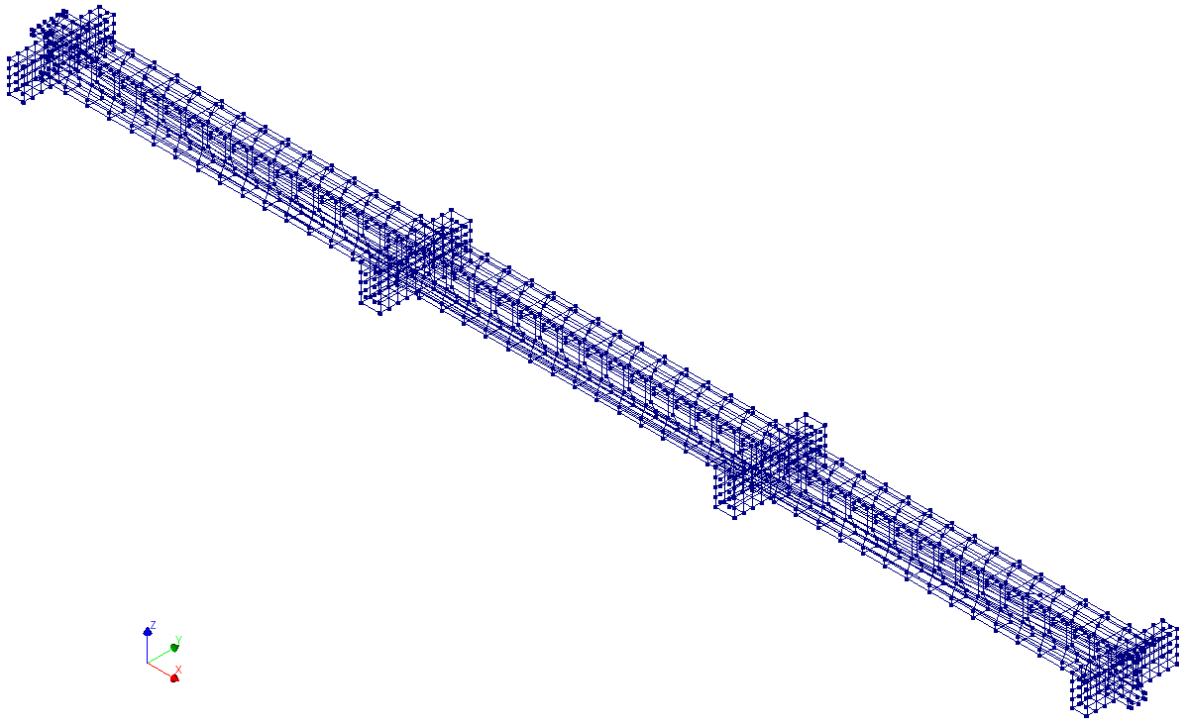
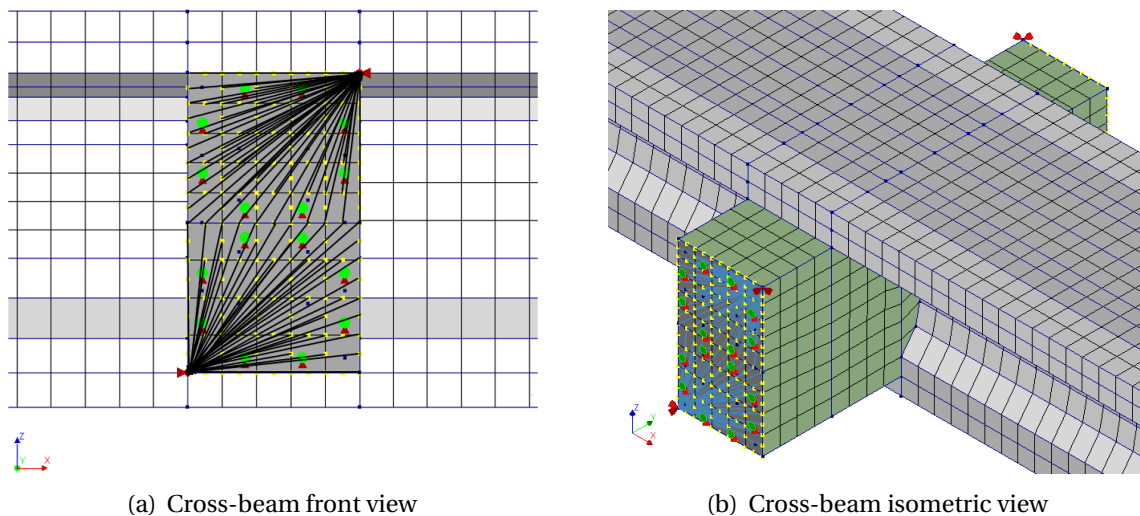


Figure 7.2: Reinforcement of the equivalent beam model



(a) Cross-beam front view

(b) Cross-beam isometric view

Figure 7.3: Intermediate cross-beam boundary conditions

All the other properties of the equivalent beam model are the same as described in chapter 6 for the Vechtbrug beam model except the load steps in the analysis procedure. The vertical deformation load step is reduced to $0.5(100)$ with a specified 1mm imposed deformation because the total deformation of the equivalent beam model is much lower than the Vechtbrug beam models.

The equivalent beam model can be simplified by modeling only the distance between the intermediate cross-beams to simulate the full beam behavior, this would help develop a much cheaper numerical model. The motivation for this idea comes from a linear elastic

analysis performed by Ensink [7] on the full bridge model with load at 4000mm from the supports and the results (figure 7.4) show that almost all of the applied shear and bending moment is resisted by the sub-span between the cross-beams and the rest of the beam seems to have very minor contribution in load resistance. Similar conclusion can also be drawn looking at the principal stresses as there is almost no change in the stresses with application of the load beyond the loaded sub-span.

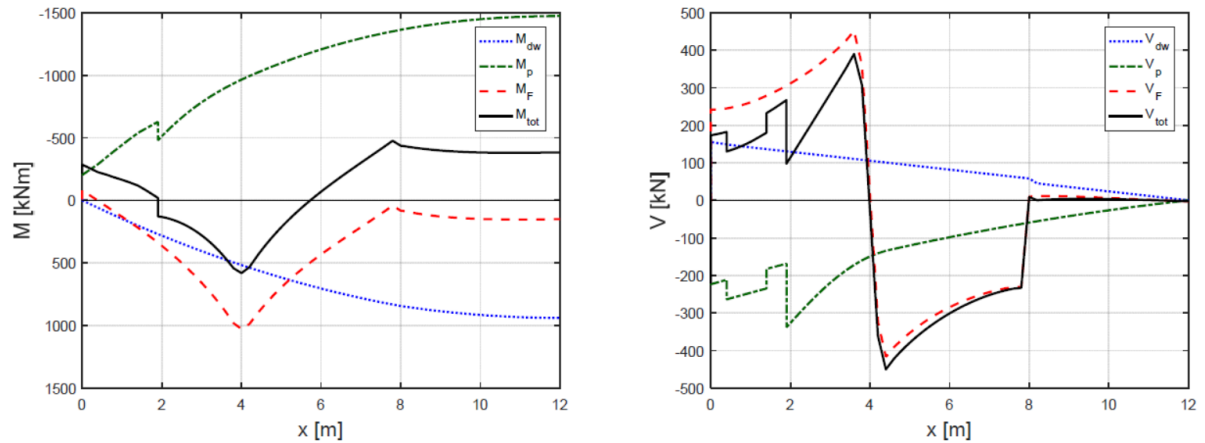
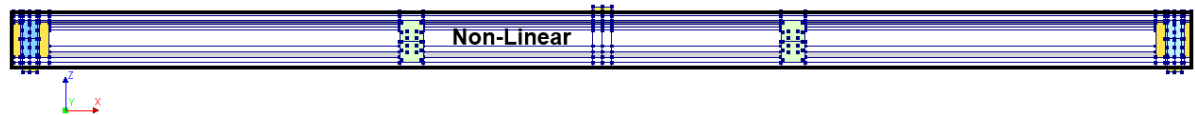
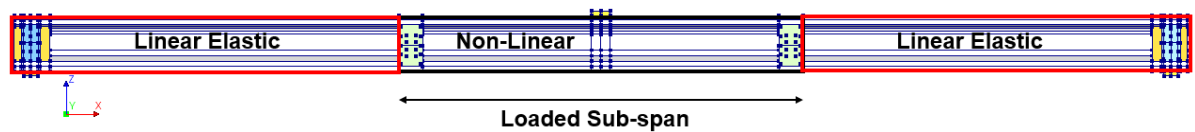


Figure 7.4: Shear force and moment distribution in linear elastic bridge system [7]

Developing on this idea, the equivalent beam model is modified by assigning linear elastic properties to the concrete outside the region of intermediate cross-beams as shown in sub-figure (b) of figure 7.5. This model is referred to as EQ-CB model and the full non-linear equivalent beam model is called EQ-NL model.



(a) EQ-NL model (Complete beam model is non-linear)



(b) EQ-CB model (Only the distance between the cross-beam in non-linear)

Figure 7.5: Description of EQ-NL and EQ-CB model

The behavior of the two models has been compared in terms of load-deformation at the point of application of the load and at the intermediate cross-beam. The load-horizontal deformation behavior at the cross-beam level and the development of membrane force between the cross-beams with increasing load is also compared. The results of both the analysis are shown in figure 7.6. It must be noted that for the membrane force, composed line option has been used with selected elements and only the forces in concrete elements are considered for post-processing i.e. the stresses in reinforcing and prestressing steel are ignored.

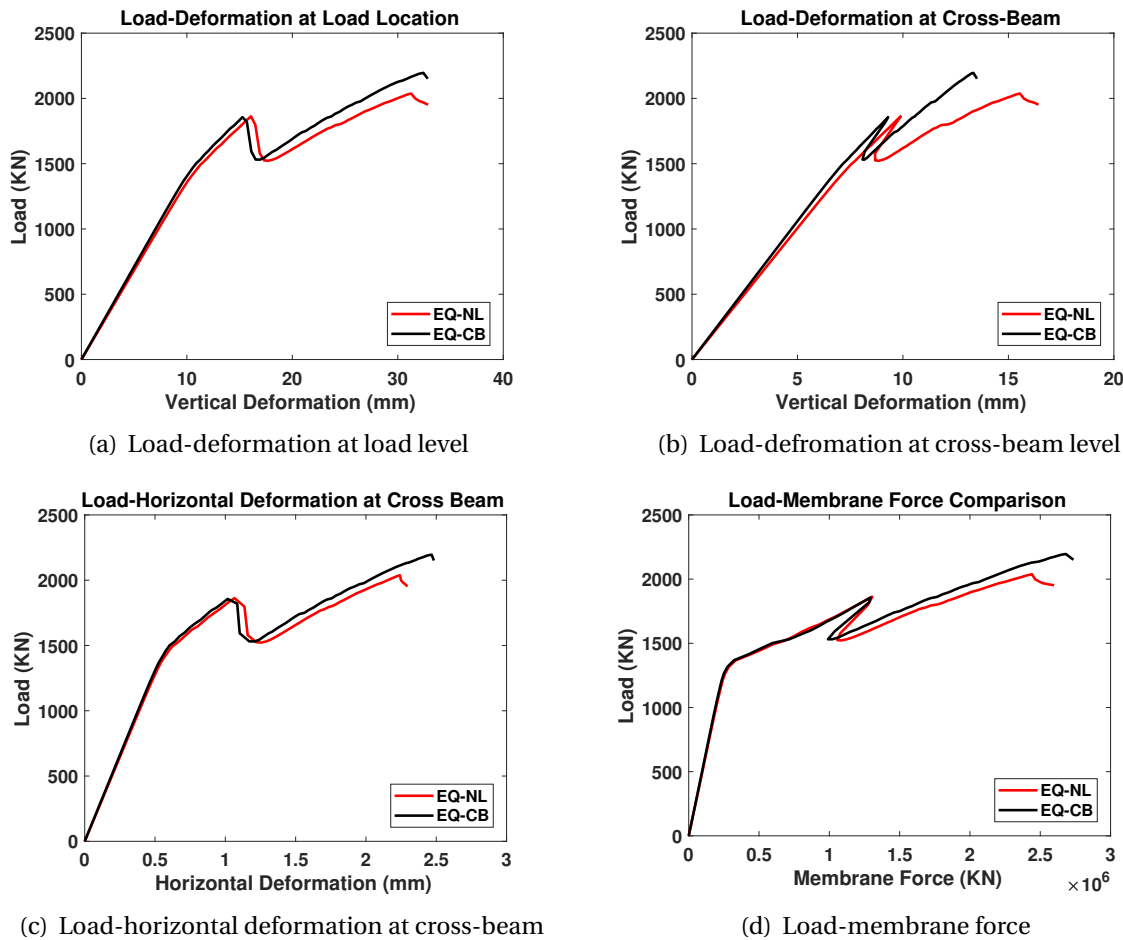


Figure 7.6: Comparison of EQ-NL and EQ-CB model

Following the results shown in figure 7.6, it can be said that the behavior of the complete beam can indeed be simulated by modeling only the loaded sub-span between the two cross-beams. The ultimate capacity of the EQ-CB model is 7% higher than the capacity of EQ-NL model but the difference in the load at the shear crack development is only 2.25%. Both the beams also show very similar arching behavior as the difference in the membrane force is only 1.6% at the load level when shear crack develops. Comparing the sub-figure (a-c) of figure 7.6, it can be seen that the EQ-NL model is slightly less stiff than the EQ-CB model. This difference is especially visible after the end of the linear elastic phase and can be possibly explained by the cracking adjacent to the cross-beam visible in sub-figure (a) of figure 7.7. This cracking is prevented in EQ-CB model due to assignment of linear elastic properties beyond the loaded sub-span resulting in a slightly higher stiffness. In general, both the beams show quite similar cracking behavior as seen in figure 7.7.

Note that the cracking near the end-beams in EQ-NL model is due to the localization caused by prestressing load in the tendons and not as a result of the applied deformation. Therefore, these cracked elements can be ignored in this comparison.

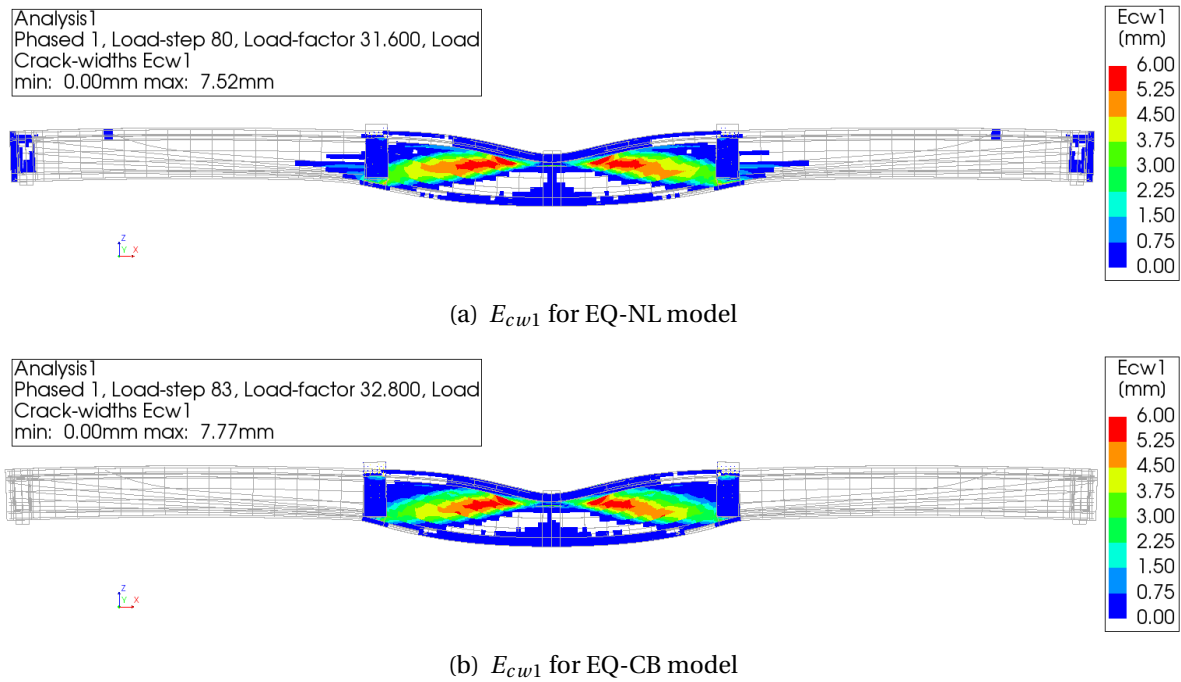


Figure 7.7: Comparison of crack pattern for EQ-NL and EQ-CB model

The computation time required for both, EQ-NL and EQ-CB model, is also compared and shown in table 7.1. Modeling only the loaded sub-span of the beam to simulate the full beam behavior appears to be a very attractive approach as with little (2.5%) loss in accuracy the computation time is reduced by 67%.

Table 7.1: Computation time of EQ-NL and EQ-CB model

Model	Computation Time (min)
EQ-NL	1032
EQ-CB	342

7.2. Disjointed Bridge Model

The full Vechtbrug model is developed and verified using the experimental results (Tests 1-3 as mentioned in chapter 5) by Ensink as part of his PhD study at Delft University of Technology. It consist of 15 T-beams connected to each other through 4 cross-beams at a distance of 8m from each other. The cross-beams and bridge deck are also transversely prestressed using QP170 tendons.

The validated full bridge numerical model is then adapted to simulate the beam behavior as though it is connected to the bridge through cross-beams only i.e. the slab of the loaded sub-span is disjointed using the no connection interface option in DIANA to prevent the distribution of the load in transverse direction - this adapted model is referred to as disjointed bridge model. Disconnecting the slab ensures that the observed enhancement in capacity of the beam is only because of the arch action in the loaded sub-span as the compressive membrane action is completely prevented. This has been done because the scope of this MSc. thesis is limited to the arching behavior of a single beam in longitu-

dinal direction only.

An illustration of the disjointed bridge model and the mesh used can be seen in figure 7.8 and figure 7.9 respectively. The edges of the slab assigned the no connection interface are marked using the dashed red line in figure 7.8. In section 7.1 it has been observed that modeling the loaded sub-span only results in almost the same behavior as the full non-linear beam model with significant reduction in computation time. Using this idea for the disjointed bridge model, only the light gray part around the load in figure 7.8 and light gray finely meshed part in figure 7.9 is modeled as non-linear concrete and the rest of the bridge is assigned linear elastic properties. In transverse direction only three beams are non-linear but as the slab between the beams is disconnected, any distribution of load in transverse direction is prevented. This justifies the use of limited numbers of non-linear beams in transverse direction.

The cross-beams are also assigned non-linear concrete properties so their contribution in the arching effect can be modeled realistically. The mesh size of the non-linear part is assigned to be 100mm (equal to the mesh size of equivalent beam model) and for the linear elastic part a mesh size of 300mm is used. In the disjointed bridge model, the transverse prestressing is applied as external load, similar to the equivalent beam model and the use of composed line elements has been made with selected elements in DIANA to obtain the results of membrane force and bending moments in the central sub-span of the loaded beam. For this comparison the concrete elements, longitudinal bars and prestressing tendons are all contributing to the results of composed line.

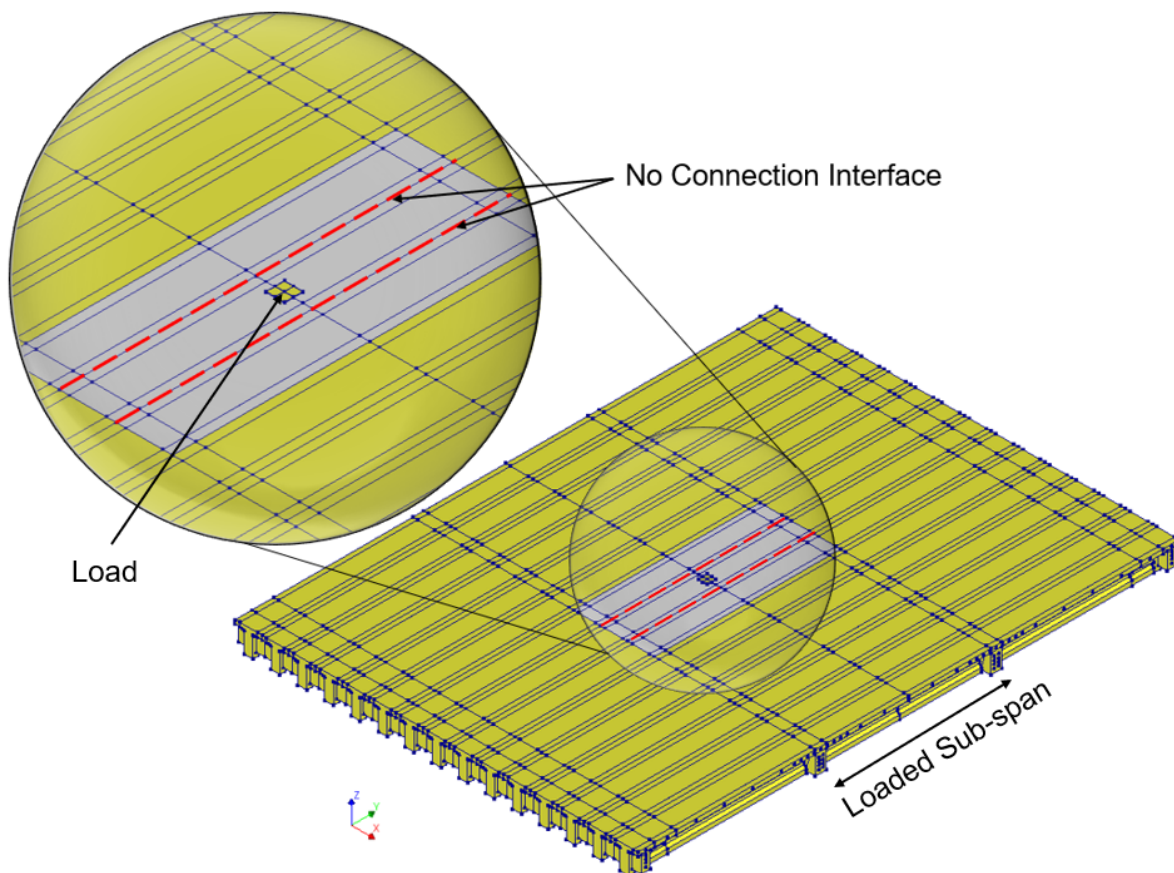


Figure 7.8: Disjointed bridge model with disconnected slab (Light gray part is non-linear)

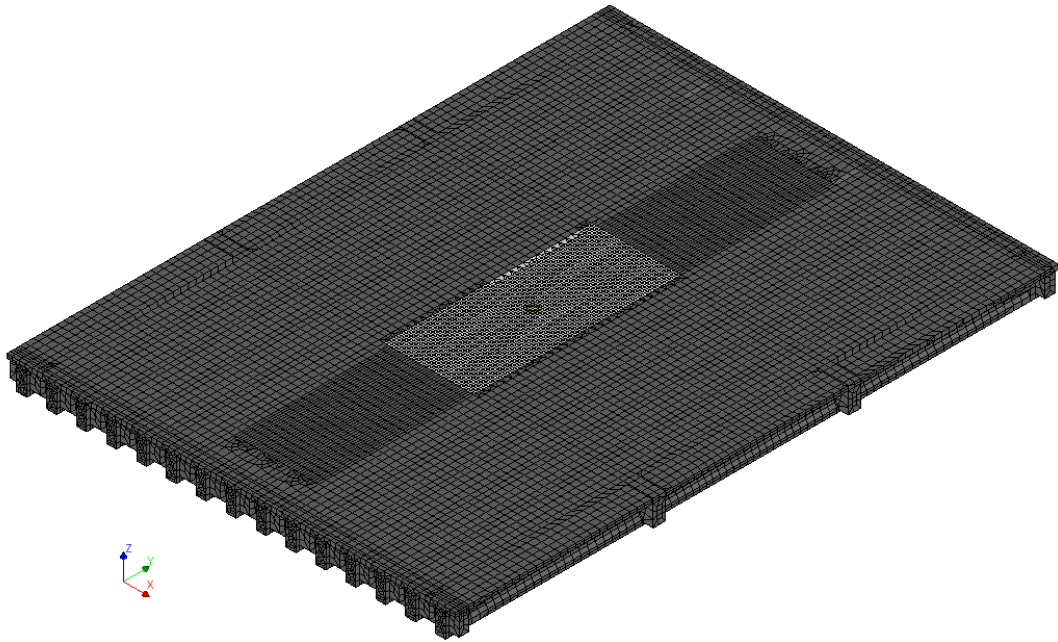


Figure 7.9: Disjointed bridge model mesh (Light gray part is non-linear)

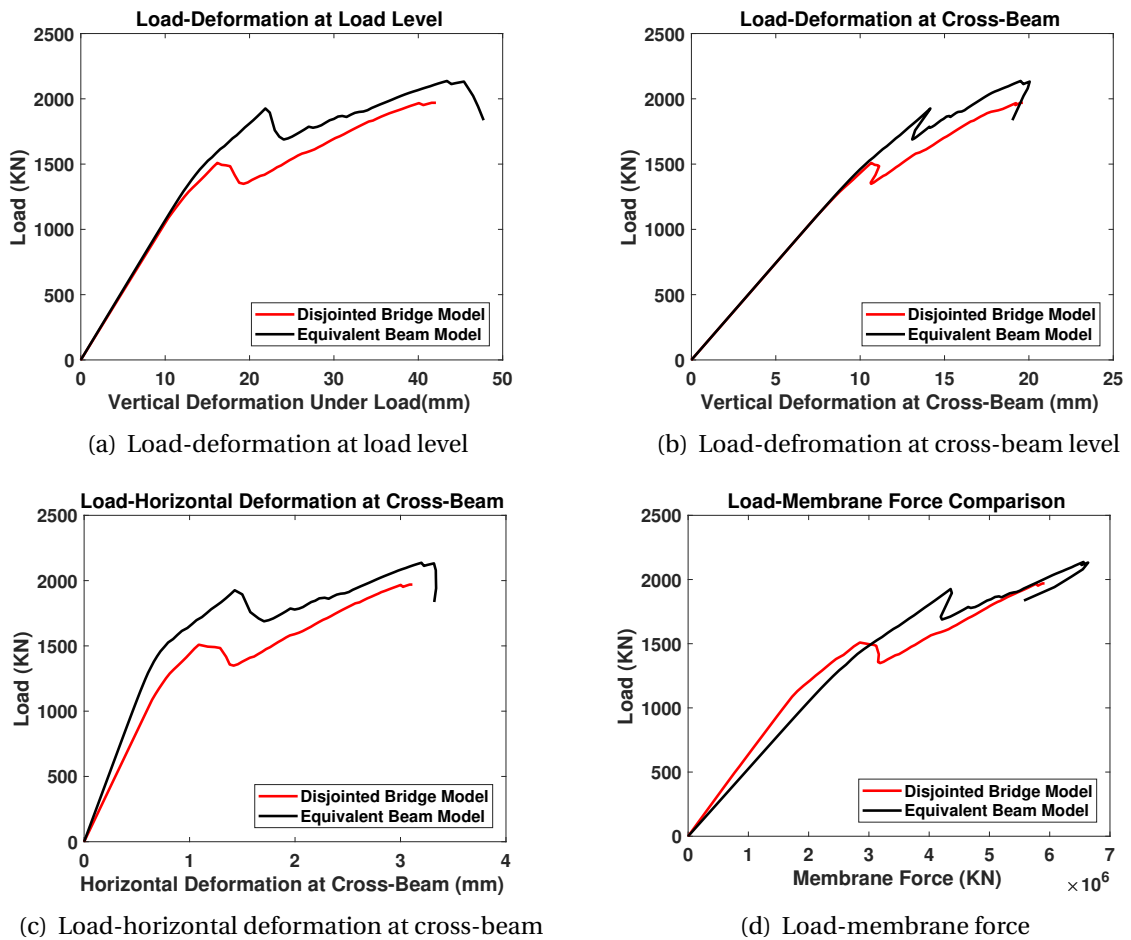
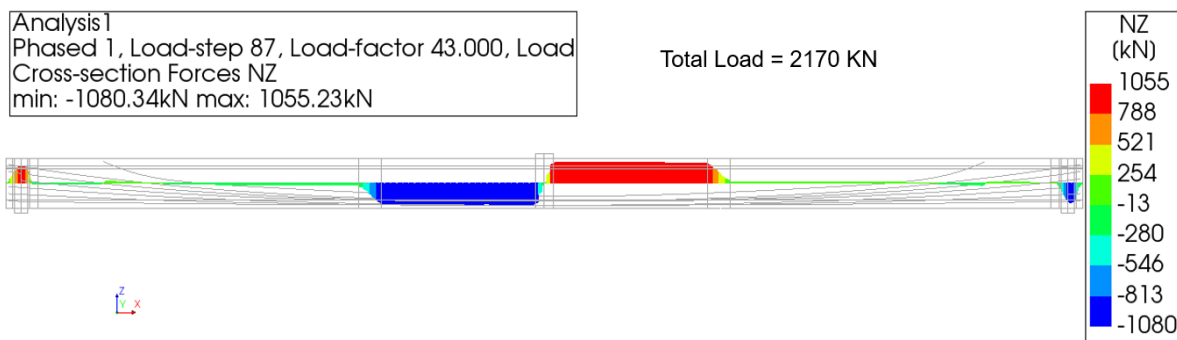


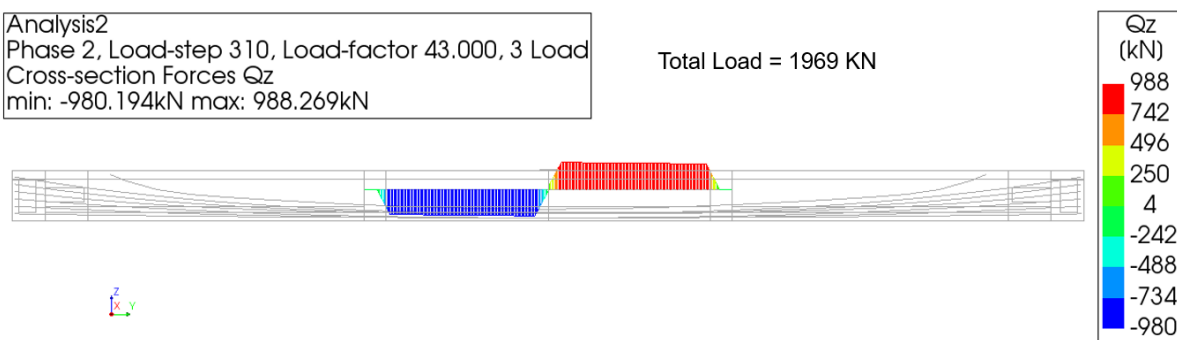
Figure 7.10: Comparison of disjointed bridge model and equivalent beam model

The equivalent beam model used for comparison with the disjointed bridge model is similar to the EQ-CB model as described in section 7.1 i.e. only the concrete of the loaded sub-span is non-linear and the rest of the beam is assigned linear elastic properties. This is also consistent with the disjointed bridge model as only the loaded sub-span is modeled as non-linear. The vertical stiffness of the equivalent beam model is calibrated as per the disjointed bridge model and all other material parameters and inputs are the same as discussed in section 7.1. The convergence behavior of all the numerical models discussed in this chapter can be seen in Appendix B.

The vertical deformation of the equivalent beam model and the disjointed bridge model is compared at the point of application of the load and at the level of cross-beam in sub-figures (a) and (b) of figure 7.10 respectively. It can be seen that the initial stiffness of both the models is in good comparison because of the calibration of the equivalent beam model for vertical stiffness of the interface. However, the disjointed bridge model shows a 16% lower capacity for shear crack development when compared to the equivalent beam model. This might be explained using the results shown in sub-figure (c) and (d) of figure 7.10 where it can be seen that the applied boundary conditions cause the equivalent beam model to be stiffer against the horizontal stretch - the difference in the initial slope of the load-horizontal deformation plot is 22%. This difference in the stiffness of cross-beam causes a higher membrane force in the equivalent beam model as the load is applied (sub-figure (d) of figure 7.10), therefore a more pronounced arching effect is observed resulting in the increased capacity of the equivalent beam model.



(a) Shear force distribution in equivalent beam model



(b) Shear force distribution in disjointed bridge model

Figure 7.11: Comparison of shear force distribution in equivalent beam and disjointed bridge model

To further compare the behavior of the loaded beam in disjointed bridge model and

the equivalent beam model, the shear force distribution along the length of the beam is compared in figure 7.11. It can be seen that almost all the load is resisted by the loaded sub-span in both the models, reinforcing the previously drawn conclusion that most of the load in the beam is resisted by the loaded sub-span. The cracking behavior of both the models is also very similar as can be seen in figure 7.12 and sub-figure (b) of figure 7.7.

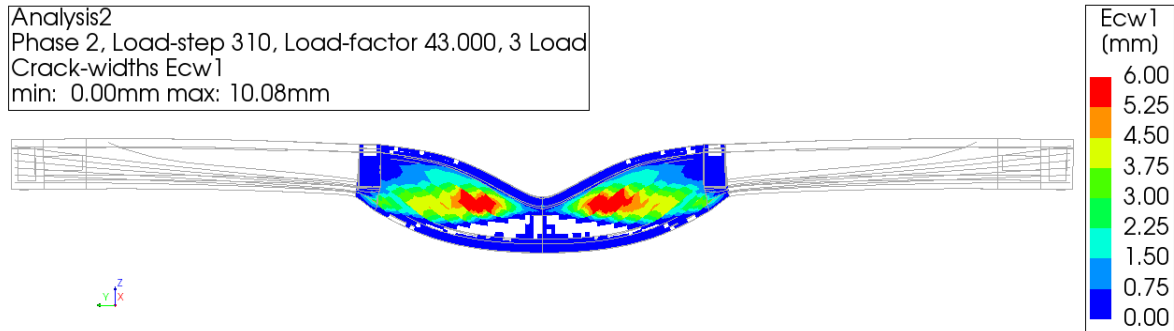


Figure 7.12: Cracks in the loaded sub-span of disjointed bridge model

The adapted CUR model for T-beams with point load is also used to analytically determine the arching capacity of loaded sub-span. For the application of the analytical model, the web of the Vechtbrug beam is modified as shown in figure 7.13 so that both the sections have same cross-sectional area of the web. Note that for this calculation the equivalent width of slab and beam concrete is used as discussed in subsection 6.2.1.

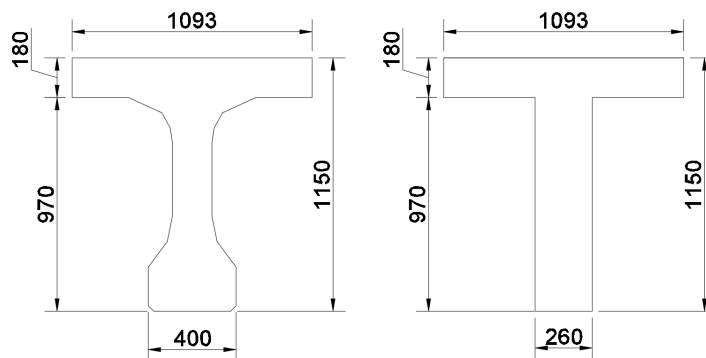


Figure 7.13: Vechtbrug beam and transformed T-section for CUR method application

Table 7.2: Parameters used to calculate analytical arching capacity of the loaded sub-span

Property	Value	Unit
Width of top flange (b_f)	1093	mm
Height of top flange (h_f)	180	mm
Width of web (b_w)	260	mm
Height of web (h_w)	970	mm
Compressive strength (f_c)	90	MPa
End stiffness (k)	1.18×10^7	N/mm
Length of beam (L_x)	8000	mm
Load location	4000	mm

The stiffness of lateral-restraint is calculated using the same procedure as discussed in section 6.5 and all the parameters used for analytical calculation are listed in table 7.2.

The adapted CUR model predicts the capacity to be 3980 KN which is around 80% higher than the numerical capacity of 2170KN obtained for the equivalent beam model. The difference in the analytical and numerical capacity is possibly because of the relatively thin web (180mm) causing the strut failure to be governing instead of compression of concrete at the point of application of the load, which is one of the assumptions of the analytical model. Furthermore, as the shear failure is governed by the tensile strength of concrete and the relative increase in tensile strength is much lower with increasing compressive strength, the high compressive strength of 90 MPa might also be a factor in this difference. As concluded in the first part of the report, the use of the studied approximate analytical model should only be made if the crushing failure of concrete is expected as it does not take into account any other failure mechanisms. It must also be noted that the analytical model assumes the stiffness of lateral restraint to be constant while in the numerical model this stiffness is significantly reduced due to cracking of the intermediate cross-beams. The reduction of the lateral restraint might also be a significant factor causing the difference in analytically and numerically calculated arching capacity of the loaded sub-span.

In light of the above discussion it can be concluded that, if the distribution of the load is prevented in the transverse direction, a single beam model with fully restrained edge faces of the cross-beam overestimates the influence of arching phenomenon on the load carrying capacity of the loaded sub-span by 16%.

Conclusions (Part-II)

1. All the modeling approaches (2D, 2.5D and 3D) show quite similar results in terms of peak load (within 10%) and load-deformation response of the prestressed concrete beam. However, the 2D models require much less computational time compared to the 2D shell and 3D models. Although the load-deformation response is very similar, only the 3D model is able to accurately predict the cracking pattern of the prestressed concrete beam.
2. The peak loads predicted by the numerical models are quite comparable to the experimental results for the beam loaded at 2250mm (within 7%) but for the load at 4000mm the predicted peak load is higher by 21%. In the latter, the difference is possibly because the numerical model is not able to simulate the distribution of stresses after the shear crack development as the numerical load-deformation plots deviate from the experimental plot once the shear crack develops.
3. The use of initial bar prestress and post-tensioning load options in DIANA result in quite similar axial forces in the system (within 3.5%) when the tendons are modeled as embedded reinforcements. However, the maximum local losses are around 9% higher when post-tension load option is used because of the friction, wobble and wedge set effects.
4. When the cross-beams are fully restrained in the longitudinal direction of the beam, only the loaded sub-span can be used to model the behavior of the full beam with an error of only 7% in the ultimate load carrying capacity and requires only 33% of the computational time for a full beam analysis.
5. Fully restraining the cross-beams in longitudinal direction of the beam overestimates the arching phenomenon in the loaded sub-span as it limits the stretch of the system and causes higher membrane forces to develop. This results in an increase of 19% in the load for shear crack development when compared to the disjointed bridge model.
6. The adapted analytical model for T-beams with point loads is not able to estimate the arching capacity of the loaded sub-span of the beam due to the failure of the strut. This failure mode is not accounted for in the assumptions of the analytical model as it assumes a crushing failure of concrete at mid-span or at supports.

Recommendations

Developing on the work done in this project, a few recommendations are made for future researchers as an idea to explore further in understanding the mechanisms responsible for the enhancement of load carrying capacity of concrete bridges.

1. The results of this project show that there is a significant increase in the load-carrying capacity of concrete beams due to arching action in T-beam bridges with cast-in-between decks, a phenomenon that has not been taken into account previously. However as a starting step, arching has been studied separately by preventing the distribution of the load in transverse direction in the bridge system. As a step further in understanding the mechanisms responsible for the hidden capacities of such bridges it is recommended to study the longitudinal arch action in beams in combination with the transverse compressive membrane action (CMA) in deck slabs. Studies to understand the relative contribution of both the mechanisms in enhancing the capacity of bridges and the geometric conditions required to guarantee the existence of both the mechanisms would greatly help in explaining the differences in expected and observed capacities of bridge systems.

2. The main focus of this project has been to study the influence of arch action on the bending capacity of concrete beams. A detailed study focusing on the effect of membrane force on different shear failure mechanisms would also be quite useful in understanding the effects of arching that can be conservatively used by engineers in practice while analyzing existing structures, if not in the design. As a motivation for this the trial beam (described in chapter 1) has been used with load placed at 2250mm from the support and comparison has been made between the load at which the shear crack develops for a simply supported and a fully restrained beam as shown in figure R.1. This proves that the membrane force also has a significant effect on the shear capacity of concrete beams and hence is vital to investigate.

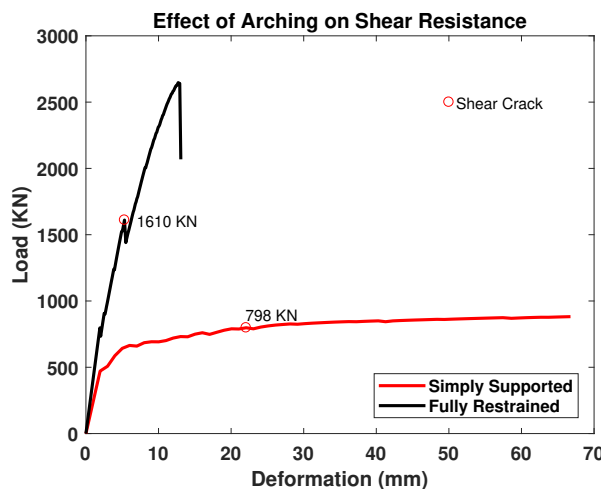


Figure R.1: Effect of arching on shear capacity of prestressed concrete beams

3. This is the first study in efforts to quantify the arch action in eccentrically loaded beam like concrete members hence the approximate analytical model developed in this study is only able to predict the arching capacity of beams if the compression failure of concrete is expected. There are some accounts for the effect of membrane action on punching shear capacities in bridge deck slabs but methods have not been developed to study the effect of arching on shear-tension type failures which are more common in beams. Studying this effect as mentioned earlier and incorporating it in analytical tools would be a significant step further in being able to practically quantify and use the arching phenomenon.

4. In literature, the compressive strength of concrete is also reported to have significant effect on the arching capacity of concrete members which has not been included in this study. The applicability of the adopted method for varying compressive strength of concrete would also help validate the analytical model for further use.

A

Appendix A

Convergence behavior of Vechtbrug beam models used for comparison with the experimental results.

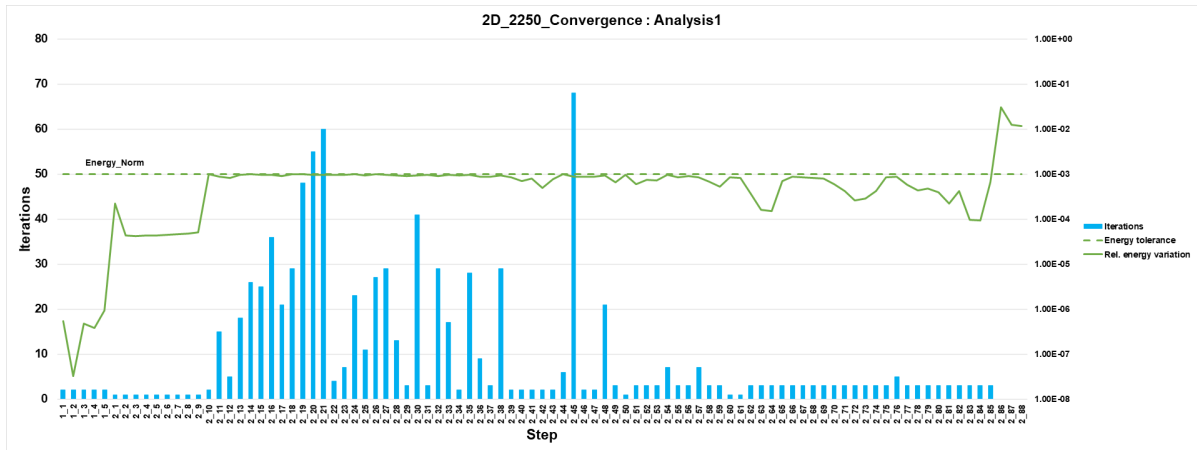


Figure A.1: Convergence behavior of 2D model with load at 2250mm from the support

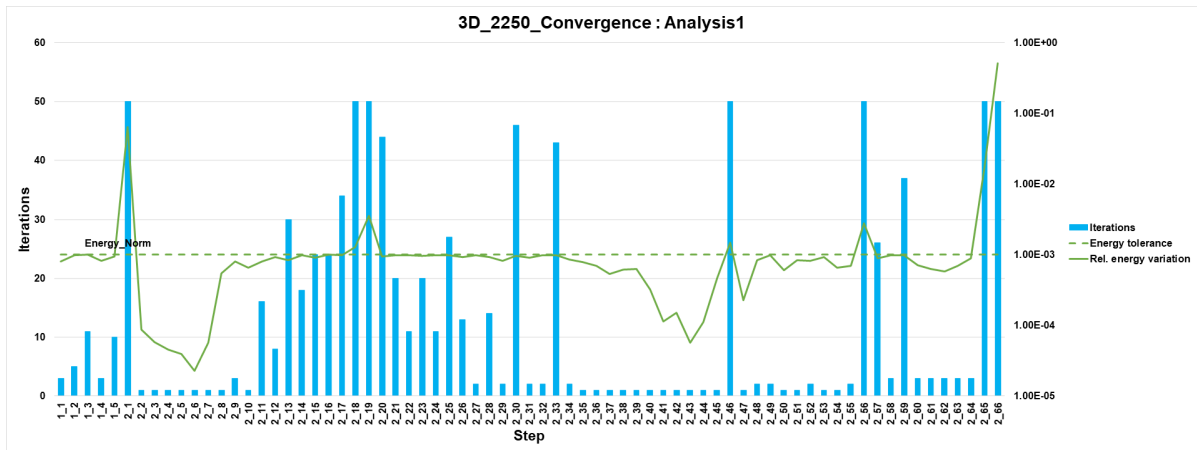


Figure A.2: Convergence behavior of 3D model with load at 2250mm from the support

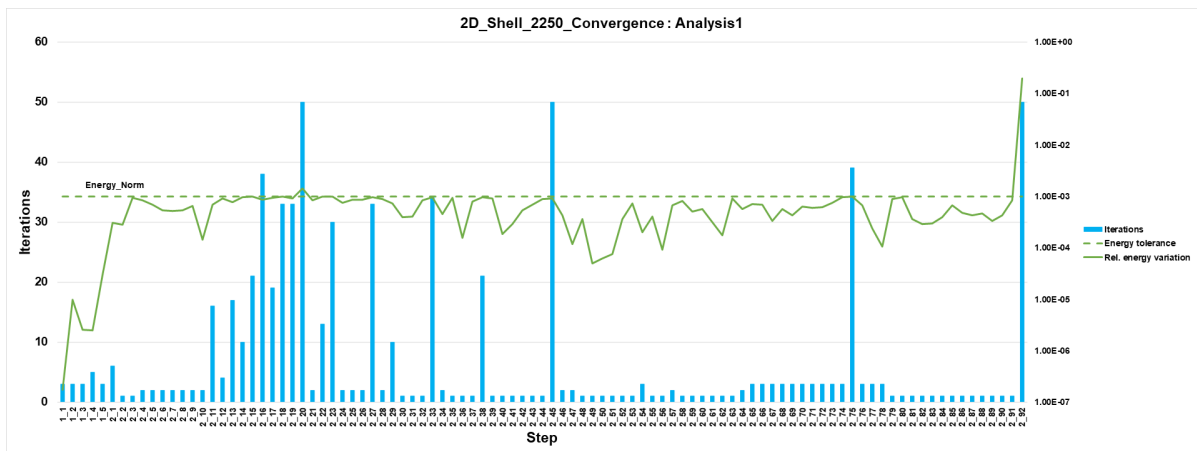


Figure A.3: Convergence behavior of 2D shell model with load at 2250mm from the support

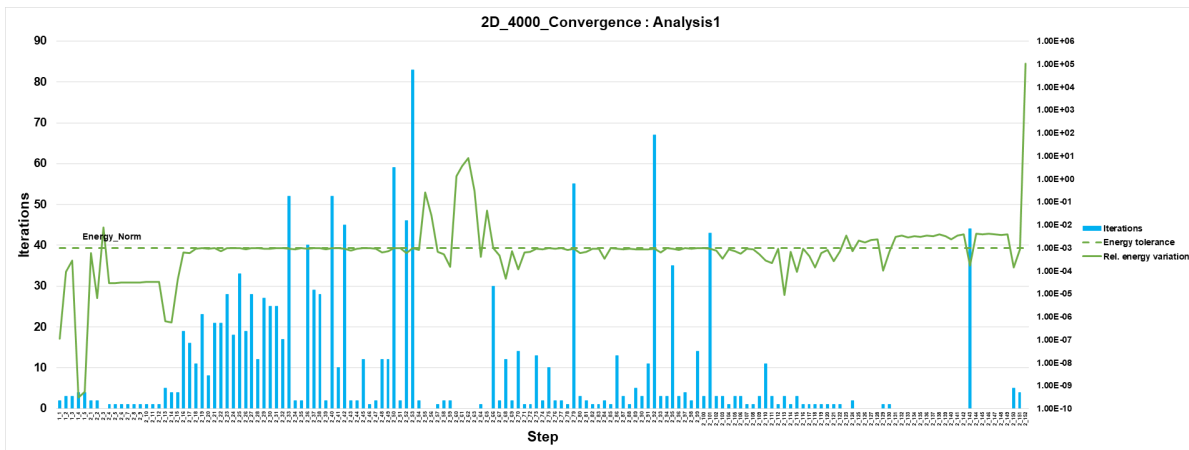


Figure A.4: Convergence behavior of 2D model with load at 4000mm from the support

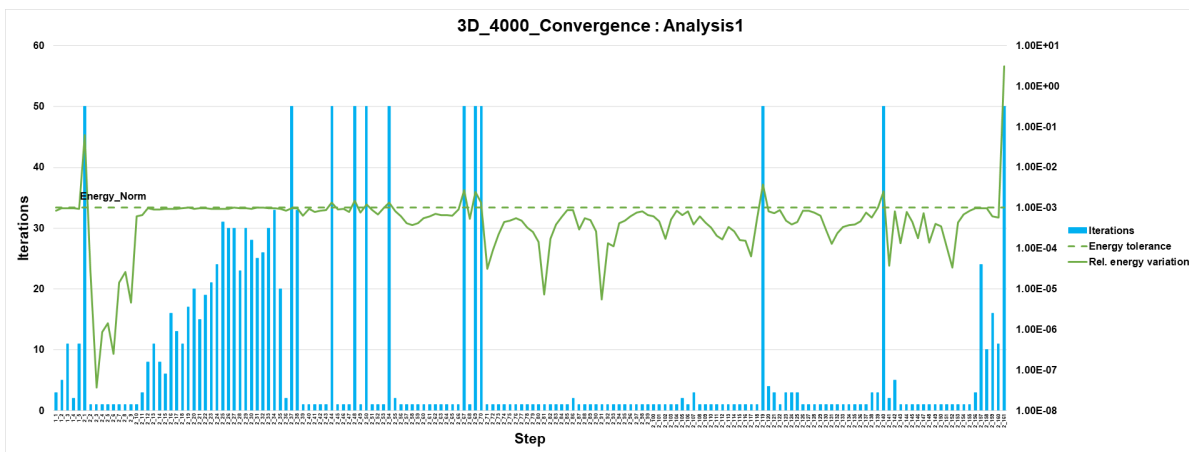


Figure A.5: Convergence behavior of 3D model with load at 4000mm from the support

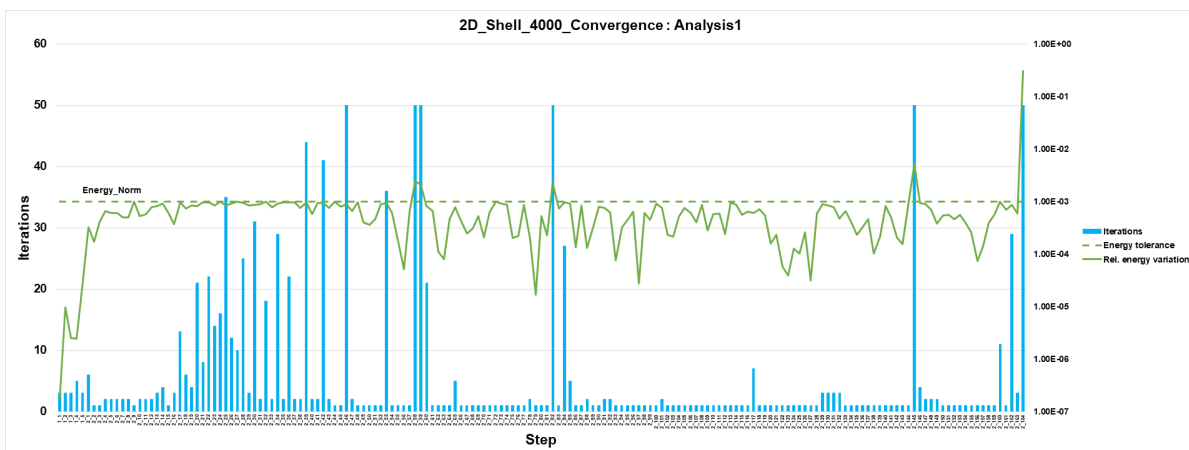


Figure A.6: Convergence behavior of 2D shell model with load at 4000mm from the support

B

Appendix B

This appendix shows the convergence behavior of the equivalent beam model and the disjointed bridge model used to compare the possibility of modeling the behavior of the beam as though it is connected to the bridge through cross-beams.

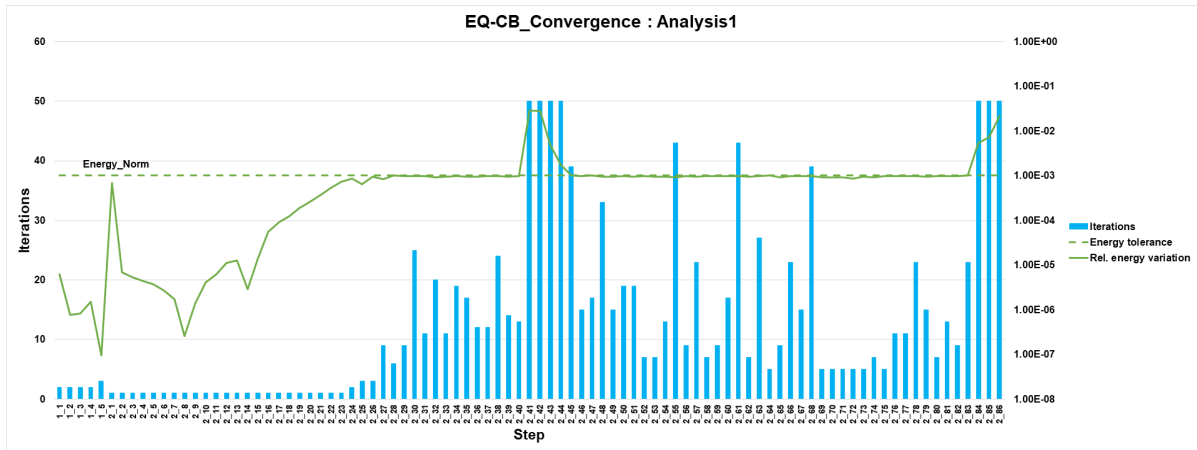


Figure B.1: Convergence behavior of EQ-CB Model

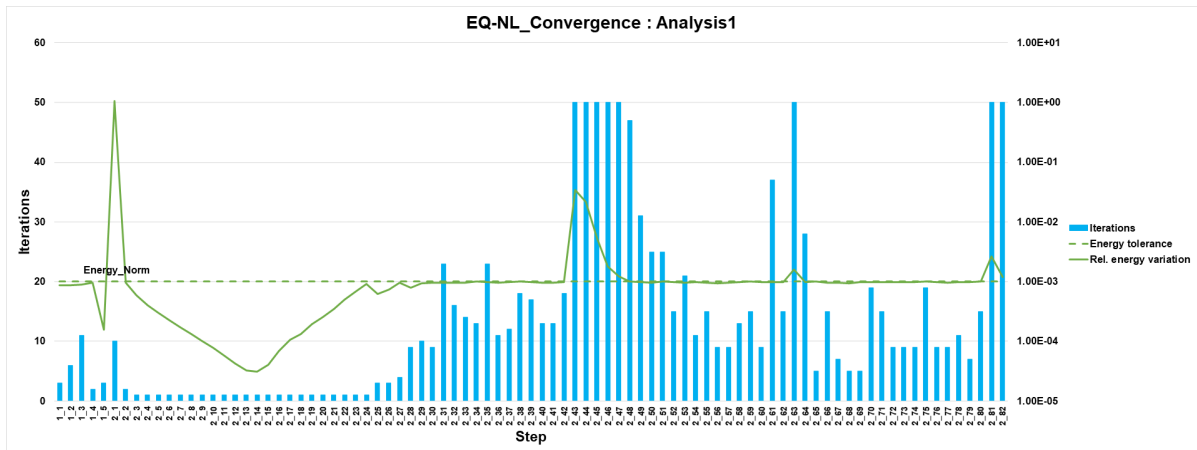


Figure B.2: Convergence behavior of EQ-NL Model

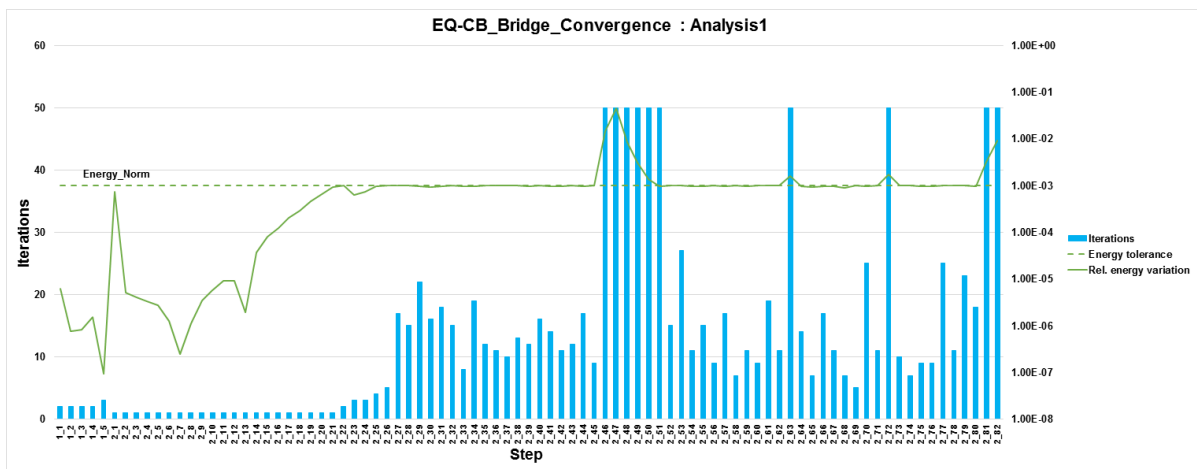


Figure B.3: Convergence behavior of EQ-CB model used for comparison with disjointed bridge model

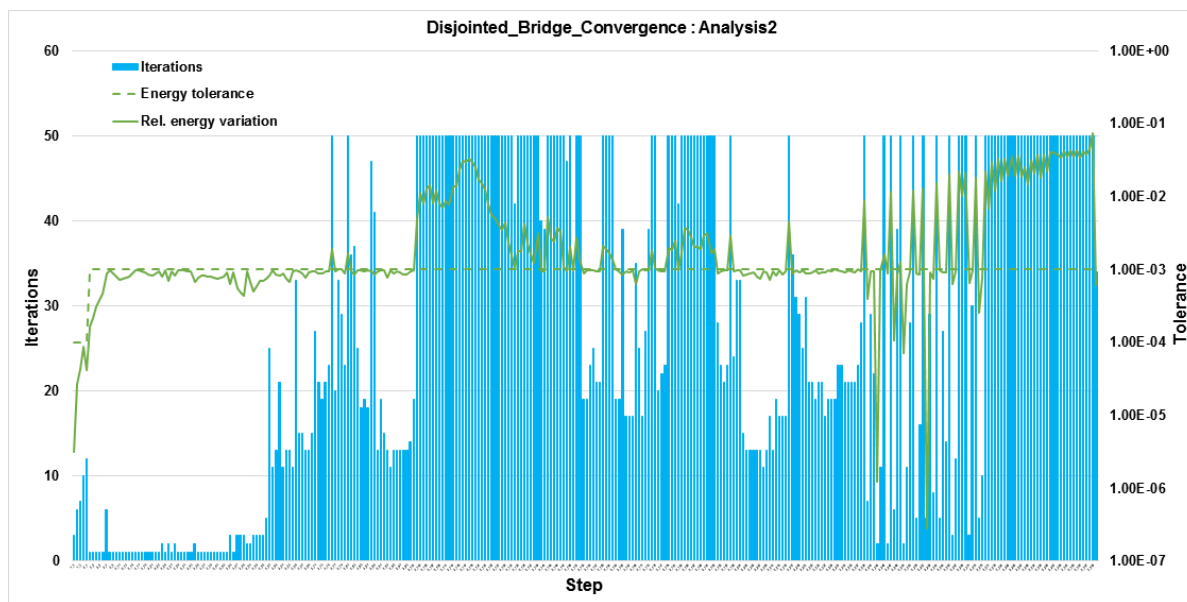


Figure B.4: Convergence behavior of the disjointed bridge model

C

Appendix C

This section of the report shows a possible conference publication following the research conducted during the course of the project.

An Approximate Analytical Approach to Study Arch Action in Concrete Beams

Shozab Mustafa¹, Sebastiaan Ensink¹, Max Hendriks¹, Cor van der Veen¹

¹Delft University of Technology
Faculty of Civil Engineering & Geosciences
Stevinweg 1, 2628 CN Delft, The Netherlands

Abstract. Arch action significantly improves the load bearing capacity of concrete members. This paper presents a practical approach to quantify the arch action in rectangular and T-beams loaded with uniform and concentrated loads. The investigated approach is able to conservatively predict the load bearing capacity for beams with slenderness less than 15 and end-restraint stiffness equal to the stiffness of restraint member. Within these boundary conditions, the slenderness ratio seems to have a significant impact on arching while stiffness of end restraint and prestressing have only minor effect. For T-beams, this methodology is only applicable if the failure is due to crushing of concrete.

1. Introduction

The arch action is significant in concrete members due to a large difference in compressive and tensile behavior of concrete. The cracking in the tensile zone causes change in the position of neutral axis which in turn causes the axial extension of the concrete member [Valipour et al. 2013]. If this extension is prevented by lateral restraints, like cross-beams in a bridge, an internal arch action is generated in the concrete member that results in significantly enhanced capacities.

The main focus of research on arch action is related to the response of bridge deck slabs [Taylor et al. 2002] and the progressive collapse of reinforced concrete frame structures [Valipour et al. 2013]. In both the cases the cross-section of the loaded member is assumed to be rectangular with a centrally placed concentrated load.

This study presents an approximate analytical approach to study the arch action in rectangular and T-shaped beams loaded with UDL and concentrated load at varying position along the length of the beam in efforts to quantify the arch action in beams as part of the bridge system.

2. Approximate Analytical Model

The approximate analytical model developed in this study is in line with the method suggested in CUR Recommendation 077 (Calculation rules for unreinforced underwater concrete floors [77:2014 2014]) for determination of arch action in underwater concrete floors.

2.1. Beams with Rectangular Cross-section

For the analytical model, the starting point is the load distribution in an un-deformed state, the factor F_0 (figure 1) is to account for initial axial forces in the system. The compressive zones at supports and at mid-span are assumed to be plastic hinges connected through infinitely rigid rods i.e. shortening of the strut under membrane force is ignored. To be conservative a triangular stress distribution is assumed and the line of action of force is assumed to be passing through the centroid as shown in figure 1.

As the load on the system increases, the mechanism wants to stretch and if this stretch is resisted, an increase in the membrane force (ΔF) is observed depending on the stiffness (k) of lateral restraint. An internal moment is developed in the beam following the membrane force (F_{tot}) and internal lever arm (z) which is in equilibrium with the externally applied moment. As

the load is increased, the height of compressive zones (x_{field} and x_{stpt}) and vertical deformation (α_v) increases causing a reduction in the internal lever arm which influences the ultimate load bearing capacity (q_u or F_u) of the concrete member. A pictorial representation of the arching mechanism is shown in figure 1.

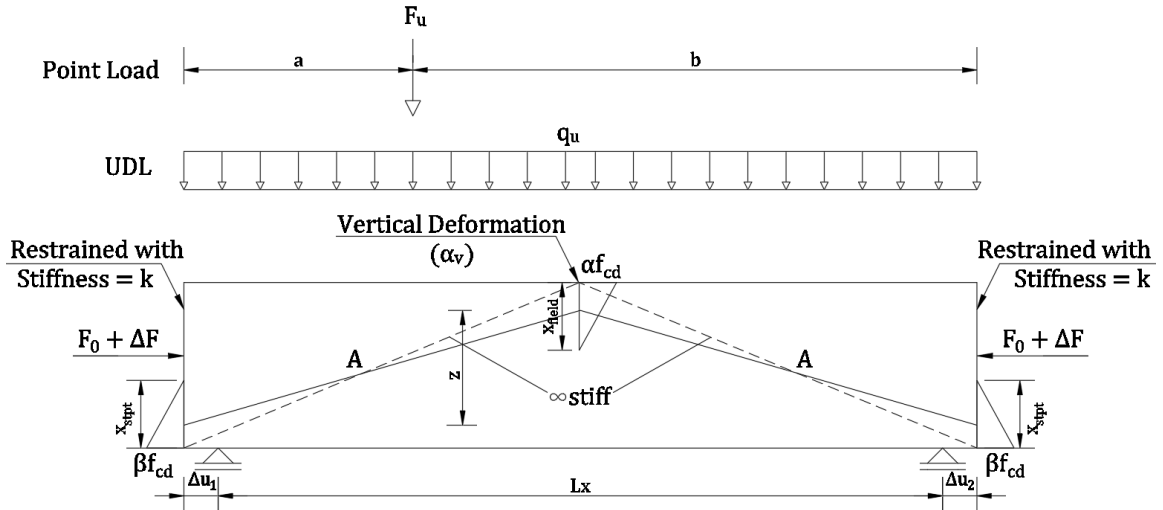


Figure 1. Arch action in concrete members

This methodology can be used for beams loaded with UDL or point loads as shown in table 1 where, b is the width and h is the height of the beam. Note that for beams with UDL the factor $\alpha = \beta = 1$ and for beams with point loads the factor $\beta = 0.50$ to take into account effects of localization at the point of application of the load. For asymmetrically applied point loads the horizontal stretch is different on both sides and this has been taken into account using infinitely rigid struts while for beams with uniform loads, $\Delta u_1 = \Delta u_2 = \Delta u$.

UDL	Point Load
$\Delta F = k(\Delta u)$	$\Delta F = k(\Delta u_1)$
$F_{tot} = F_0 + \Delta F$	$F_{tot} = F_0 + \Delta F$
$x_{field} = \frac{2 \cdot F_{tot}}{b \cdot \alpha f_{cd,pl}}$	$x_{field} = \frac{2 \cdot F_{tot}}{b \cdot \alpha f_{cd,pl}}$
$x_{stpt} = \frac{2 \cdot F_{tot}}{b \cdot \beta f_{cd,pl}} = \frac{x_{field}}{\beta}$	$x_{stpt} = \frac{2 \cdot F_{tot}}{b \cdot \beta f_{cd,pl}} = \frac{x_{field}}{\beta}$
$A^2 = (h)^2 + \left(\frac{L_x}{2}\right)^2 \rightarrow A$	$A^2 = (h)^2 + (a)^2 \rightarrow A$
$A^2 = (h - \alpha_v)^2 + \left(\frac{L_x}{2} + \Delta u\right)^2 \rightarrow \alpha_v$	$A^2 = (h - \alpha_v)^2 + (a + \Delta u_1)^2 \rightarrow \alpha_v$
$z = h - \frac{x_{field}}{3} - \frac{x_{stpt}}{3} - \alpha_v$	$z = h - \frac{x_{field}}{3} - \frac{x_{stpt}}{3} - \alpha_v$
$q_u = \frac{8 F_{tot} z}{(L_x + 2 \Delta u)^2}$	$F_u = \frac{F_{tot} z (L_x + \Delta u_1 + \Delta u_2)}{b a}$

Table 1. Step by step procedure for application of approximate analytical model

2.2. T-Beams

For extension of the analytical model to T-beams, a regular T-shape is considered with a constant width of flange and web as shown in figure 2. The difference in the width of web and flange results in different stress concentrations at support and mid-span and this has been taken into account using factor α and β . For T-beams with UDL, the factor β can be considered equal to one owing to the thin web while the factor α can be defined as shown in equation (1). The height of the compressive zone at mid-span and at supports has been calculated using the beam

geometry and the rest of the procedure is the same as outlined in table 1 for beams loaded with UDL.

$$\alpha = \frac{0.8b_w}{b_f} + 0.4 < 1.0 \quad (1)$$

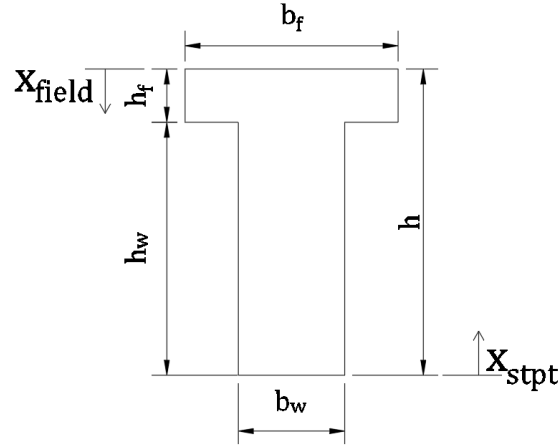


Figure 2. T-beam cross section

For T-beams with point loads the factors α and β are modified, where $\alpha = 1.0$ due to localization and β is defined in equation (2) following the results of non-linear finite element analysis (NLFEA). The compressive zones are calculated following the geometry of cross-section and the rest of the procedure is as defined in table 1 for beams with point loads.

$$\beta = 1.25 - 0.8 \frac{b_w}{b_f} < 1.0 \quad (2)$$

3. Numerical Models

All the numerical models used for the validation of the approximate analytical model are developed using DIANA 10.2 (release date 2018-11-13) following the guideline for non-linear analysis of concrete structures [Hendriks et al. 2012].

The models are developed in a 2D work environment and have a total length of 8700mm with 400mm long steel plates for the supports at 350mm from each edge. As assumed in the analytical model, all the beams are un-reinforced concrete beams - study has also been performed on prestressed beams and no significant differences have been observed. The beam is restrained using a linear elastic interface over the complete height at both edges of the beam. The concrete has been assigned a parabolic compression behavior [FEA and Manie 2017] and Hordijk tension-softening behavior [Hordijk 1991] following the guidelines [Hendriks et al. 2012]. The support plates are assigned linear elastic steel properties and an interface has been used between the plates and the beam to avoid concentration of stresses. A load-controlled analysis is performed using full Newton-Raphson method with the energy norm tolerance of 0.001. The peak values reported in all the studies correspond to the last converged load step before numerical failure which is defined by energy norm exceeding 10%.

4. Comparison of Analytical and Numerical Models

4.1. Slenderness Ratio

To verify the approximate analytical model, comparison has been made with the results of NLFEA as shown in figure 3. The peak load (q_u) before numerical failure, horizontal deforma-

tion (Δ_u), vertical deformation (α_v) and membrane force (F_{tot}) are all compared. As the beams are un-reinforced, the membrane force has been calculated assuming an internal lever arm of $0.75h$ (75% of the height of concrete member), following the results of NLFEA.

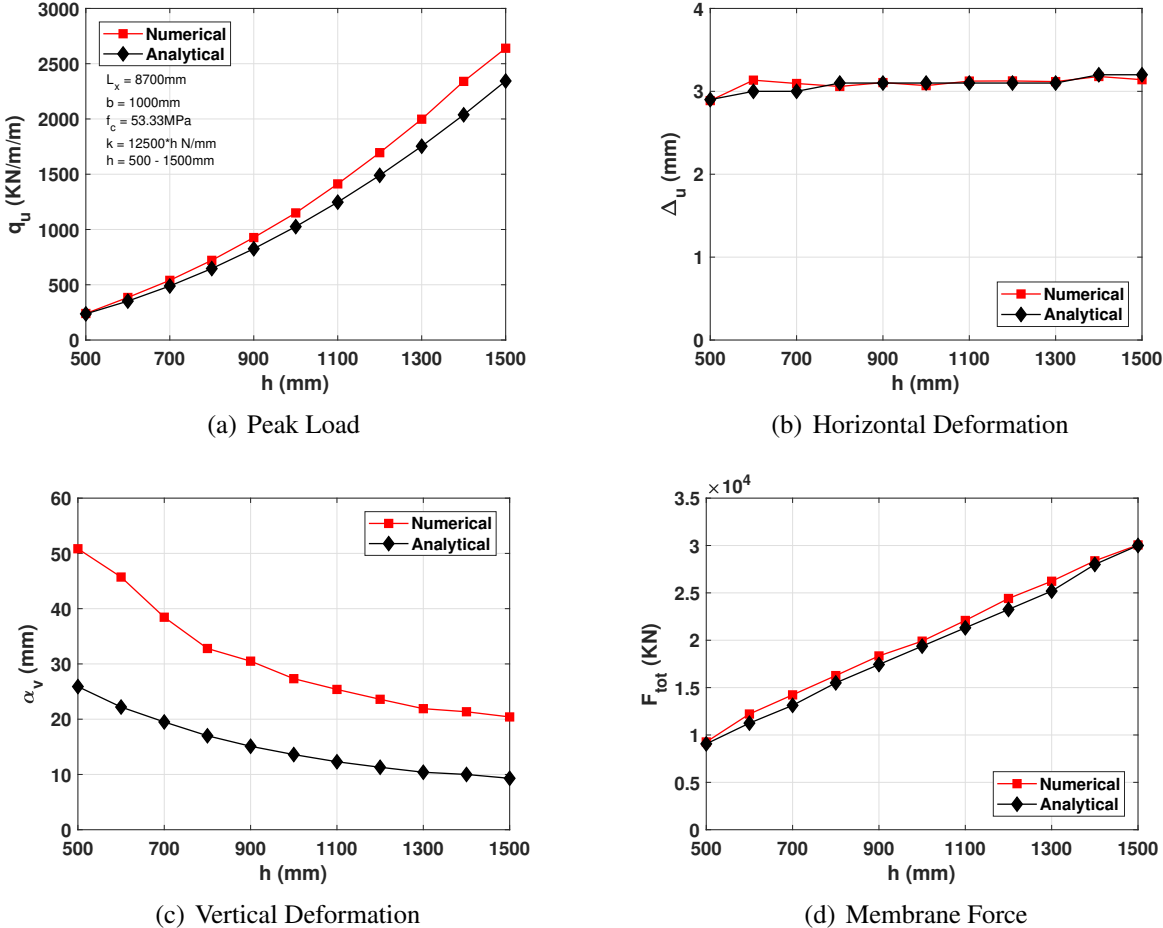


Figure 3. Effect of slenderness ratio on arching capacity

The peak load graph (figure 3a) shows that indeed the span-to-depth ratio has a significant effect on the arching capacity of concrete members as also concluded by several authors [Taylor et al. 2002, Park and Gamble 2000, Yu and Tan 2014, Kang and Tan 2017] - given that enough restraint is available. It can also be seen that the approximate analytical method is able to conservatively predict the capacity of all the beams with a maximum difference of 12%. As the slenderness increases, the difference in analytical and numerical capacities reduces, hence it is recommended to use this method only for beams with a slenderness of less than 15. The results in figure 3b show that the horizontal deformations predicted by the analytical and numerical approaches are also comparable with a maximum difference of 5% for all the studied slenderness ratios. However, the analytical model underestimates the vertical deformations (figure 3c) by almost 50%, possibly because the analytical model does not take into account the bending deformations of the beam and the shortening of the strut under the membrane force. The analytical model is also able to predict the membrane force in the system with an accuracy of 10% as shown in figure 3d. The phenomenon of arching is defined by the horizontal stretch and membrane force in the system and the approximate analytical model seems to be able to quantify the behavior in accordance with the numerical results for all the studied slenderness

ratios.

The vertical deformations and membrane forces show a similar co-relation with the numerical results for all the studied parameters, hence are not discussed further.

4.2. Stiffness of End-restraint

To study the effect of varying end restraint on the arch action in concrete beams the stiffness of restraint is varied from $25 \times 10^6 \text{ N/mm}$ to $1.25 \times 10^6 \text{ N/mm}$.

As seen from the results in figure 4a, the stiffness of horizontal restraint only has a significant effect on the arching capacity of the concrete members when it is rather low, as also concluded by other authors [Valipour et al. 2013], who made comparison between the stiffness of end restraint and the axial stiffness of the restrained member to develop a minimum criterion for the development of arch action - similar efforts are made to come up with a minimum support stiffness for applicability of the method discussed in this study. When comparing the analytical and numerical results it can be seen that the analytical model is able to conservatively predict the arching capacity of concrete member when the stiffness is greater than the axial stiffness of the member. This effect is rather pronounced in figure 4b, as the analytical model significantly overestimates the horizontal deformations at low stiffness values. This is one of the limitations of the analytical model because it allows stretching of the member until the membrane force responsible for the compressive failure of concrete is reached as there is no limitation on the stretching of the system. It is therefore concluded that for the application of this analytical model, the end stiffness should at least be equal to the stiffness of the restraint member. Given that this restraint is available the analytical model can predict the capacity within 12% and horizontal deformation within 10% of the numerical results.

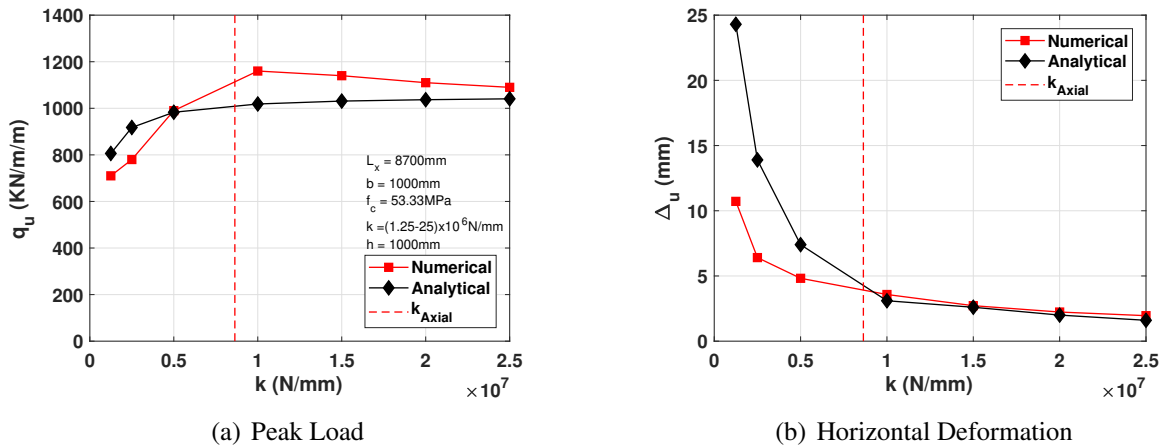


Figure 4. Effect of end stiffness on arching capacity

4.3. Pre-stressing

To compare the effect of prestressing on arch action, the prestressing load is applied as an external load on the concrete member in the numerical model. The initial prestress is increased from 0 MPa to 10 MPa and as seen from figure 5a, prestressing seems to have a minor influence on arch action - increasing the prestress to 10MPa increases the arching capacity by only 11%. It can also be seen that the approximate analytical model is not able to capture this effect as the increase in capacity is not observed and the error in predicting horizontal deformation increases with increasing prestress. This is possibly because the analytical model ignores the positive effects of prestressing and treats the prestressing force as an external load causing the compressive failure of concrete at lower levels of horizontal deformation.

It can be concluded that including the effect of prestressing as F_0 in the system might not be a suitable method for this approximate analytical approach.

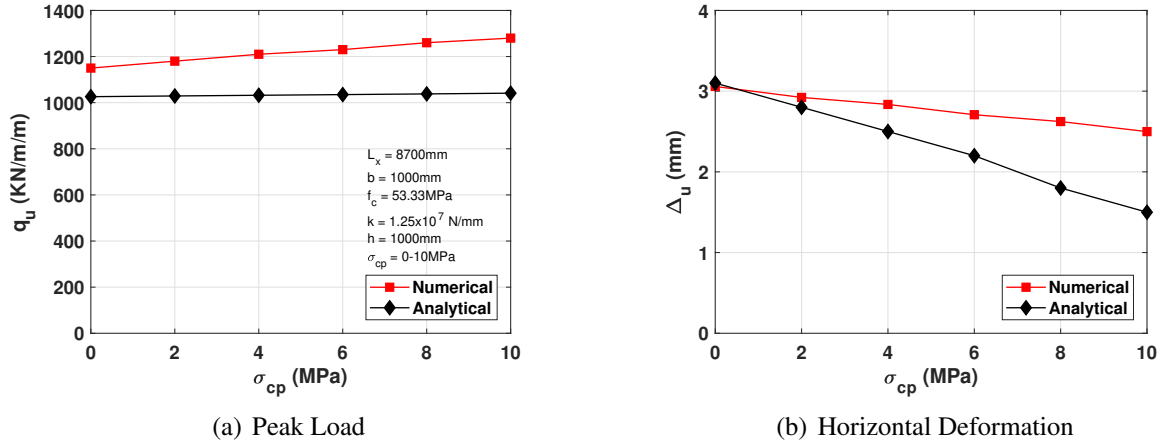


Figure 5. Effect of prestressing on arching capacity

4.4. Load Location

For the application of point load, a 500mm long steel plate is modeled in the numerical model with an interface between the plate and the beam. The load location is varied from mid-span (4000mm) to 1000mm from the support. As can be seen in figure 6a, the load location seem to have a minor effect on the arching capacity for the central L/2 of the span (2000mm from either of the supports). Beyond this, there is a direct transfer of load to the support and this effect is not captured by the analytical model.

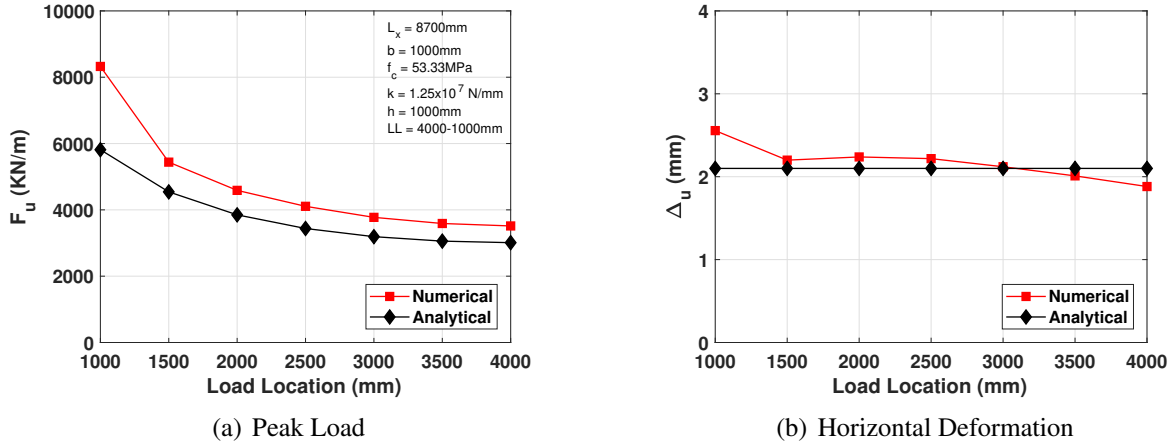


Figure 6. Load Location sensitivity analysis

For the load in central L/2 of the span, the analytical model is able to predict the capacity within 15% and horizontal stretch within 5% of the result from NLFEA.

4.5. T-beam

For T-beam, a sensitivity analysis is performed for the width of the web as it governs the failure mechanism. For thin webs ($b_w \leq 300mm$) the shear crack develops before the plasticity of concrete which is not in line with the assumptions of the analytical model and it is not able

to conservatively predict the arching capacity - this effect is evident in figure 7a and figure 8a. Nonetheless, it can be seen from figures 7 and 8 that the approximate analytical model is able to predict the arching capacity of beams with T-shaped cross-sections with an accuracy of at least 7.5% given that the numerical failure is due to the plasticity of concrete.

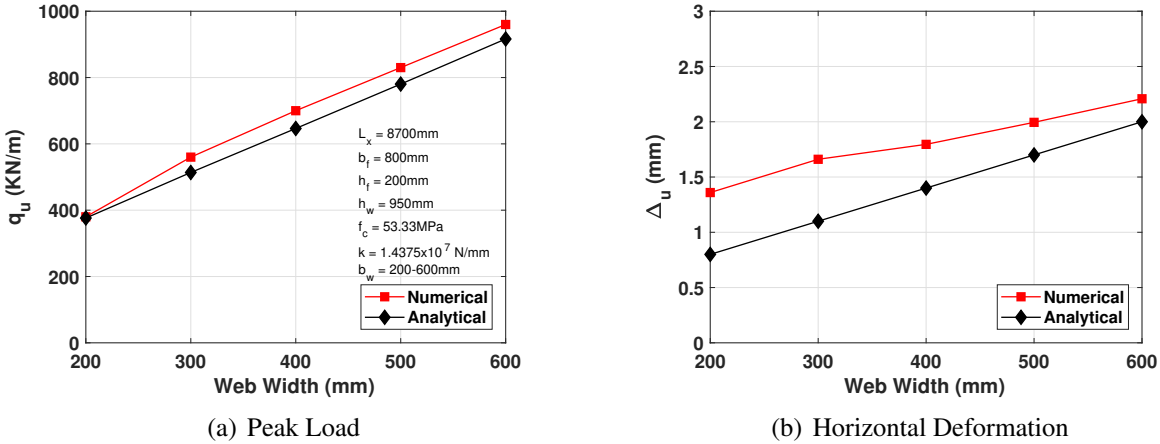


Figure 7. Effect of web-width on arching capacity (UDL)

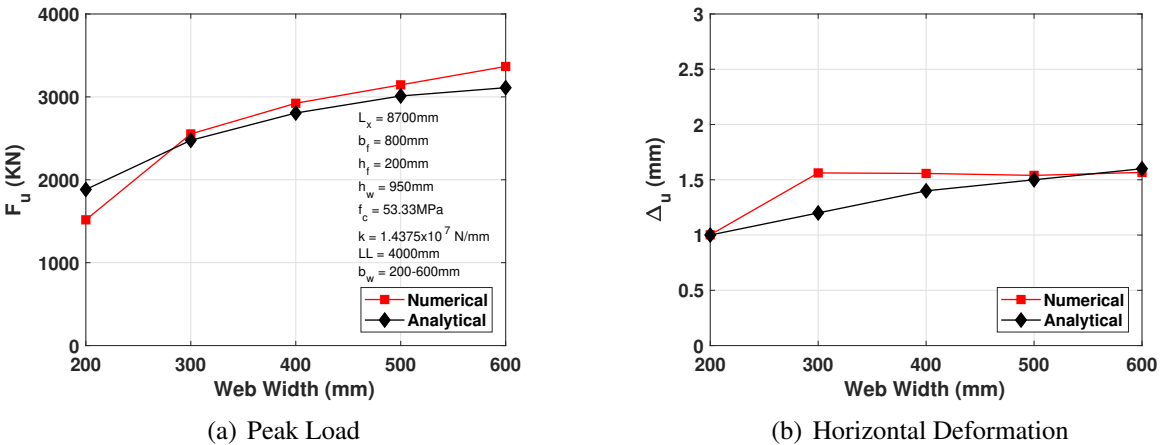


Figure 8. Effect of web-width on arching capacity (Point Load)

5. Conclusions

- The approximate analytical model investigated in this study is able to conservatively predict the arching capacity of rectangular beams with uniformly distributed loads if the slenderness of the member is less than 15 and the end restraint stiffness is at least equal to the stiffness of restrained member. Within these boundary conditions, the maximum difference in numerical and analytical results is 12%.
- Prestressing seems to have a minor effect on the arching capacity of concrete member and the analytical model is unable to capture this effect.
- The approximate analytical model significantly underestimates (50%) the vertical deformation of the member as it ignores the bending deformation and shortening of strut under membrane force.

- The extended model for beams loaded with point load is able to predict the arching capacity of beams for load at the central $L/2$ of the span with an accuracy of 15%.
- The extended model for T-beams loaded with UDL or point load is able to predict the arching capacity of beams with an accuracy of 7.5% if the numerical failure of the beam is due to plasticity of concrete. For beams with thin web, shear cracking is observed and the analytical model significantly overestimates the capacity because it does not take into account any other failure mechanism.

References

- [77:2014 2014] 77:2014, C. (2014). Cur-aanbeveling 77:2014 rekenregels voor ongewapende onderwaterbetonvloeren.
- [FEA and Manie 2017] FEA, D. and Manie, J. (2017). User's manual – release 10.2.
- [Hendriks et al. 2012] Hendriks, M. A., de Boer, A., and Belletti, B. (2012). Guidelines for non-linear finite element analysis of concrete structures. *Rijkswaterstaat Technisch Document (RTD)*, Rijkswaterstaat Centre for Infrastructure, RTD, 1016:2012.
- [Hordijk 1991] Hordijk, D. (1991). Local approach to fatigue of concrete, doctor dissertation. *Delft University of Technology*.
- [Kang and Tan 2017] Kang, S.-B. and Tan, K. H. (2017). Analytical study on reinforced concrete frames subject to compressive arch action. *Engineering Structures*, 141:373–385.
- [Park and Gamble 2000] Park, R. and Gamble, W. L. (2000). *Reinforced concrete slabs*. John Wiley & Sons.
- [Taylor et al. 2002] Taylor, S., Rankin, G., and Cleland, D. (2002). Guide to compressive membrane action. Technical report.
- [Valipour et al. 2013] Valipour, H., FarhangVesali, N., and Foster, S. (2013). A generic model for investigation of arching action in reinforced concrete members. *Construction and Building Materials*, 38:742–750.
- [Yu and Tan 2014] Yu, J. and Tan, K. H. (2014). Analytical model for the capacity of compressive arch action of reinforced concrete sub-assemblages.

Bibliography

- [1] EN 1992-1-1. Eurocode 2: design of concrete structures–part 1-1: general rules and rules for buildings, 2004.
- [2] CUR 77:2014. Cur-aanbeveling 77:2014 rekenregels voor ongewapende onderwater-betonvloeren, 2014.
- [3] Beatrice Belletti, Cecilia Damoni, Max AN Hendriks, and Ane de Boer. Validation of guidelines for nonlinear finite element analysis of concrete structures part: Prestressed beams. *Rijkswaterstaat Technisch Document (RTD), Rijkswaterstaat Centre for Infrastructure, RTD*, 1016-3B:2017, 2017.
- [4] HAW Cornelissen, DA Hordijk, and HW Reinhardt. Experimental determination of crack softening characteristics of normalweight and lightweight. *Heron*, 31:45, 1986.
- [5] D. den Boef. Materiaalkundig onderzoek betondruksterkte. Technical report, 2016.
- [6] Minister van Verkeer en Waterstaat. Inventarisatie kunstwerken. Technical report, 2007.
- [7] SWH Ensink, C van der Veen, DA Hordijk, EOL Lantsoght, Francisco de Quito, EC170157 Cumbaya, H van der Ham, and A de Boer. Full-size field test of prestressed concrete t-beam bridge.
- [8] Nima FarhangVesali, Hamid Valipour, Bijan Samali, and Stephen Foster. Development of arching action in longitudinally-restrained reinforced concrete beams. *Construction and Building Materials*, 47:7–19, 2013.
- [9] DIANA FEA and Jonna Manie. User’s manual – release 10.2, 2017.
- [10] Max AN Hendriks, Ane de Boer, and Beatrice Belletti. Guidelines for nonlinear finite element analysis of concrete structures. *Rijkswaterstaat Technisch Document (RTD), Rijkswaterstaat Centre for Infrastructure, RTD*, 1016:2012, 2012.
- [11] DA Hordijk. Local approach to fatigue of concrete, doctor dissertation. *Delft University of Technology*, 1991.
- [12] Shao-Bo Kang and Kang Hai Tan. Analytical study on reinforced concrete frames subject to compressive arch action. *Engineering Structures*, 141:373–385, 2017.
- [13] R.T. Koekkoek. Measurement report - loading of vechtbrug (25h-100). Technical report, 2017.
- [14] NEN. N 1009: 1950 nl reinforced concrete requirements gbv 1950, 1950.
- [15] Robert Park and William L Gamble. *Reinforced concrete slabs*. John Wiley & Sons, 2000.

-
- [16] Rijkswaterstaat. Guidelines for the assessment of works of art (rbk 1.1): assessment of the structural safety of an existing work of art during renovation, use and rejection rtd 1006: 2013, 2013.
- [17] SE Taylor, GI Rankin, and DJ Cleland. Guide to compressive membrane action. Technical report, 2002.
- [18] Hamid Valipour, Nima FarhangVesali, and Stephen Foster. A generic model for investigation of arching action in reinforced concrete members. *Construction and Building Materials*, 38:742–750, 2013.
- [19] Jun Yu and Kang Hai Tan. Analytical model for the capacity of compressive arch action of reinforced concrete sub-assemblages. 2014.